UNIVERSITÀ DEGLI STUDI DI PADOVA

UNIVERSITA' DEGLI STUDI DI PADOVA

Dipartimento di Ingegneria Industriale DII

Corso di Laurea Magistrale in Ingegneria dei Materiali

Device modelling of wide band gap perovskite solar cells for tandem applications

Relatore
Prof. Martina Roso

Correlatori
Prof. Johan Lauwaert
Nithin Thomas Jacob

Andrea Rapagnani
2015539

Anno Accademico 2022/2023

TABLE OF CONTENTS

GLOSSARY

Property

α	Absorption coefficient	m^{-1}
ε	Relative dielectric permittivity	-
λ	Wavelength	nm
μ_n/μ_p	Electron/Hole mobility	cm Vs^{-1}
σ_n/σ_p	Electron/Hole capture cross section	cm^2
τ_n/τ_p	Electron/Hole lifetime	s
ϕ	Photon flux density per wavelength	photons cm^{-2} s^{-1} nm
ϕ_m	Metal work function	eV
X	Electron affinity	eV
ω	Angular velocity	rad s^{-1}
Φ	Electrical potential	V
A	Cell area	cm^2
c	Velocity of light	m s^{-1}
d	Thickness	m
E	Energy	eV
$\overrightarrow{E_{bi}}$	Built-in-electric field	V m^{-1}
E_C	Energy conduction band level	eV
E_{Fn}/E_{Fp}	Electron/Hole Fermi level	eV
Eg	Energy band gap	eV
E_t	Energy trap level	eV
E_V	Energy valence band level	eV
G	Electron-hole generation rate	m^{-3}
h	Planck's constant	J s
$\hbar$	Reduced Planck's constant ($\hbar = h / 2\pi$)	J s
HOMO	Highest Occupied Molecular Orbital level	eV
I	Intensity of the light	W m^{-2}
J	Current density	mA cm^{-2}
k	Boltzmann's constant	J K^{-1}

n	Diode ideality factor	-
N_0	Photon flux at the surface	photons cm^{-2} s^{-1}
N_A/N_D	Acceptor/Donor density	cm^{-3}
N_C/N_V	Effective density of states in Conduction/Valence band	cm^{-3}
N_t	Defect density	cm^{-3} or cm^{-2}
P	Power density	W m^{-2}
q	Elementary charge	C
Rs	Series Resistance	Ωcm^2
Rsh	Shunt Resistance	Ωcm^2
T	Temperature	K
V	Voltage	V
v_{thn}/v_{thp}	Electron/Hole thermal velocity	cm s^{-1}
WF	Work Function	eV
x	Distance	m

Solar cell characteristic

EQE	External Quantum efficiency	%
FF	Fill Factor	%
J_0	Saturation current density	mA cm^{-2}
J_{mpp}	Current density at maximum power point	mA cm^{-2}
J_{SC}	Short circuit current density	mA cm^{-2}
PCE	Power Conversion Efficiency	%
P_{max}	Maximum power density	W cm^{-2}
V_{mpp}	Voltage at maximum power point	V
V_{OC}	Open circuit voltage	V

Materials

Ag	Silver
Al	Aluminium
Au	Gold
B	Boron
BCP	Bathocuproine
Br	Bromine
C	Carbon
C_{60}	Fullerene
Ca	Calcium
Cd	Cadmium
CIGS	Copper Indium Gallium Selenium
Cl	Chlorine
Cs	Cesium
FA	Formamidinium
Fe	Iron
H	Hydrogen
Hg	Mercury
I	Iodine
ITO	Indium Tin Oxide
MA	Methylammonium
N	Nitrogen
n-a-Si:H	*n*-type hydrogen-terminated amorphous Si
Nb	Niobium
n-c-Si	*n*-type crystalline Si
O	Oxygen
p-a-Si:H	*n*-type hydrogen-terminated amorphous Si
Pb	Lead
PEEDOT:PSS	poly(3,4-ethylenedioxythiophene) polystyrene sulfonate
PEIE	Polyethylenimine ethoxylated

PTAA	Poly[bis(4-phenyl)(2,4,6-trimethylphenyl)amine]
Sn	Tin
Te	Tellurium
Ti	Titanium
Zn	Zinc

General terms

n-	Majority of carriers are electrons
p-	Majority of carriers are hole
TCO	Transparent Conductive Oxide
2T	Two Terminal
PSCs	Perovskite solar cells
CAGR	Compound Annual Growth Rate
SEM	Scanning Electron Microscope
SAM	Self assembled monolayer
SCR	Spatial charge region
i-	Intrinsic
ETL	Electron Transport Layer
HTL	Hole Transport Layer
PVD	Physical Vapour Deposition
CVD	Chemical Vapour Deposition

INTRODUCTION

Perovskite solar cells are a promising technology for the energy sector. The current digital and consumeristic age has led to an energy crisis and global warming. The world green-house emissions account for the 74% to the energy production, so the global warming problem is principally an energy problem. Demand for power could be reduced in three ways: by reducing our population, by changing our lifestyle and by keeping our lifestyle, but reducing its energy intensity through "efficiency" and "technology" (MacKay 2009). At this third point, we must focus our attention on solar panels as renewable source of energy, indeed they use an infinite and free source, the Sun. Solar panels can be used as standalone systems, which do not require thermal mechanical linkages like in the conventional grid systems, and they are durable with lifespan more than 20 years. The solar panel efficiency is increasing, but for a single junction Si cell, most common photovoltaic system in the market, the efficiency limit is around 30% (Shockley-Queisser limit), so new technologies for energy harnessing are being developed. The perovskite material is opening new opportunities for energy harnessing in the photovoltaic sector. Studies of solar panels based on perovskite are proving the continuous growth in solar cell efficiency over the years passing from 14.1% in 2013 to 25.7% in 2022 (NREL 2022). The perovskite has wide scope for improvements and various fields of application like in rigid or flexible solar panels, electric automobiles and in space (Fu et al. 2018) (Ilic 2020). The integration of perovskite cell with the Si cell is becoming a concrete solution to increase the Si cell efficiency, this type of cell is called tandem cell. The tandem cells can surpass the Shockley-Queisser limit for a single-material cell reaching the theoretical limit of 44% in efficiency (Würfel and Würfel 2016). The actual record in efficiency of a tandem perovskite/Si cell is 31.25%, about 30% higher than other solar technologies (EPFL 2022).

This work is a study of wide band gap perovskite solar cells for tandem applications. The perovskite cell is modelled with Solar Cell Capacitance Simulator (SCAPS) program to be a feasible and efficient as possible. SCAPS is powerful simulation tool to design and study solar cell models varying materials parameters and configuration. This program is widely used by the researchers as it is well adapted to study the solar cell behavior in the

first stages of development. The models presented are a perovskite top cell with energy band gap *Eg* of 1.68 eV and a Si bottom cell with *Eg* of 1.12 eV. Every cell is (1) designed to be feasible, (2) investigated, and (3) its findings are reported. The models are first studied in standalone condition and their spectral response is displayed, then they are virtually stacked together to create a tandem cell. Every layer of the cells is studied giving an outlook of the most influential parameters for cell optimization.

Further optimization studies can be carried out for candidate materials for perovskite solar cell in tandem photovoltaics. It is critical to study the recombination mechanisms that occurs between the top and the bottom cell for optimization. This will assist in the manufacturing of high efficiency solar cell.

CHAPTER 1 - SOLAR CELL AND TANDEM CELLS

1.1 The semiconductors and the *p-n* junction

The solar cell is a device that converts the light into electrical energy through the photovoltaic effect. All materials do not have the property of harvesting the light. They must have a particular energy band configuration that allows the electrons to change their energy state through excitation.

The semiconductors have the valence band full of electrons and the conduction band empty of electrons divided by an energy gap *Eg* that is between 0.1 eV and 3.5 (Shur 2005). A photon must have energy $E = \hbar\omega$ ($\hbar$ is the Planck's constant divided 2π and ω is the angular velocity) larger than this energy gap of the material to excite electrons from the valence band to conduction band. The main difference between the conductors, insulators and semiconductors is in this energy gap (Fig. 1.1). The insulators have high *Eg* that does not allow to the electron to have a band-to-band transition. The conductors do not have *Eg* because the valence and conduction band overlap so the excited electron will lose its energy reaching the lower energy level in a short time. In semiconductors, the excited electron returns to the low energy valence band from the high conduction band in a single step. The energy loss during this return is termed as recombination. The electrons in the conduction band can be collected and transported to a contact through an electron transport layer (ETL). The holes in the valence band are transported to the opposite

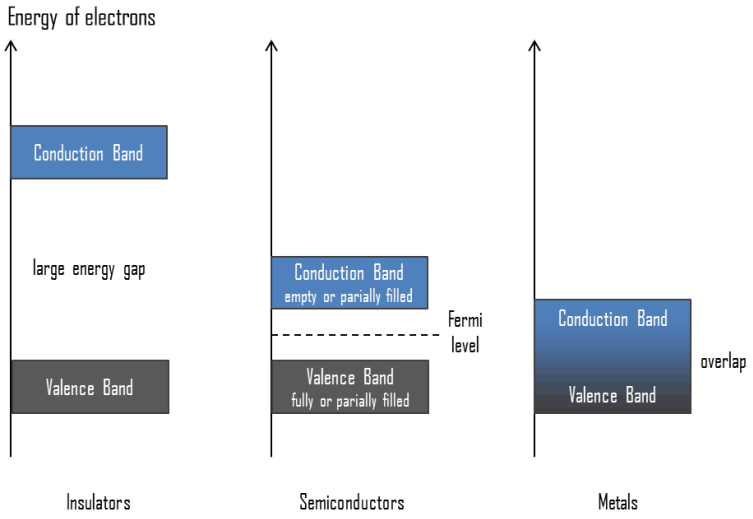

Figure 1.1. Energy band configuration for insulators, semiconductors and conductors or metal. (Nuclear Power 2019)

contact through a hole transport layer (HTL) (Würfel and Würfel 2016). The semiconductors are materials from either group IV of the periodic table, or from a combination of group III and group V or of combinations from group II and group VI. There are three types of semiconductors: intrinsic (*i*-type), extrinsic doped with donor impurities (*n*-type), and extrinsic doped with acceptor impurities (*p*-type). The intrinsic are the semiconductors in which the thermal excitation of a carrier from the valence band to the conduction band creates free carriers in both bands. The *n*- and *p*-type are doped semiconductors. Doping is a technique used to vary the number of electrons and holes in semiconductors. The increase in conductivity of *n*-type semiconductors is due to the addition of doped electrons. The Fermi level is shifted closer to the conduction band. The increase in conductivity of *p*-type semiconductors is due to the addition of doped holes. The Fermi level is shifted down closer to the valence band (Shockley 1950). These different types of semiconductors are essential to create a solar cell, indeed a *p-n* junction or a *p-i-n* junction (Fig. 1.2 a) are manufactured to collect the carriers.

When a contact or a junction is made, the Fermi levels must have the same energy, so bands bending occurs (Fig 1.2 b). The greater chemical potential of the electrons in the *n*-

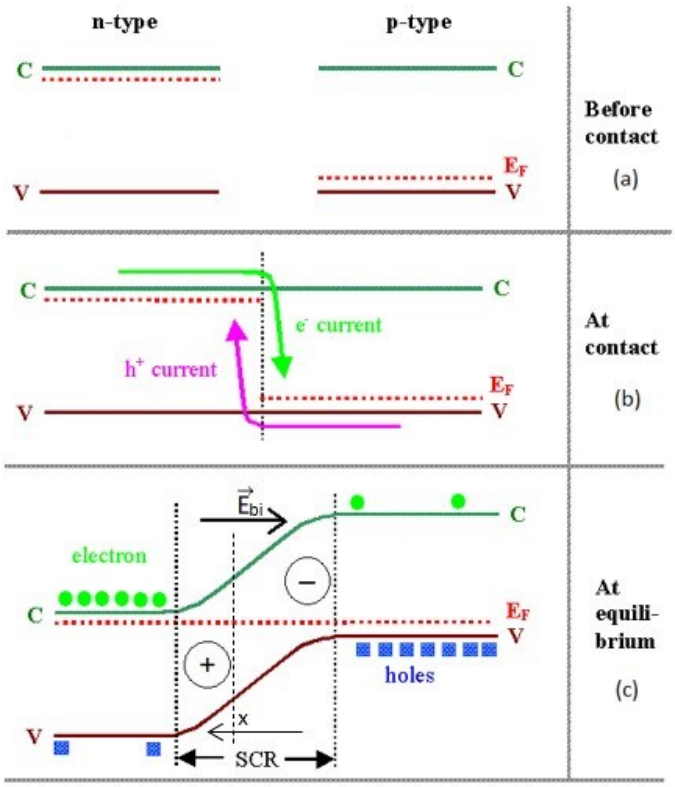

Figure 1.2. Working principle of a p-n junction: (a) before contact, (b) at contact, (c) at equilibrium. (Föll H. 2019)

conductor (and of the holes in the *p*-conductor) drives a diffusion current of electrons from the *n*-conductor to the *p*-conductor and a hole diffusion current from the *p*-conductor to the *n*-conductor. The result is a formation of a spatial charge at the interface of the junction: a positive charge in the *n*-region of the junction and a negative charge in the *p*-region. This region where there are not free charge carriers is the depletion region (SCR). A potential difference $\Phi_n - \Phi_p$ is set up. The equilibrium is established when the drift current generated from the potential difference contrasts completely the diffusion current. The potential difference $\Phi_n - \Phi_p$ is the result of the electrochemical equilibrium of the electrons in the *n*- and *p*-regions and is called built-in-voltage V_{bi} (Fig 1.2 c). To a V_{bi} correspond a built-in-electric field $\overrightarrow{E_{bi}}$ from the relation $\overrightarrow{E_{bi}} = \frac{dV}{dx}$ where x is the distance from the junction interface in the depletion region (Würfel and Würfel 2016).

In dark, a solar cell behaves as *p-n* junction in equilibrium where a potential difference is present but there is not current flow. The equilibrium is broken when it is exposed to light. The absorbance layer starts to generate electron-hole pairs, the electric field generated from the potential difference move the charges from the depletion region in opposite directions, the electrons will move to the *n*-region and the holes to the *p*-region (Würfel and Würfel 2016). The diffusion of charge carriers to the opposite region where the concentration is lower is limited due to the potential difference. The potential difference works as a barrier to avoid recombination of the electron-holes generated by

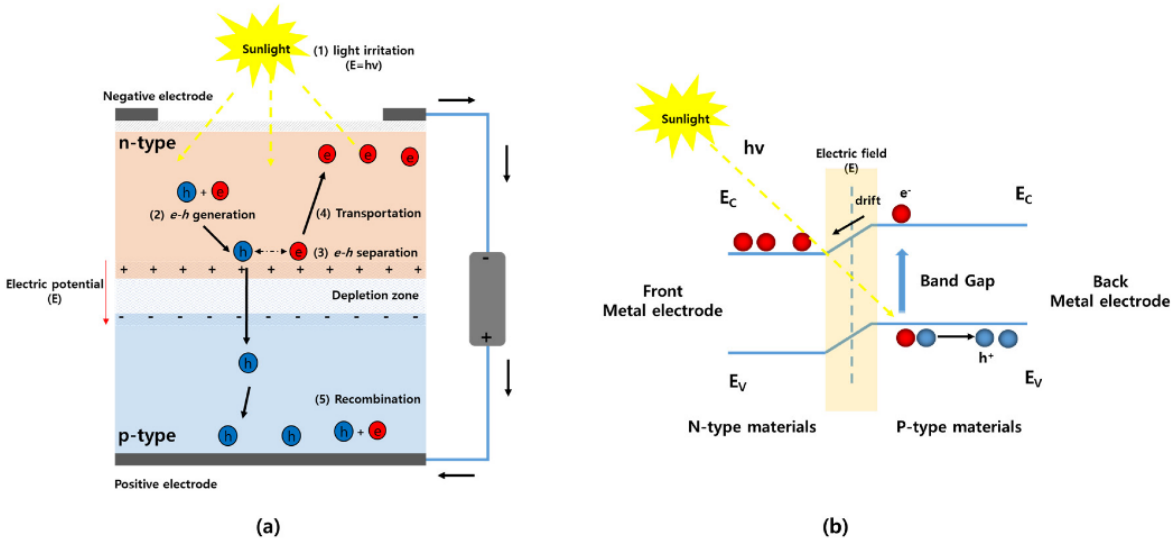

Figure 1.3. Solar cell and its working mechanism under illumination. (a) Representation of light irritation (1), electrons and holes generation (2), separation (3), transportation (4), recombination (5) in a solar cell. (b) Representation of electrons and holes generation and transportation in the energy band diagram of a solar cell. (S. Kim, Hoang, and Bark 2021)

the photons' absorption. As the concentration of electrons becomes higher in the *n*-type side of the junction and concentration of holes becomes higher in the *p*-type side of the junction, the *p*-*n* junction will behave like a small battery cell. If we collect the charges at the contacts placed one in front and one in the back of the cell we have an available potential difference. If the electrical circuit is closed a current flow (Fig. 1.3). The current can be increased applying a forward bias that decreases the resistance created by the potential difference in the SCR. The behaviour is the opposite if a reverse bias is applied, the current will not flow unless the voltage is too high that the junction exhibits a breakdown (Honsberg and Bowden 2019).

1.2 Solar cell characteristics

A solar cell is essentially described by five parameters (Khelifi 2009):

1. Short-circuit current density J_{SC} (mA cm^{-2})
2. Open-circuit voltage V_{OC} (V)
3. Fill factor FF (%)
4. Power conversion efficiency PCE (%)
5. External Quantum Efficiency EQE(λ) (%)

The short circuit current density J_{SC} is the current through the solar cell when the voltage across the solar cell is zero (i.e., when the solar cell is short circuited) (Fig. 1.4 a). J_{SC} is the largest current which may be drawn from the solar cell. J_{SC} is due to the generation and collection of light-generated carriers. For an ideal solar cell, J_{SC} and the light-generated current are identical, but in real solar cell thermalization and transmission losses occur.

The open-circuit voltage V_{OC} is the maximum voltage available from a solar cell sets up by the separation of charges, and this occurs at zero current (open-circuit condition) (Fig. 1.4 a).

The fill factor FF is a measure of the "squareness" of the J-V curve under illumination and is defined as the ratio

$$FF = \frac{J_{mpp}\, V_{mpp}}{J_{SC}\, V_{OC}}$$

(Eq. 1.1)

where J_{mpp} and V_{mpp} are respectively the values of current density and voltage at the maximum power condition.

The power conversion efficiency PCE is the power density delivered at the maximum power point as a fraction of the incident light power density P_{inc}. The PCE is roughly how much of the light power is converted in electricity power.

$$PCE = \frac{J_{mpp}\, V_{mpp}}{P_{inc}} = \frac{J_{SC}\, V_{OC}\, FF}{P_{inc}}$$

(Eq. 1.2)

The External Quantum Efficiency EQE is the ratio of the number of carriers collected by the solar cell to the number of photons of a given energy incident on the solar cell. The short circuit current density can be predicted from the wavelength dependency of external quantum efficiency EQE(λ) and the solar spectrum

$$J_{SC} = q \int_{\lambda} \phi(\lambda)\, EQE(\lambda)\, d\lambda$$

(Eq. 1.3)

where ϕ is the incident photon flux density per unity wavelength bandwidth and q is the elementary charge.

The J-V curve of a solar cell (Fig.1.4 a and b) is the superposition of the J-V curve in the dark with the light generated current. Illumination shifts the J-V curve down where power can be extracted from the cell. The J-V characteristic is then described by

$$J = J_0 \left[exp\left(\frac{qV}{nkT}\right) - 1 \right] - J_{SC}$$

(Eq.1.4)

where J_0 is the saturation current density, q the elementary charge, k is the Boltzmann's constant, T the absolute temperature, n is the diode ideality factor which in a typical device ranges from 1 to 2. The ideality factor takes in account the recombination mechanism taking place. Deviations from n = 1 indicates that either there are unusual recombination mechanisms or that the recombination is changing in magnitude (Caprioglio et al. 2020).

The V_{OC} can be described by

$$V_{OC} = \frac{nkT}{q}\, ln\left(\frac{J_{SC}}{J_0} + 1\right)$$

(Eq.1.5)

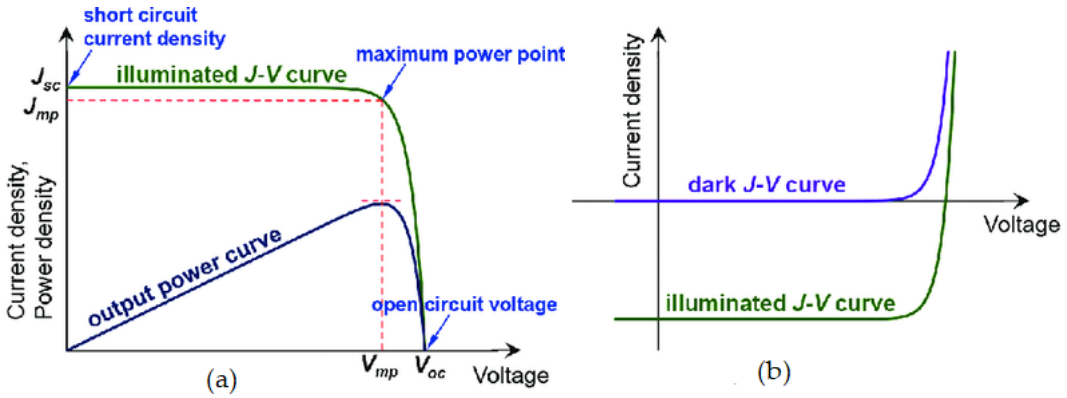

Figure 1.4. (a) J-V characteristic and parameters of a solar cell, (b) dark and illuminated J-V characteristic. V_{mp} and J_{mp} are V_{mpp} and J_{mpp}. (Tao 2016)

In real cells the J-V curve deviate from the ideal J-V curve Eq. (1.4) by parasitic affects, which can be described by two resistances, one in series (R_s) and one in parallel (R_{sh}) with the cell. Series resistance is due to the resistance of the cell material to current flow through the *p-n* materials and between the surfaces and the contacts. The parallel or shunt resistance is due to manufacturing defects that cause power losses by providing alternative current path through the cell (Würfel and Würfel 2016). Thus, when the parasitic resistances are included the diode equation becomes (Khelifi 2009)

$$J = J_0 \left[exp \left(\frac{q(V - JR_sA)}{nkT} \right) \right] + \frac{(V - JR_sA)}{R_{sh}A} - J_{SC}$$

(Eq.1.6)

where A is the cell area.

1.3 Tandem cell

The absorber material used for a solar cell has a specific energy gap that determine the absorption wavelength of the light. To harvest all the energy coming from the light, tandem solar cells are used. These solar cells use different absorber materials stacked together according to their energy band gaps. The tandems are being developed matching two, three or four different materials. From the absorption coefficient of the different semiconductor materials in Figure 1.5 it is clear there is good match between Si and perovskite. The perovskite has higher absorption coefficient α from 380 to 780 nm and the Si absorbs the light of higher wavelength until 1200 nm. The higher is absorption coefficient α the lower can be the thickness x of the cell as the it is explained by the following formula

$$I_{absorbed} = I_0 \, (1 - e^{-\alpha x})$$

where I is the intensity of the light in W m^{-2} and I_0 is the intensity of the incident light (Honsberg and Bowden 2019). Therefore, the main advantage of the perovskite against the Si is the possibility to be thinner. Pervoskite cells of the order hundreds nm than Si cells which are of the order hundreds μm in thickness. In the wavelength range of 380-780 nm the perovskite cell with lower thickness x and under the same illumination has higher

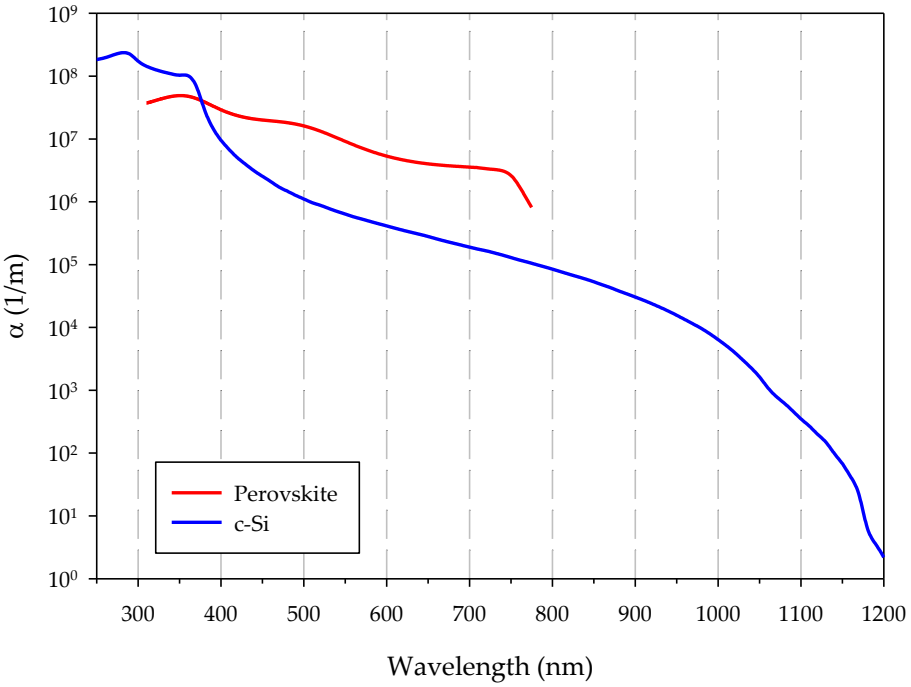

Figure 1.5. Absorption coefficient α (1/m) – Wavelength (nm) plot of perovskite and c-Si. Data are taken from Löper et al. (2015) for the perovskite and Green (1995) for the crystalline Si (c-Si).

electron-holes pairs generation rate G (m^{-3}) described by the formula

$$G = \alpha N_0 e^{-\alpha x}$$

where N_0 is photon flux at the surface (photons/unit-area/sec) (Honsberg and Bowden 2019).

The probability for the absorption of a photon with energy $\hbar\omega$ is defined by the absorption coefficient $\alpha(\hbar\omega)$, which is a material property, independent of the geometry of a body (Würfel and Würfel 2016). The absorption coefficient for a given photon energy, $\hbar\omega$, is proportional to the probability P_{12} of the transition of an electron from the initial state E_1 to the final state E_2, the density of electrons in the initial state $g_V(E_1)$ and the density of available final states $g_C(E_2)$, and is then summed over all possible transitions between states where $E_2 - E_1 = \hbar\omega$

$$\alpha(\hbar\omega) \propto \sum P_{12} \cdot g_V(E_1) \cdot g_C(E_2)$$

assuming that all the valence-band states are full and all the conduction-band states are empty. The absorption coefficient for direct transitions (perovskite and Si cases) is

$$\alpha(\hbar\omega) \approx A^*(\hbar\omega - \mathrm{Eg})^{1/2}$$

where A^* is a material constant (Luque and Hegedus 2011). Lower is the energy gap Eg more of the light spectrum can be utilized.

The tandem cells are used to reduce the thermalization losses, transmission losses (Fig. 1.6) and to improve the absorption efficiency of monolithic solar cell due to a better spectral utilization. A solar cell with Eg = 1.1 eV has a maximum solar conversion efficiency around 30% first calculated by William Shockley and Hans-Joachim Queisser at Shockley Semiconductor in 1961; would have an efficiency of 42% if all of the energy of

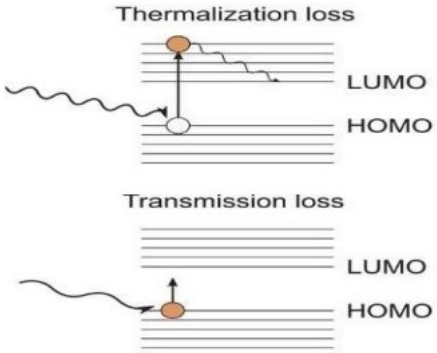

Figure 1.6. Thermalization and transmission losses in a semiconductor under illumination. (Chauhan and Singh 2021)

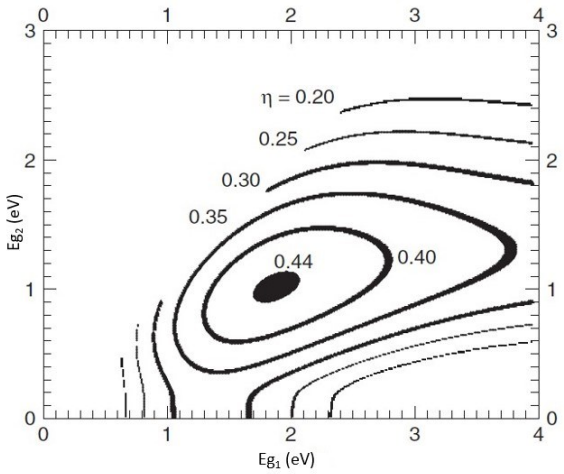

Figure 1.7. Efficiency for two solar cells in tandem operation, with energy gaps Eg_1 and Eg_2 for the AM0 spectrum when their energy currents are added. (Würfel and Würfel 2016)

the electron-hole pairs could be converted into electrical energy, i.e. if the thermodynamic efficiency were equal to 1. A tandem cell could achieve higher efficiency and the limit is 44% for the optimal combination of two materials with Eg_1 = 1.9 eV and Eg_2 = 1.0 eV (Fig. 1.7) (Würfel and Würfel 2016) which surpass the Shockley-Queisser limit. By stacking the sub-cells in order of decreasing bandgap. The light first falls on the cell with the greater energy gap which absorbs all photons with energy higher than Eg_1 and transmits all photons with smaller energy. The cell behind with the lower energy gap then absorbs the photons with energy between Eg_1 and Eg_2 (Fig. 1.8). This mechanism can be done with two or more cells improving the PCE every time a cell is stacked with the other. The limit for a tandem perovskite/Si is over 40% (Neder, Tabernig, and Polman 2022). The cells must be stacked in a consecutive configuration, i.e., if the first cell is *p-n*, the second must be *p-n* as well to have a tandem configuration *p-n-p-n*. If a third layer or a fourth layer will

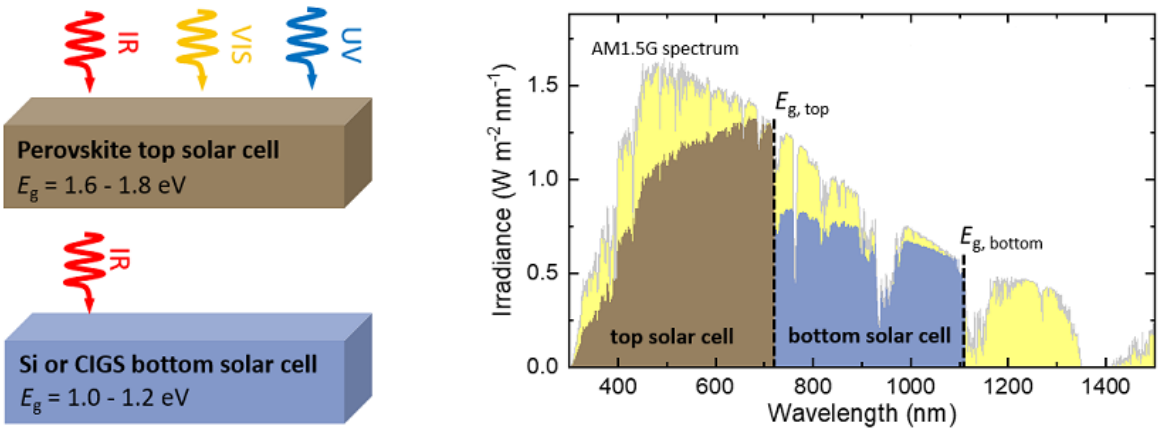

Figure 1.8. How the AM1.5G spectrum is harvested by a tandem perovskite/Si cell. (Paetzold 2021)

be stacked the "*p-n* order" must be respected. The interface layer between the cells must avoid recombination of the electron from *n* side of the top cell and the holes from the *p* side of the bottom cell. Electrical contacts between the cells, which absorb photons, must be avoided. This allows only for connection of the cells electrically in series (Würfel and Würfel 2016). In a tandem cell the working current is determined by the smallest short-circuit current. The working voltage is the sum of the voltages of the individual cells. An example of the J-V characteristic and EQE-wavelength plot for a tandem cell is showed in Figure 1.9. To prevent losses due to a series connection, the energy gaps or/and the thickness must be chosen so that the currents J_{mpp} at the maximum power points are the same for all cells. However, as the radiation from the sun is not constant during the day, the equality of the currents J_{mpp} of different cells cannot always be maintained.

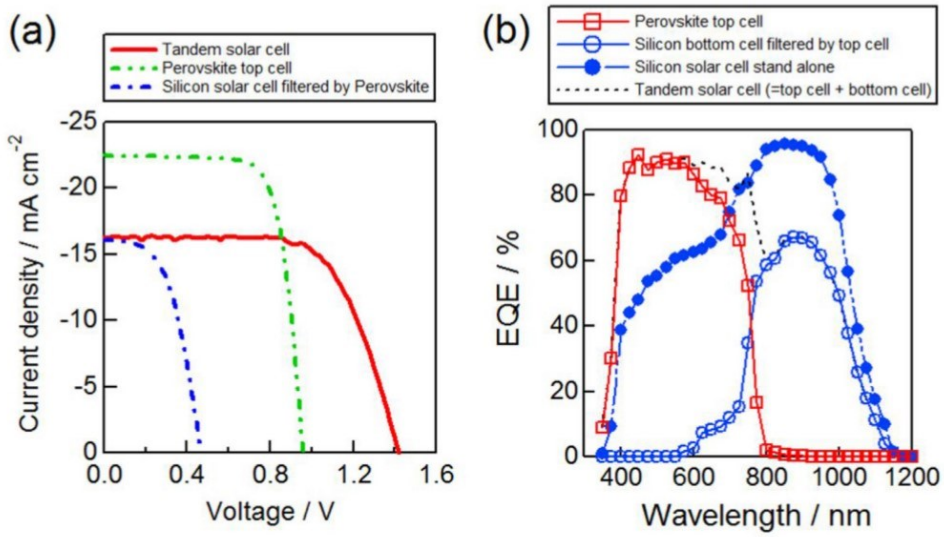

Figure 1.9. Example of (a) Current density J- Voltage V characteristic and (b) External Quantum Efficiency EQE-wavelength plot for a tandem cell. (Kanda et al. 2018)

1.4 Perovskite structure and properties

Perovskite is the class of compounds which have the same type of crystal structure as calcium titanium oxide ($CaTiO_3$) known as the perovskite structure (Wenk and Bulakh 2004). Perovskite structure is adopted by many oxides that have the chemical formula ABX_3, where X is an anion and A and B are cations of different sizes (A being larger than B) (Fig. 1.10). The idealized form is a cubic structure which is rarely encountered. The orthorhombic and tetragonal phases are the most common non-cubic variants. The larger cation A is organic and it is generally methylammonium, although related ethylammonium and formamidinium also give good results. The anion X is a halogen generally iodine, although Br and Cl are also commonly used in a mixed halide material. For efficient cells, cation B has universally been Pb. Sn forms similar compounds with theoretically more ideal bandgaps but generally lower stability. The archetypal compound is thus methylammonium lead triiodide $CH_3NH_3PbI_3$. $CH_3NH_3PbI_{3-x}Cl_x$ and $CH_3NH_3PbI_{3-x}Br_x$ mixed halides are also important (Green, Ho-Baillie, and Snaith 2014). The Perovskite solar cells (PSCs) consist of active perovskite layer that is sandwiched between electron transport layer (ETL) and hole transport layer (HTL). The *n-i-p* structure is when the transparent conducting layer is in front of ETL and the incident light goes through the ETL. The *p-i-n* structure is the opposite one (Fig. 1.11). There are two basics structures for the perovskite solar cells (PSCs) and are: mesoscopic and planar. Typically, mesoscopic structure has *n–i–p* configuration: compact ETL/mesoporous

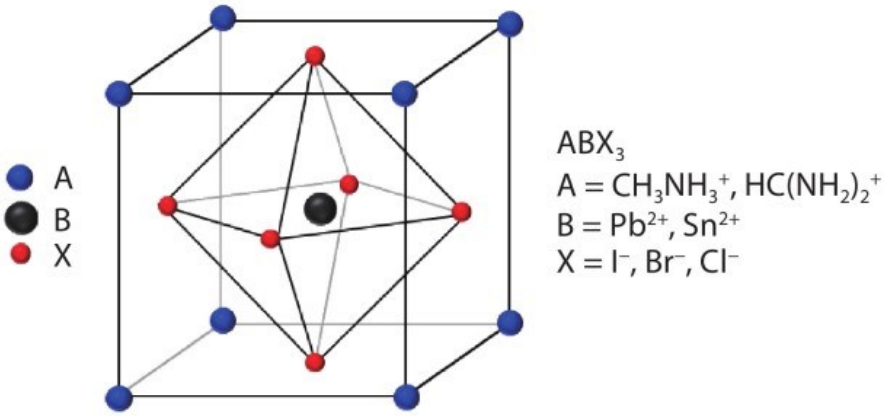

Figure 1.10. Perovskite chemical structure. (Davis and Yu 2020)

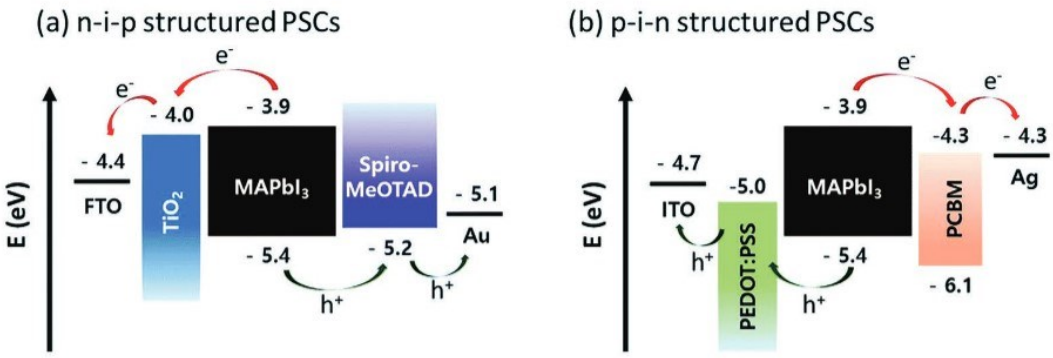

Figure 1.11. Energy band diagram of typical (a) n–i–p and (b) p–i–n structured PSCs. (Wang et al. 2019)

ETL/perovskite/HTL/electrode (Fig. 1.12 a). A perovskite absorber layer covers the scaffold forming a compact capping layer and penetrating the scaffold leading to an intermixed layer. The mesoporous layer can facilitate charge separation (Z. Li et al. 2018). The planar type PSCs are further divided into two band configurations: *n–i–p* planar and *p–i–n* planar (Fig. 1.12 b and c). The planar *n–i–p* architecture contains a compact ETL layer and thus does not feature the perovskite–ETL intermixed layer that is present in the mesoporous architecture. The mesoporous layer adds one more step to the fabrication process which is perhaps unfavourable for scaling. It remains to be seen if the mesoporous scaffold is indispensable for achieving higher PCE or improved stability (Z. Li et al. 2018). The planar *p–i–n* architecture is generally referred to as an inverted structure because the carrier extraction layers are inverted with respect to the *n–i–p* structure.

PSCs based on both mesoporous and planar structure exhibit high performance and stability. However, the comparison of the advantages of two different structures in stability is still under debate (Wang et al. 2019).

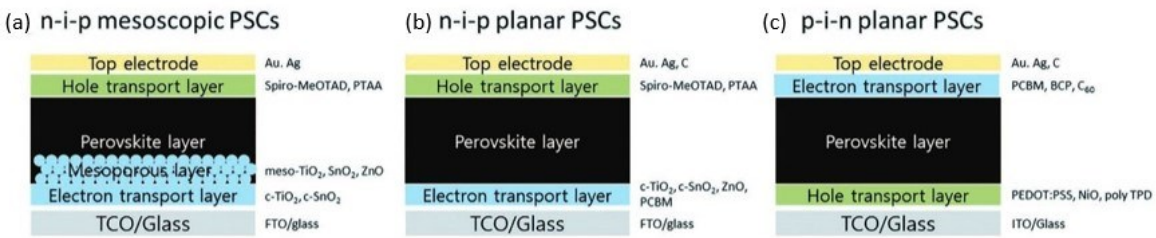

Figure 1.12. Device structures of (a) n–i–p mesoscopic, (b) n–i–p planar, and (c) p–i–n planar PSCs. (Wang et al. 2019)

1.5 Production of perovskite and tandem cells

1.5.1 Scalable production of perovskite solar cell

The production of perovskite is growing year by year due to the growth of the research in this field. The best scalable solution deposition methods for perovskite growth include blade coating, slot-die coating, spray coating, inkjet printing, screen printing, electrodeposition, and vapor-phase deposition.

In the blade-coating deposition method, a blade is used to spread precursor solution on substrates to form wet thin films (Fig. 1.13 a). This technique can be adapted for continuous fabrication with roll-to-roll setups in which the blade is stationary and flexible substrates on a roller are in motion. PSCs fabricated by blade coating have demonstrated PCE >19%.

Slot-die coating (Fig. 1.13 b) is like blade coating and uses an ink reservoir with a thin slit to apply ink over the substrate. Ink flow can be better controlled in slot-die coating, but this method normally requires larger quantities of ink thus is generally less suitable for use in the development of new ink chemistries. As a result, slot-die coating has been less explored. The resultant PSCs have a much lower PCE than those fabricated through blade coating. However, slot-die coating shows better yield and reproducibility than blade coating when the ink is already fully developed. Thus, it has more potential to be applied in roll-to-roll fabrication in the future.

In spray coating, a nozzle is used to disperse tiny liquid droplets onto substrates (Fig. 1.13 c). Spray coating can be further classified according to the method used for generating droplets, such as pneumatic spraying, ultrasonic spraying or electro spraying. Pneumatic spraying and ultrasonic spraying are commonly used for compact oxide layer deposition in PSCs. Droplet size and placement are random in the spraying process and several droplets need to overlap in a local area to ensure full coverage.

In inkjet printing, nozzles are used to disperse the precursor ink with fine control of the droplet size and trajectory (Fig. 1.13 d). Miniaturized nozzles and a short distance between the nozzles and substrate enable ultrafine lateral resolution. However, whether

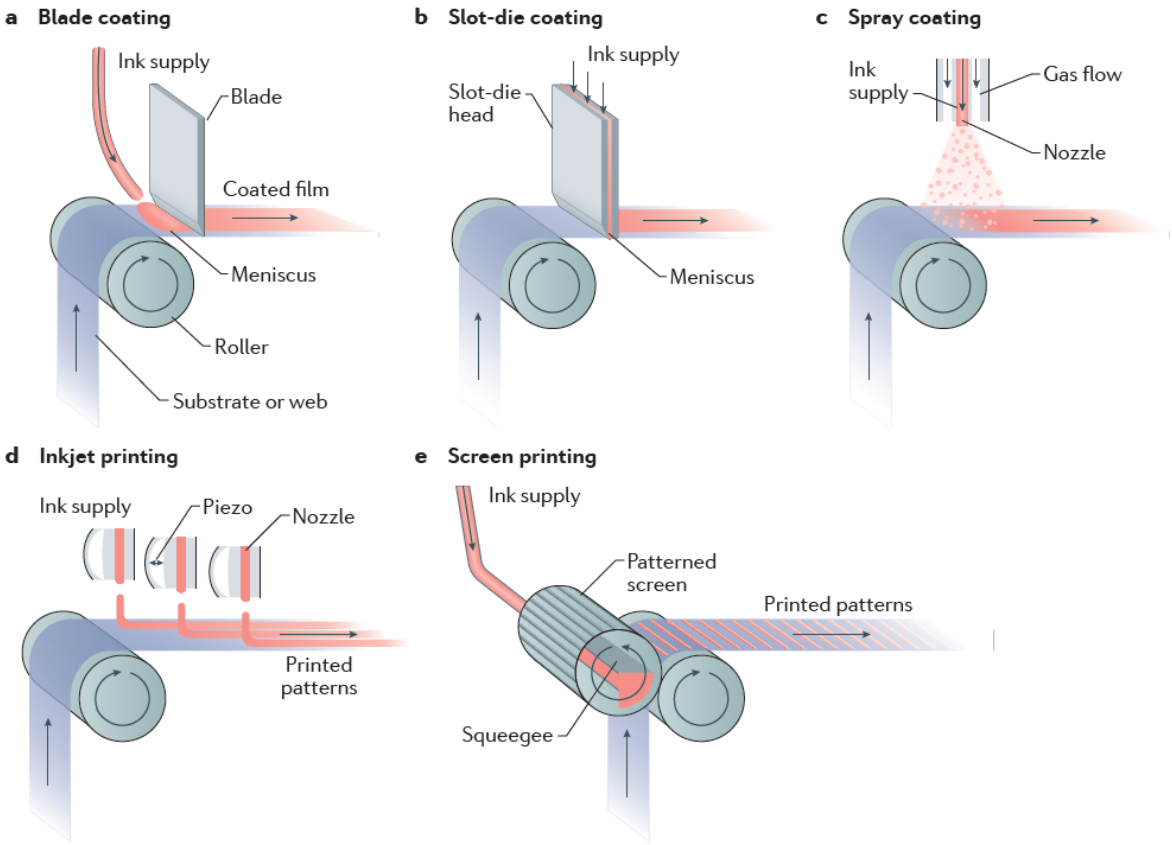

Figure 1.13. Common scalable solution deposition methods for the roll-to-roll fabrication of perovskite solar cells. (Z. Li et al. 2018)

inkjet printing is suitable for the high-volume, large-area production of perovskite solar modules will depend on the printing speed and device structure.

In screen printing, a patterned mesh screen is used to hold and transfer ink to the substrate (Fig. 1.13 e). A photosensitive polymer emulsion is used to block the ink in the unwanted area. The thickness of the resulting film is determined by the mesh size and thickness of the emulsion layer. Screen printing is usually used to fabricate mesoporous scaffolds and carbon back electrodes in PSCs.

Electrodeposition is another scalable solution deposition method to deposit thin films over a large area. It generally takes two steps. First PbO_2 or PbO is electrodeposited on a conducting substrate. The lead oxide is then converted into a perovskite through reaction with organic halides or reaction with HI acid to form PbI_2 which is then converted into a perovskite. The advantage of electrodeposition is the use of a non-toxic solvent (usually an aqueous solution) in the process.

Vapour-phase deposition is common in solar cell fabrication: the deposition of CIGS and CdTe relies heavily on physical vapour deposition (PVD). The doping of silicon is

realized through chemical vapour deposition (CVD). A PVD apparatus for the large-scale fabrication of solar cells has been developed and successfully applied. This experience and equipment have been readily translated to PSC fabrication. Perovskite thin films have been deposited with both PVD and CVD methods. PVD refers to the process in which a perovskite or its precursor is directly sublimated to form a perovskite thin film. CVD refers to the process in which a lead halide is converted into a perovskite using organic halide vapours. Although vapour-phase deposition has the potential to be used to deposit perovskite thin films over large areas, these methods usually require more sophisticated vacuum equipment and longer processing times which could potentially hinder their application for the low-cost fabrication of PSCs (Z. Li et al. 2018).

1.5.2 Production of a tandem cell

For a tandem cell we need to stack a cell over another. The materials must be compatible and the production process suitable. Until a few years ago there was a lack of efficient and low-cost solar cells that could be used in a tandem configuration with the PV technologies established in the market. However, the advent of perovskite solar cells and their rapid progress has changed this deadlock. The most common arrangement for tandem cells is to grow the cells layer by layer on a substrate and tunnel junctions connect the individual cells (Bremner, Levy, and Honsberg 2008). Solutions for metallisation, interconnection and module lamination for tandem solar cells are still at a very early research and development (R&D) stage. Since the perovskite material can't sustain the same mechanical and thermal stress as silicon, novel materials and processes must be developed. There are research centres like HelHelmholtz Zentrum Berlin (HZB) in Germany (Mariotti et al. 2022) or EnergyVille and Imec's in Belgium (Aernouts 2020) that are developing new manufacturing processes to bring the tandem cells and modules to technology levels ready for product integration. A collaboration of HZB and South Korea-based Qcells established a pilot manufacturing line for silicon-perovskite tandem cells in Thalheim, Germany. The project name is PEPPERONI "Pilot line for European Production of PEROvskite-Silicon taNdem modules on Industrial scale" aims to speed up the technology's mass manufacturing and market penetration (Qcells 2022). An ITO layer

forming the recombination junction between the bottom Si and the top perovskite cell is sputtered. Then the perovskite precursor layer is spin coated. A process similar to the typical spray coating of a normal perovskite cell but with the application of a rotation to have an uniform thin film. The photoactive perovskite crystal structure is formed through annealing (Mariotti et al. 2022). This process is easy and use already known techniques. Another innovation is given by the Solar Energy Research Institute of Singapore (SERIS) with the help of the Dutch start-up SALD BV. SALD BV has developed a unique worldwide patented technology for applying coatings with thickness lower than 1 nm on an industrial scale. This technology is called "Spatial Atomic Layer Deposition" or SALD. The solar cell manufacturers will be able to use SALD technology making a licensing agreement. This technology could boost the rise of the tandem cells (IST 2022). The present study is taking place at ELIS the department of Electronic and Information System of Ghent University, a photonic research centre that will give a contribution for the solar panels technology in the next years. The existing and well known perovskite production technologies are a good foundation for the development of the tandem cell production as they could be further implemented or applied directly. The Nord Europe is heavily investing on this sector therefore the major solar cells companies will establish a strong relationship and communication with the research centres that provide an important scientific knowledge.

1.6 Solar cell market

Mostly of the solar cells are in crystalline silicon (c-Si) that account for the 95% of the global market. Other options are CIGS (copper, indium, gallium and selenium) and CdTe solar cell. Power generation from solar panels increased by a record 179 TWh in 2021, marking 22% growth on 2020. Solar panels accounted for 3.6% of global electricity generation and it remains the third largest renewable electricity technology behind hydropower and wind (IEA 2022). The perovskite cells are rising up and replacing the solar system in the present market or are integrating them to give more efficient and cheaper products. The Si cell is the leading technology because the silicon is abundant and the wafers are easy to obtain with the Czochralski method, instead the critical elements as tellurium (CdTe case), gallium, and indium (CIGS case) are less available. To put it into perspective the materials production and availability, Jean et al. assume a 25 TW solar plant installation, for CdTe it would require the amount of tellurium equal to 1500 times the current annual global production. For silicon (c-Si case) this would amount to the equivalent of years of current global production and for lead (perovskite case) only days (Wojciechowski, Forgács, and Rivera 2019). The differences are large.

Cai et al. (2017) analysed two perovskite modules that are experimental manufactured. The cell in Module A based on a mesoporous structure can be fabricated by using a series of simple techniques based mainly on-screen printing to produce modules with efficiency of 15%. The cells in Module B based on a precise structure were

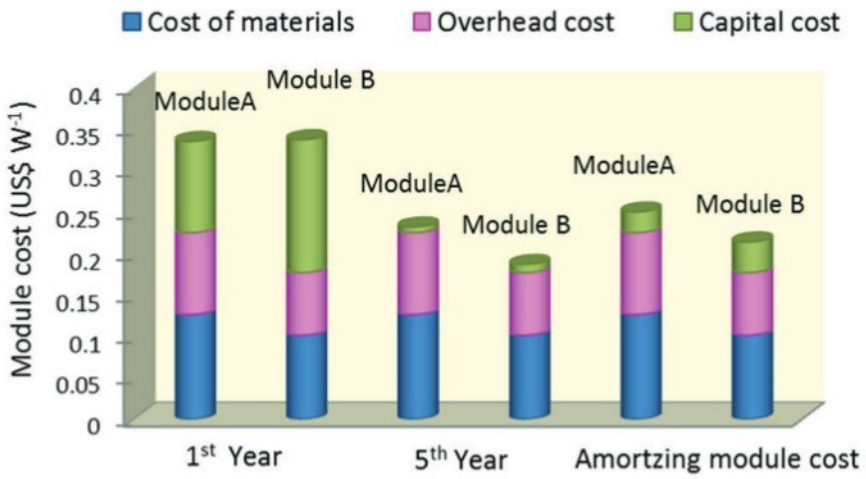

Figure 1.14. Calculated modules costs of PSCs. (Cai et al. 2017)

composed of several layers of high-quality thin films to produce highly efficient modules about 20%. The Module A has higher cost in materials and in overhead costs, instead the Module B has higher initial capital cost associated with the use of the high-vacuum machines. In conclusion the cost of Module B and that of Module A are almost the same. The amortizing module costs were calculated and showed in Figure 1.14. The Module A costs 0.250 US$ and Module B 0.215 US$ which are one third of module cost of bulk silicon solar cells. The previous study allows to predict that the module costs increase exponentially as their module efficiency decreases (Fig. 1.15). If we further extend the solid line, i.e., the Cai et al. (2017) study, the module costs of Module A and Module B are getting closer under the same module efficiency (dash line of Fig. 1.15). This result revealed that the module efficiency acted as an important factor for module cost no matter which route was used for manufacturing. Improvement of the cell efficiency and active area by upgrading precision of printing method for further increase of the module efficiency is effective way to reduce the cost of solar cell module (Cai et al. 2017).

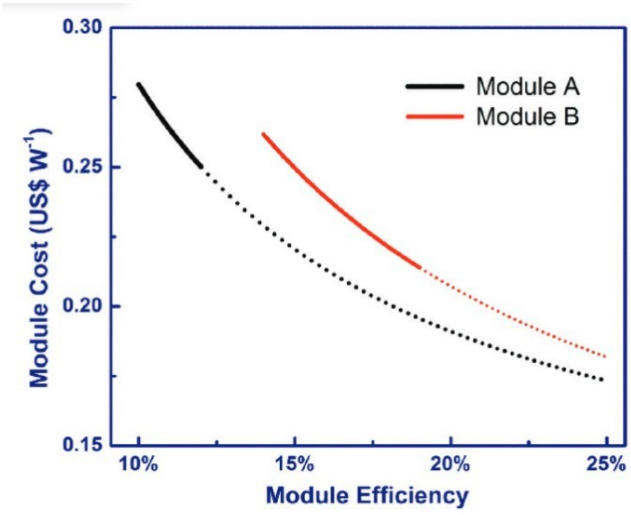

Figure 1.15. Module cost of PSCs as a function of module efficiency. (Cai et al. 2017)

Coupling cells to create a tandem cell is an effective way to increase the cell efficiency, so this approach should be also effective to decrease the amortizing module costs. However, the tandem cells are still under development and not already ready to enter prominently in the market. The market is waiting for new technology that could reduce the costs and make the solar cells renewable energy resource fully available.

1.7 Perovskite advantages, limits and solutions

The perovskite material has many advantages that in different field of application thanks to his unique properties. The structure and the chemical composition can be easily modified. The replacement of ions alters the size of the perovskite crystal lattice and its properties. This useful characteristic makes perovskite one of the most studied materials in the last decade especially in the energy field. Perovskite is a hybrid type material which sums up the advantages of both classes of semiconductors organic and metallic. Perovskite has some limitations that must be overcome. The toxicity and the instability are the most relevant disadvantages for its application (Zekry, Yahyaoui, and Tadeo 2019).

1.7.1 Advantages

The main advantages of perovskite related to the energy production especially concerning solar panels are:

- Inexpensive to produce using simply ink production methods, the low-cost materials and the deposition that can be done at near to room temperature (Aernouts 2020).
- The perovskite solar panels have large absorption coefficient and hence it requires thin film material to absorb the incident solar radiation compared to lower absorption coefficient candidates for the same solar cell efficiency. As absorber layer in the solar cell has thickness lower than 1 μm, that is more than 100 times lower than the current Si cell (Zekry, Yahyaoui, and Tadeo 2019). The panels are light weight and could be flexible. Two characteristics for promising application such: portable and wearable electronics, power-generated textiles, building-integrated photovoltaic systems, electric means of transport, and in space industry (Fu et al. 2018) (Ilic 2020).
- Large carrier mobility and dielectric constant that allow the formation of excitons and the dissociation in free electrons and holes (Zekry, Yahyaoui, and Tadeo 2019).

- Perspective of high power conversion efficiency (Zekry, Yahyaoui, and Tadeo 2019).
- Perovskite is light weight and flexible. Two characteristics for promising application such: portable and wearable electronics, power-generated textiles, building-integrated photovoltaic systems, electric means of transport, and in space industry (Fu et al. 2018) (Ilic 2020).
- The energy payback time could be up to ten times shorter than current industrial Si PV modules (Aernouts 2020).
- Perovskite has ease tuneability band gap, rages from 1.1 eV to 3.2 eV. The bandgap of most perovskites can be tuned simply by varying their chemical composition. The most commonly used monolithic cells has energy band gap of 1.55 – 1.60 eV. For tandem application with crystal Si (c-Si) or copper indium gallium selenide (CIGS) a band gap between 1.7 – 1.8 eV is preferable (Aernouts 2020).
- The perovskite can be assembled into panels that can replace or integrate as the top component of a tandem device without damaging the bottom cell thus increase the efficiency by several percent of today's panels without additional cost (Aernouts 2020).
- Perovskite exhibits exceptionally low sub-gap absorption, i.e., the absorption by defect states and band edge tails, necessary to have high efficiency solar panels (Wali et al. 2018).

1.7.2 Limitations and solutions

The main limitations and possible solutions of perovskite application in solar panels are:

- Thermal and moisture instability. The solutions could be the use of thermally resistant materials and modified perovskite (2D perovskites) (Wang et al. 2019).
- Performance dropping down to 80% of their initial efficiency after 1–2 years, compared to commercial Si PV technologies lasting more than 25 years (Llanos et al. 2020).

- When perovskite cells are assembled in modules, the modules lose about 8 – 9% of the perovskite cell initial efficiency (Llanos et al. 2020).
- The best perovskites at generating energy contain lead which is toxic for humans and environment. However, the Pb pollution from perovskite photovoltaics is smaller in comparison with the pollution generated from non-renewable sources required to supply the electricity needs. Moreover, the perovskite can use secondary sources of lead instead of mining. Lead can be easily extracted from the disposed lead-acid battery which is more environmentally friendly and reduces the risk of lead leakage from the disposed battery. However, lead free perovskites are currently under investigation (Llanos et al. 2020).
- In a tandem cell, solutions for metallisation, interconnection and module lamination are still at early research and development stage (Aernouts 2020).

1.7.3 Why use a perovskite in a tandem cell

The top cell of a tandem cell must be compatible with the bottom cell. Top cell must absorb part of solar light to generate electricity but also must be transparent to let through light which will be absorbed by bottom cell. Mechanical compatibility is required for all stack to ensure no cracking with a temperature change. The perovskite is the suitable

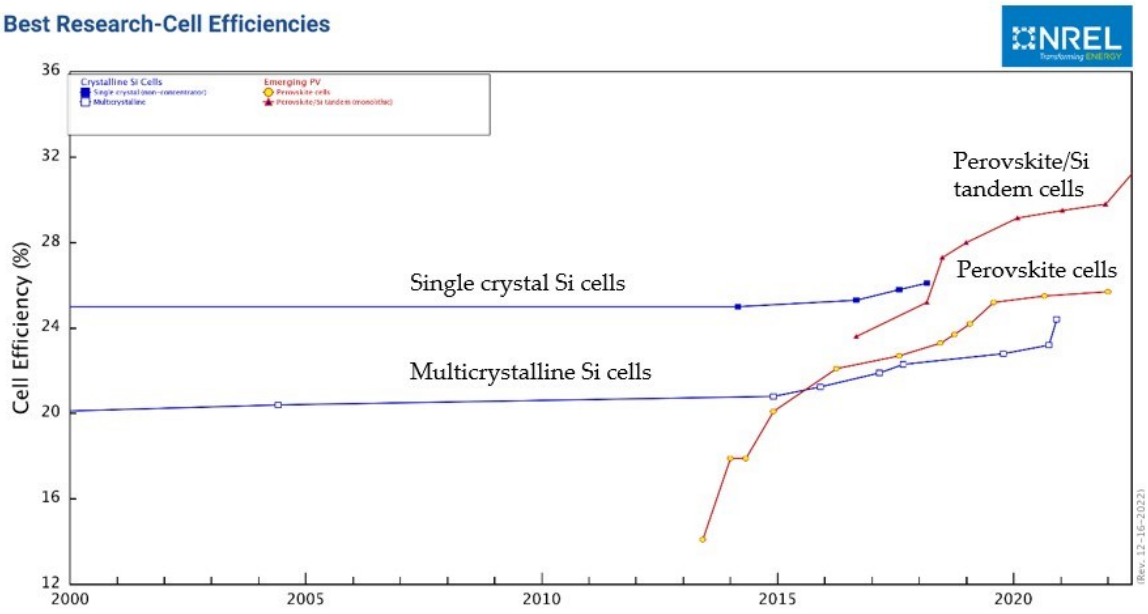

Figure 1.16. Chart record research cell efficiencies for Si single crystal (non-concentrator) cells, Si heterostructures (HIT) cells, perovskite cells, and perovskite/Si tandem cells in the last 22 years. (NREL 2022)

material for a Si tandem cell as it has all these characteristics. The perovskite band gap can be tuned in accordance with the Si bottom cell to give the max PCE possible. The absorption coefficient of the perovskite is higher than that of Si for lower photons wavelength where the solar power is higher. For longer wavelength, the perovskite is transparent, so the Si cell complete the light utilization with reduced waste of energy. The thermalization and transmission losses are reduced and the Shockley-Queisser limit for a monolithic cell can be surpassed. The perovskite cells alone, even if their performance has grown considerably are not competitive with the Si cells so the tandem cells are highly recommended to use the best properties of both materials (Fig. 1.16). The perovskite cell PCE record is 23.7% (Green et al. 2022), the crystalline Si cell record is 26.7% (Green et al. 2022), and the tandem perovskite/Si record is 31.25% (EPFL 2022). The perovskite top cell could be mechanically stacked over a silicon bottom cell by applying a pressure over the contact area between the two sub-cells as it is reported by Lamanna et al. (2020) The ''mechanical stacking approach'' proposed is a good alternative to the perovskite deposition process over the Si cell as it does not require a polished front surface of the bottom cell. Moreover, the cells could be independently fabricated giving full freedom to choose the production cell process. Lamanna et al. (2020) also evaluated the long-term stability of the mechanical staking. It exhibited a similar degradation trend as a single perovskite cell, it exceeded the expectations. The contacts in the interface does not represent a problem in stability for a tandem configuration.

CHAPTER 2 – SCAPS AND METHODOLOGY

2.1 SCAPS working principle

Solar Cell Capacitance Simulator SCAPS (3.3.10 version) is a one dimensional solar cell simulation program written in C code developed at the department of Electronics and Information Systems (ELIS) of the University of Gent, Belgium. The program is freely available to the photovoltaic (PV) research community (universities and research institutes). Some of SCAPS main features that can be manipulated relevant for my work are:

- Device configuration up to 7 semiconductors layers
- Almost all parameters of can be graded:
    - Energy band gap Eg,
    - Electron affinity X,
    - Relative dielectric permittivity ε,
    - Effective density of states in conduction band N_C,
    - Effective density of states in valence band N_V,
    - Electron/Hole thermal velocity v_{thn} /v_{thp},
    - Electron/Hole mobility μ_n/μ_p,
    - Shallow uniform donor density N_D,
    - Shallow uniform acceptor density N_A,
    - Trap defects total density N_t
- Defect levels: in bulk or at interface
- Defect levels, energetic distributions: single level, uniform, Gauss, tail, or combinations
- Contacts: work function or flat band
- Illumination: AM1.5G spectrum (solar spectrum filtered by the atmosphere), AM1.5 1 sun spectrum (solar spectrum) and other spectra
- Absorption: perovskite, Si and others absorption coefficient
- Working point for calculations: voltage, frequency, temperature

- Batch calculations possible; presentation of results and settings as a function of batch parameters
- Loading and saving of all settings

SCAPS will work on using the basic semiconductor equations such as Poisson equation, continuity equation of electrons and holes. It calculates energy bands, concentrations and currents at a given working point, current density-voltage (J-V) characteristics, and spectral response (Burgelman M., Nollet, and Degrave 2000). SCAPS is well adapted for modelling of various micro and polycrystalline thin films devices and photonic structures. Thus, it can be used to simulate the perovskite solar cell architectures. From the literature, experimental results are coinciding with the simulated results of the SCAPS, to design and develop high efficiency solar cells (Mandadapu and Babu 2017).

The working points are fixed for all simulations:

- Temperature = 300 K
- Voltage = 0 V
- Frequency = 1×10^6 Hz
- Number of points = 5

The solar spectrum can be chosen. The result of the simulation will be displayed and can be saved (Burgelman M., Nollet, and Degrave 2000).

2.2 Methodology

From reference paper concerning a high performance tandem cell with a wide band gap perovskite top cell (D. Kim et al. 2020), the solar cells are modelled in order to have the same performance. The top and the bottom cells are studied separately. To simulate the cell in SCAPS the materials parameters as Eg, X, ε, N_C, N_V, v_{thn}, v_{thp}, μ_n, μ_p, N_A, N_D, N_t are needed. The cells are created starting from "flat band" contacts, the absorber layer, the Hole Transport Layer (HTL) and the Electron Transport Layer (ETL) and then one layer at a time is added. Each material is studied and the most realistic parameters are chosen in order to have a feasible and efficient cell in accordance with the reference paper. Once the cell is made and is in agreement to reported literature, the next cell is added on to the structure. The procedure is repeated until the cell is completed.

2.2.1 Reference paper

It is reported by D. Kim et al. (2020) the experimental result of a 2 terminal Perovskite/Si (2T) tandem device that achieved 26.7% of Power Conversion Efficiency (PCE). It is reported that the highest PCE of tandem Perovskite/Si (2T) measured under the global AM1.5 spectrum (1000 W m^{-2}) at 25 °C (IEC 60904-3: 2008 or ASTM G-173-03 global) is 29.8% (Green et al. 2022). In the selected paper, the PCE is lower, but the perovskite has 1.68 eV energy band gap and it is needed to create a useful top cell model for the next tandem cell. In a material with such a wide energy gap, all photons with energy higher than Eg are absorbed and transmits all photons with smaller energy that are then absorbed by the bottom cell material with lower Eg. In this way all the energy from the sun could be utilized (Würfel and Würfel 2016). The perovskite used by D. Kim et al. (2020) is $(FA_{0.65}MA_{0.2}Cs_{0.15})Pb(I_{0.8}Br_{0.2})_3$. The replacement of I with Br by more than 20% is necessary to enlarge the bandgap to 1.68 eV and a mixture of thiocyanate (SCN) with iodine is used to overcome the instability issue.

The reference cells structures and performances are reported in the Table 2.1. The top cell performance is deduced from Fig.1 C of D. Kim et al. (2020) study. It is reported a cross-sectional scanning electron microscope (SEM) image (Fig. 5 A of D. Kim et al. (2020)

study) that shows the thickness of the device layers. The thickness of the layers taken from the SEM image will be around 500 nm for perovskite, 30 nm for C_{60} with PEIE, 150 nm for ITO (C_{60}), 30 nm for PTAA with ITO (PTAA). These are the only guidelines to build the cells.

Table 2.1. Reference cells structures and performances taken from D. Kim et al. (2020).

Reference cells	PCE (%)	V_{OC} (V)	J_{SC} (mA/cm²)	FF (%)
Tandem cell: Si cell/ITO/PTAA/perovskite/C_{60}/PEIE/ITO/ Ag	26.7	1.756	19.2	79.2
Top cell: ITO/PTAA/perovskite /C_{60}/BCP/Ag	20.7	1.22	21.2	80
Bottom cell under AM1.5G: ITO/*n*-a-Si:H/*n*-c-Si/*p*-a-Si:H/ITO	17.28	0.644	35.11	76
Bottom cell under filtered spectrum: ITO/*n*-a-Si:H/*n*-c-Si/*p*-a-Si:H/ITO	9.36	0.624	19.32	78

2.2.2 Top cell

The top cell is a perovskite cell with Eg = 1.68 eV. The estimated thicknesses of the layers are taken from SEM image (Fig. 5 A of D. Kim et al. (2020) study) and adjusted in the way the cell could work properly. Most of interest is given to Eg, X, N_A, and N_D, as they are the most effective parameters for the cell performance. The energy bad gap Eg and the electron affinity X are essential to build an efficient energy band diagram that allow the comprehension of the electron and holes transportation from the absorber layer to de contacts. The doping concentration N_A and N_D are adjusted by chemical methods by the companies and they give to the material the property to be HTL or ETL. The electrical conductivity is heavily influenced by the doping concentration (L. Li, Meller, and Kosina 2007). The batch simulations of SCAPS are useful to see how the performance changes with respect of these parameters. The value of the bulk defect density N_t is never "zero" as every material has always some defects that induce recombination and decrease the performance. The electron and hole mobility μ_n and μ_p, and the dielectric constant ε do not affect the performance as the other parameters mention before do. The electron and hole thermal velocity v_{thn} and v_{thp} are the least relevant parameters. The top cell is simulated

under AM1.5G spectrum (spectrum of the sun filtered by the atmosphere) and the current density-voltage (J-V) curve analysed. The objective is to model a cell with ITO/PTAA/perovskite/C_{60}/PEIE/ITO configuration type that gives performance similar to the top cell of the reference paper (Table 2.1 of Section 2.2.1). A further study is carried out to verify what materials could be adopted for the front and back contacts. An outlook of the role of the *Eg* and thickness on the performance is given at the end.

2.2.3 Bottom cell

The bottom Si cell has narrow energy gap of 1.12 eV as the most cell used in the market. As this cell is not the main objective of this study, it is modelled in a simplified way composed only with the absorber, HTL and ETL layers. The thickness of the layers is studied and estimated with respect to D. Kim et al. (2020b). The parameters are chosen and studied in the same way of the top cell. The bottom cell with crystalline Si (c-Si) as absorber layer and hydrogenated amorphous Si (a-SI:H) as HTL and ETL is simulated under AM1.5G 1 sun spectrum and under the transmitted filtered spectrum of the top cell to derive essential current matching conditions necessary for the construction of tandem current density–voltage (J–V) curve. The filtered spectrum is calculated from the equation

$$P(\lambda) = P_0(\lambda) \cdot exp\left(\sum_{i=1}^{n} -\alpha_{mat_i}(\lambda) d_{mat_i}\right)$$

(Eq. 2.1)

where $P_0(\lambda)$ is the power density (W m^{-2}) of the incident light, $P(\lambda)$ is the power density (W m^{-2}) filtered spectrum from the top cell, mat_i represents the specific material, $\alpha(\lambda)$ is the absorption coefficient, and d represents the thickness of a given device layer (Madan, Singh, and Pandey 2021). The J-V curves are analysed and the effect of the top cell studied. The reference performance is reported in Table 2.1 of Section 2.2.1 (D. Kim et al. 2020b). It is expected that the performance of the Si cell under filtered spectrum illumination will not be the same of the reference paper, especially for the J_{SC}, as the calculated filtered spectrum might be different.

2.2.4 Tandem cell

Two terminal monolithic tandem solar cell structure resembles the architecture of series-connected diodes in which the cell with minimum current limits the maximum current, i.e., tandem J_{SC}, whereas the V_{OC} is the sum of the individual V_{OC} of the cells. Mathematically (Madan, Singh, and Pandey 2021), in standalone condition

$$J_{SC}\ (\text{tandem}) \approx \min\{J_{SC}\ (\text{top}), J_{SC}\ (\text{bottom})\}$$

(Eq. 2.2)

$$V_{OC}\ (\text{tandem}) \approx V_{OC}\ (\text{top}) + V_{OC}\ (\text{bottom})$$

(Eq. 2.3)

This approach is widely adopted by the researchers designing tandem solar cells using SCAPS (Madan, Singh, and Pandey 2021).

The FF can be estimated with:

$$FF\ (tandem) = \frac{v_{OC}\ (tandem) - ln(v_{OC}\ (tandem) + 0.72)}{v_{OC}\ (tandem) + 1}$$

(Eq. 2.4)

where v_{OC} is defined the "normalized V_{OC}":

$$v_{OC}(tandem) = \frac{q}{nkT}\ V_{OC}\ (tandem)$$

(Eq. 2.5)

where q the elementary charge, k is the Boltzmann's constant, T the absolute temperature, n is the ideality factor which in a typical device ranges from 1 to 2 (Saleh and Vide 1981).

From this data the PCE can be calculated with (Khelifi 2009)

$$PCE\ (tandem) = \frac{J_{SC}\ (tandem) \cdot V_{OC}\ (tandem) \cdot FF\ (tandem)}{P_{inc}}$$

(Eq. 2.6)

The J-V characteristic of the tandem cell in relation with the top and the bottom cell can be obtained. The reference performance is reported in Table 2.1 of Section 2.2.1. It is expected that the performance of the tandem cell will not be the same of the reference paper as the Si cell under filtered spectrum illumination might has different performance from the reference paper.

CHAPTER 3 - PEROVSKITE TOP CELL

3.1 PTAA/perovskite/C_{60}

The SCAPS parameters for the first three layers PTAA/perovskite/C_{60} are reported by Diekmann et al. (2021). The cell simulated is similar to the one of the reference paper. The cell structure is ITO/PTAA/PFN-Br/perovskite/C_{60}/BCP/Cu with performance simulated in SCAPS: PCE ~19.2%, V_{OC} = 1.13 V, J_{SC} = 21.5 mA cm^{-2}, and FF = 79%. In the paper there are all the parameters of PTAA, perovskite and C_{60} except for:

1. The donor density of PTAA N_D *(PTAA)* and the acceptor density of C_{60} N_A *(C_{60})*
2. The mobility of the minority carriers of PTAA and C_{60} μ_n *(PTAA)* and μ_p *(C_{60})*
3. The interface defects

The thickness of the layers is comparable to that of the SEM image of D. Kim et al. (2020), only the perovskite thickness is lower 400 nm instead of the measured 500 nm, the role of perovskite thickness is studied and reported in the report in Section 3.9. The perovskite energy gap is 1.63 eV instead in the reference paper is 1.68 eV (D. Kim et al. 2020), so the role of perovskite energy gap is studied and reported in the report in Section 3.9.

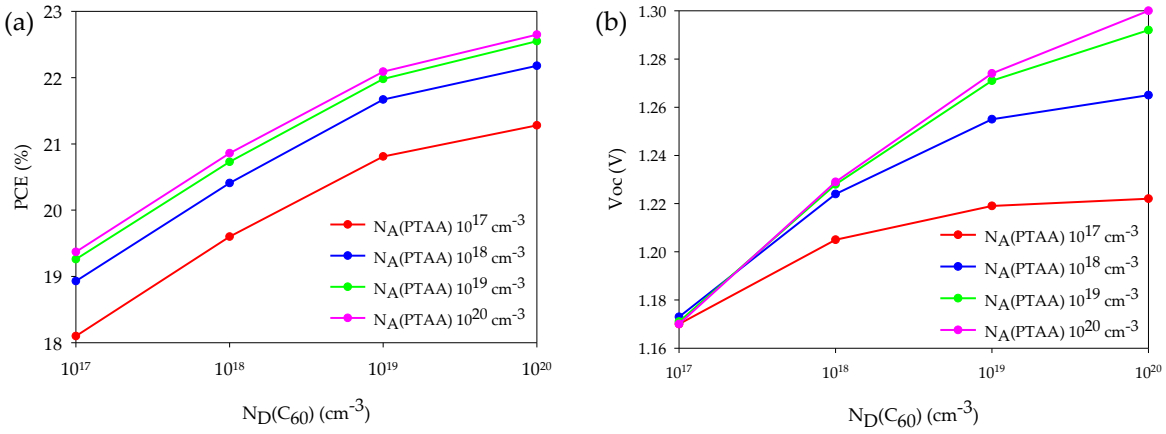

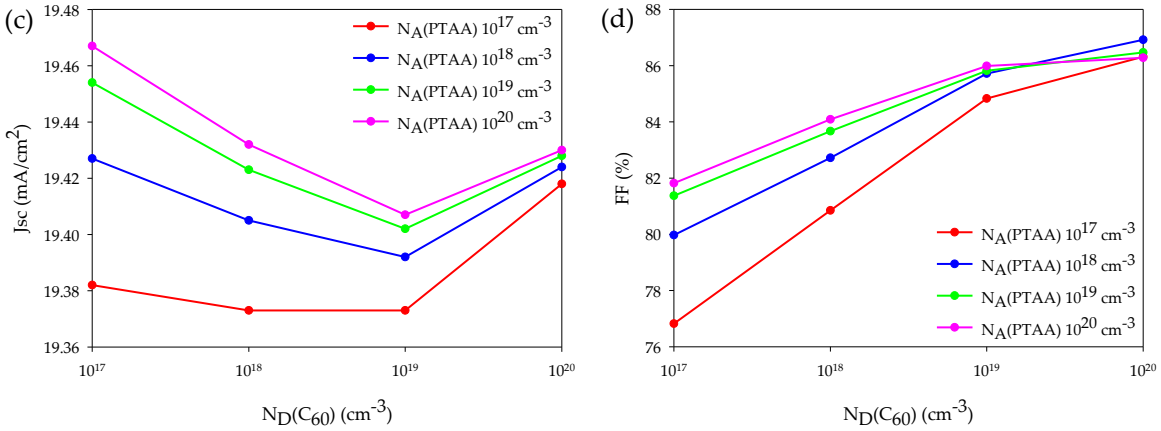

Figure 3.1. Batch simulation of flat band/PTAA/perovskite/C_{60}/flat band varying N_A(PTAA) and N_D(C_{60}) from 1x 10^{17} cm^{-3} to 1 x 10^{20} cm^{-3} under AM1.5G spectrum. (a) PCE plot, (b) V_{OC} plot, (c) J_{SC} plot and (d) FF plot. Data reported in figure are obtained from the SCAPS simulator.

The first unknown parameters $N_A(PTAA)$ and $N_D(C_{60})$, i.e., the minority carrier density of PTAA and C_{60} respectively, are chosen doing a batch simulation in SCAPS under AM1.5G spectrum of flat band/PTAA/perovskite/C_{60}/flat band with neutral interface defects where $N_A(PTAA)$ and $N_D(C_{60})$ were varied from 1x 10^{17} cm^{-3} to 1 x 10^{20} cm^{-3} (Fig. 3.1).

Table 3.1. Performance comparison. Data reported from D. Kim et al. (2020) and SCAPS simulator.

	PCE (%)	V_{OC} (V)	J_{SC} (mA/cm²)	FF (%)
Reference cell: ITO/PTAA/PFN-Br/perovskite/C_{60}/BCP/Cu	19.2	1.13	21.5	79
SCAPS cell: flat band/PTAA/perovskite/C_{60}/flat band	19.60	1.205	19.373	80.85
SCAPS Data / Ref. Data – 1 (%)	+2.08	+6.63	-9.89	+2.34

Looking to the batch simulation results with N_D = 1 x 10^{18} cm^{-3} and N_A = 1 x 10^{17} cm^{-3}, we are close to the reference performance especially for the PCE and FF but also for V_{OC} (Table 3.1). Moreover, the realistic values of N_A and N_D are reported by Turedi et al. (2021); N_D = 2 x 10^{18} cm^{-3} and N_A = 2 x 10^{17} cm^{-3} were selected for C_{60} and PTAA respectively.

For the second problem, it was proved with batch simulation (Fig. 3.2 and 3.3) that the mobility of the minority carriers μ_n *(PTAA)* and μ_p *(C60)* has not a big impact on the performance. The PCE decreases only by 0.00002% increasing the μ_n *(PTAA)* by five orders of magnitude. The PCE increases by about 0.8% increasing the μ_p *(C60)* by five orders of magnitude. Therefore, it has been decided to use the same mobility of the majority carriers μ_p *(PTAA)* and μ_n *(C60)* given by Diekmann et al. (2021): μ_p *(PTAA)* = 1.5 x 10^{-4} = μ_n *(PTAA)*; μ_n *(C60)* = 1 x 10^{-2} = μ_p *(C60)*.

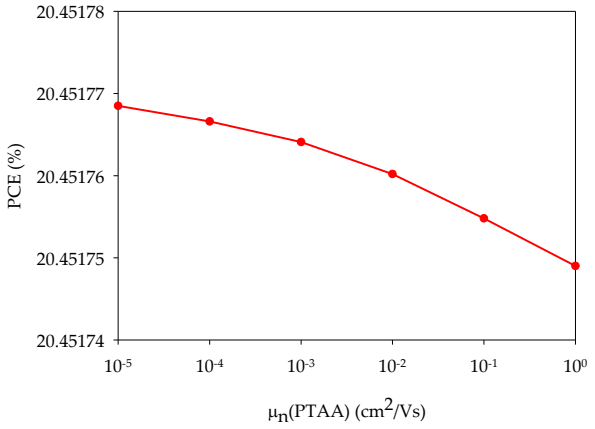

Figure 3.2. Batch simulation varying μ_n (PTAA) from 1 x 10^{-5} to 1 x 10^0 cm^2/Vs. Data reported in figure are obtained from the SCAPS simulator.

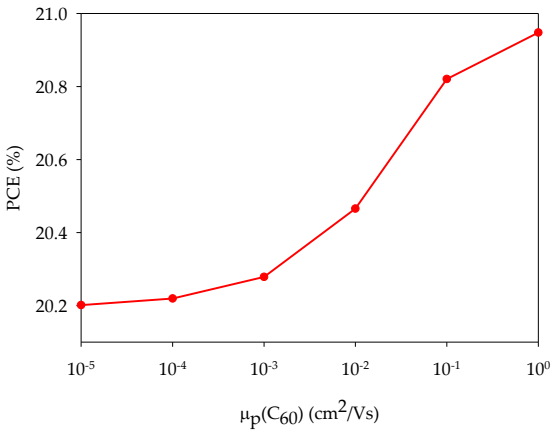

Figure 3.3. Batch simulation varying μ_p (C60) from 1 x 10^{-5} to 1 x 10^0 cm^2/Vs. Data reported in figure are obtained from the SCAPS simulator.

As the interface defects were not well described in Diekmann et al. (2021) work, three possible configurations were studied and reported, but at end only one gives good results: neutral interface defects. The three different configurations made with three different interface defects are simulated:

1. "Neutral" where the charge type is neutral;
2. "Minority" where the charges are donors for PTAA/Perovskite interface and acceptors for C_{60}/Perovskite interface;
3. "Both charges" where every interface defect is made by two defects: one with acceptors and one with donors type of charge.

From the SCAPS simulations (Table 3.2) we can see that the performance is good only for one type of configuration: neutral interface defects.

Table 3.2. Interface defects simulations. Data reported are obtained by SCAPS simulator.

Configuration type	PCE (%)	V_{OC} (V)	J_{SC} (mA/cm^2)	FF (%)
Neutral	20.45	1.221	19.498	82.70
Minority	15.15	1.040	19.717	71.13
Both charges	Convergence error: SCAPS is not able to calculate			

The perovskite absorption interpolation models used is taken from Löper et al. (2015) and for PTAA and C_{60} it is used the *sqrt(hv-Eg) law*.

All the parameters of the materials and interface defects are reported in the Tables 3.3 and 3.4.

Table 3.3. PTAA, perovskite and C_{60} SCAPS parameters.

Parameters	PTAA	Perovskite	C_{60}
Thickness (nm)	10	400	30
Bandgap (eV)	3.00	1.63	2.00
Electron affinity (eV)	2.50	3.90	3.90
Dielectric permittivity (relative)	3.50	22.00	5.00
CB effective density of states (cm^{-3})	1.0×10^{20}	2.2×10^{18}	1.0×10^{20}
VB effective density of states (cm^{-3})	1.0×10^{20}	$2.2\ 10^{18}$	1.0×10^{20}
Thermal velocity hole and electron	1.0×10^{7}	1.0×10^{7}	1.0×10^{7}
Electron mobility (cm^2/Vs)	1.5×10^{-4}	1.0	1.0×10^{-2}
Hole mobility (cm^2/Vs)	1.5×10^{-4}	1.0	1.0×10^{-2}
Donor density N_D (cm^{-3})	0	1.0×10^{12}	2.0×10^{18}
Acceptor density N_A (cm^{-3})	2.0×10^{17}	1.0×10^{12}	0
Defect density N_t (cm^{-3})	1.0×10^{18}	2.0×10^{15}	1.0×10^{18}
References	Diekmann et al. (2021), Turedi et al. (2021)	Diekmann et al. (2021)	D. Kim et al. (2020), Turedi et al. (2021)

Table 3.4. PTAA, perovskite and C_{60} SCAPS defects parameters.

Parameters	Bulk PTAA	Bulk perovskite	Bulk C_{60}	PTAA/perovskite interface	C_{60}/perovskite interface
Defect type	Neutral	Neutral	Neutral	Neutral	Neutral
Capture cross section (cm^2)	1.0×10^{-16}	1.0×10^{-16}	1.0×10^{-16}	1.0×10^{-16}	1.0×10^{-16}
Energetic distribution	Single	Gaussian	Single	Single	Single
Reference energetic level	Above E_V	Above E_V	Above E_V	Above the highest E_V	Above the highest E_V
Energy level (eV)	0.6	0.6	0.6	0.6	0.6
Characteristic energy (eV)	-	0.1	-	-	-
Defect density N_t (bulk cm^{-3}) (interface cm^{-2})	1.0×10^{18}	2.0×10^{15}	1.0×10^{18}	1.0×10^{11}	$2.0\ 10^{12}$
References	Turedi et al. (2021)	Turedi et al. (2021)	Turedi et al. (2021)	Turedi et al. (2021)	Turedi et al. (2021)

3.2 PTAA and C_{60} observations

The parameters reported by Diekmann et al. (2021) are electron affinity of PTAA *X(PTAA)* = 2.50 eV and electron affinity of C_{60} *X(C_{60})* = 3.90 eV, but they are supposed to be and not measured, they are subjected to a further study.

The electron affinity of C_{60} is verified to be correct as 3.9 eV if instead of C_{60} is used C_{61}PCBM, i.e., a modification of C_{60} as it is reported by Schwenn, Burn, and Powell (2011). Also, the *Eg* = 2 eV, selected in the previous report Section Perovskite cell, is proper of C_{61}PCBM material as it is reported by Sun et al. (2016). On the other hand, the electron affinity (*X*) can be decreased up to 3.6 eV and a suitable candidate can be used. The demonstration is given by the batch simulation of flat band/PEDOT:PSS/PTAA/perovskite/C_{60}/PEIE/ITO/flat band varying the C_{60} electron affinity from 3.9 eV to 3.5 eV (Fig. 3.4). We can see that decreasing the *X* from 3.9 eV the performance increases until 3.7 eV. It is not possible to study the electron affinity lower than 3.6 eV as the SCAPS limitations are reached. However, *X* = 3.9 eV is selected. The performance is: PCE = 20.29%, V_{OC} = 1.202 V, J_{SC} = 21.044 mA cm^{-2}, and FF = 80.20%.

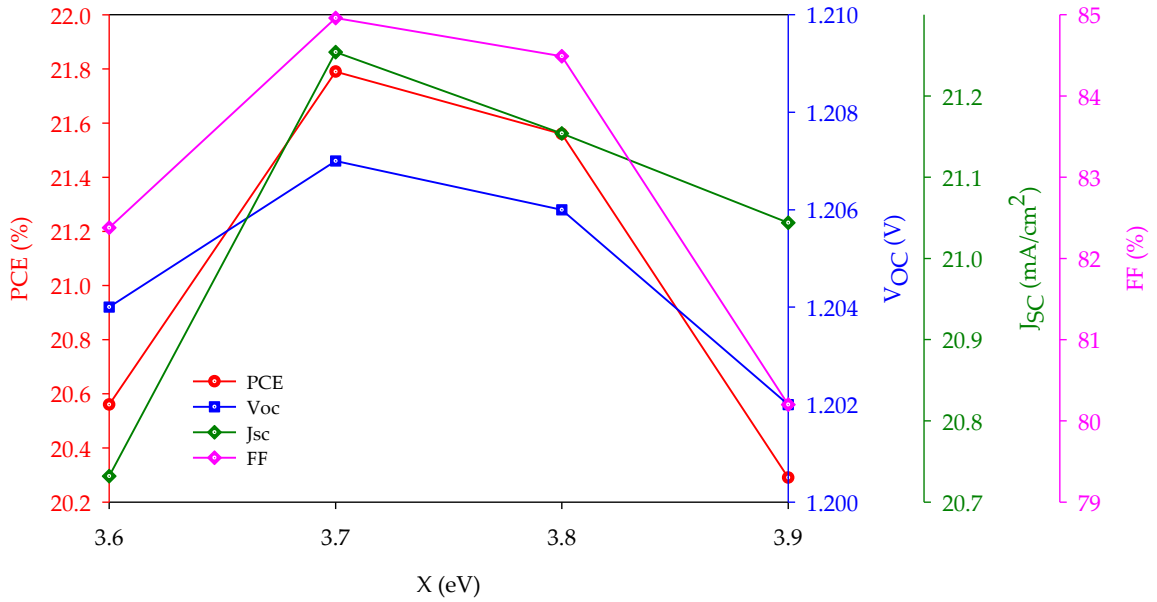

Figure 3.4. Batch simulation of flat band/PEDOT:PSS/PTAA/perovskite/C_{60}/PEIE/ITO/flat band varying C_{60} electron affinity (X) from 3.5 to 3.9 eV under AM1.5G spectrum. Data reported in figure are obtained from the SCAPS simulator.

The PTAA electron affinity reported by Diekmann et al. (2021) is 2.5 eV only because it is necessary to align the Highest Occupied Molecular Orbital level (*HOMO*) with the perovskite to have an efficient carrier collection. In the batch simulation of flat band/ PEDOT:PSS/PTAA/perovskite/C60/PEIE/ITO/flat band, the electron affinity is decreased from 2.7 eV to 1.7 eV (Fig. 3.5). The performance decreases lowering the *X* from 2.5 eV because the recombination increases as the Fermi level of perovskite (E_{Fn}) and the Fermi level of PTAA (E_{Fp}) are getting closer. It can be deduced that the *HOMO (PTAA)* and *HOMO (perovskite)* must be aligned, so the PTAA must have *HOMO* = *Eg* + *X* = 5.5 eV as *HOMO (perovskite)* = 5.58 eV. In reality, PTAA has *X* of 2.1 eV or 2.3 eV or lower, and *Eg* of 3.2 eV or 3.3 eV or higher as it is reported by Ravishankar et al. (2022) and by Jarwal et al. (2020), but Diekmann et al. (2021) reported a measured energy gap of 3 eV and then they used *X* = 2.5 eV to align the *HOMO* levels of perovskite and PTAA (*HOMO (perovskite)* = 5.58 eV). If PTAA/perovskite/C_{60} cell is simulated with *X (PTAA)* = 2.1 eV and *Eg (PTAA)*= 3.2 eV, *HOMO (PTAA)* = 5.3 eV, the performance is: PCE = 18.01%, V_{OC} = 1.062 V, J_{SC} = 21.023 mA cm^{-2}, and FF = 80.67%. If PTAA/perovskite/C_{60} cell is simulated with *X (PTAA)* = 2.3 eV and *Eg (PTAA)*= 3.3 eV, *HOMO (PTAA)* = 5.6 eV, the performance is: PCE = 19.77%, V_{OC} = 1.231 V, J_{SC} = 21.044 mA cm^{-2}, and FF = 76.36%. With these two simulations is proved the cell effectiveness with different PTAA parameters that could be useful for other configuration analysis. However, *X (PTAA)* = 2.5 eV is selected giving performance PCE = 20.45%, V_{OC} = 1.221 V, J_{SC} = 19.498 mA cm^{-2}, and FF 82.70%.

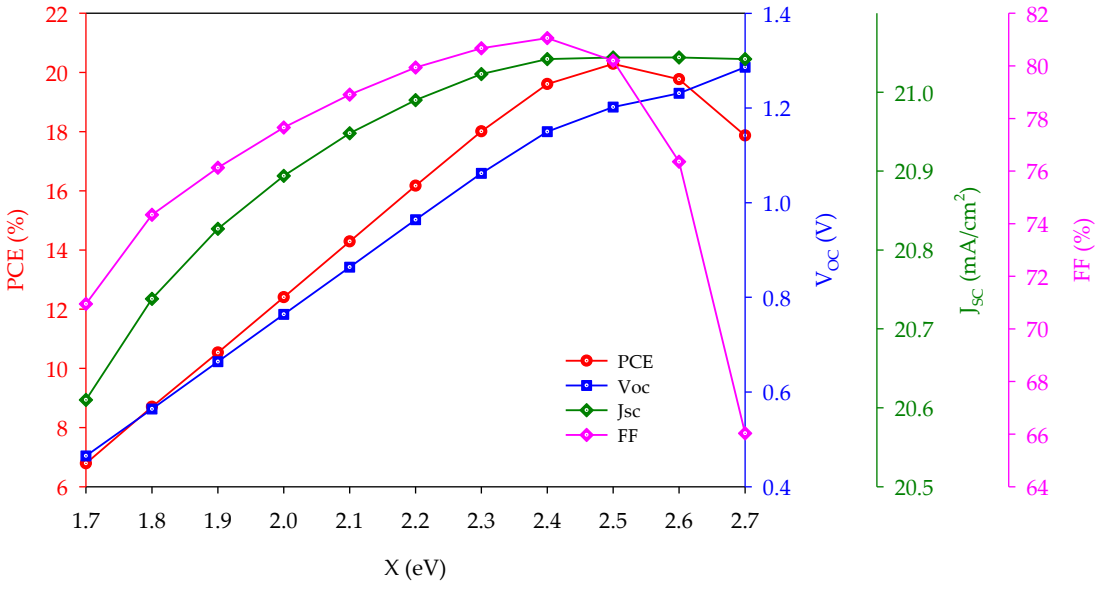

Figure 3.5 Batch simulation of flat band/PEDOT:PSS/PTAA/perovskite/C_{60}/PEIE/ITO/flat band varying PTAA electron affinity (X) from 1.7 to 2.7 eV under AM1.5G spectrum. Data reported in figure are obtained from the SCAPS simulator.

3.3 PEIE

The top cell is ITO/PTAA/perovskite/C_{60}/PEIE/ITO, so we move on from PTAA/perovskite/C_{60} adding the PEIE layer. As the information for PEIE material was limited. Further studies were carried to approximate its parameters.

The low-cost, nontoxic, and environment-friendly polyethylenimine ethoxylated (PEIE) contains simple aliphatic amine groups that can produce surface dipoles as is reported by X. Li et al. (2019). In Anefnaf et al. (2020) study it has been used as interlayer or buffer layer to reduce the work function (*WF*) of ITO and other oxide electrodes, hence improving the performance and stability of inverted devices. PEIE has also been applied to modify the recombination layer in high performance tandem organic solar cells. The experimental results given by P. Li et al. (2014) have confirmed that the influence of the PEIE is negligible on the optical transmittance, thickness of the active layer, and morphology of the ITO. For these reasons the PEIE layer will be not added in SCAPS but will be integrated in the ITO layer.

3.4 ITO (C_{60})

The ITO, in the *n* side of the cell, is 150 nm thick and the other parameters are taken from the study of Bendib et al. (2020). The energy gap (*Eg*) and electron affinity (*X*) are studied separately.

It is reported by Yu et al. (2016) that ITO has energy gap between 3.5 eV and 4.3 eV; *Eg* = 3.5 eV is selected.

Klein et al. (2010) demonstrated that the electron affinity of ITO can be manipulated from 4.2 eV to 5.3 eV via the deposition parameters over the dopant concentration. A batch simulation was done varying the *X* from 4.4 eV to 3.8 eV (Figure 3.6). It is demonstrated that *X* from 4.4 eV to 3.8 eV could be used. It can be used values lower than 4.2 eV because the PEIE layer reduce the work function, as it was documented in the previous Section 3.3. It was selected *X* = 4.1 eV. The performance under AM1.5G is PCE = 20.39%, V_{OC} = 1.222 V, J_{SC} = 20.174 mA cm^{-2}, and FF = 82.71%.

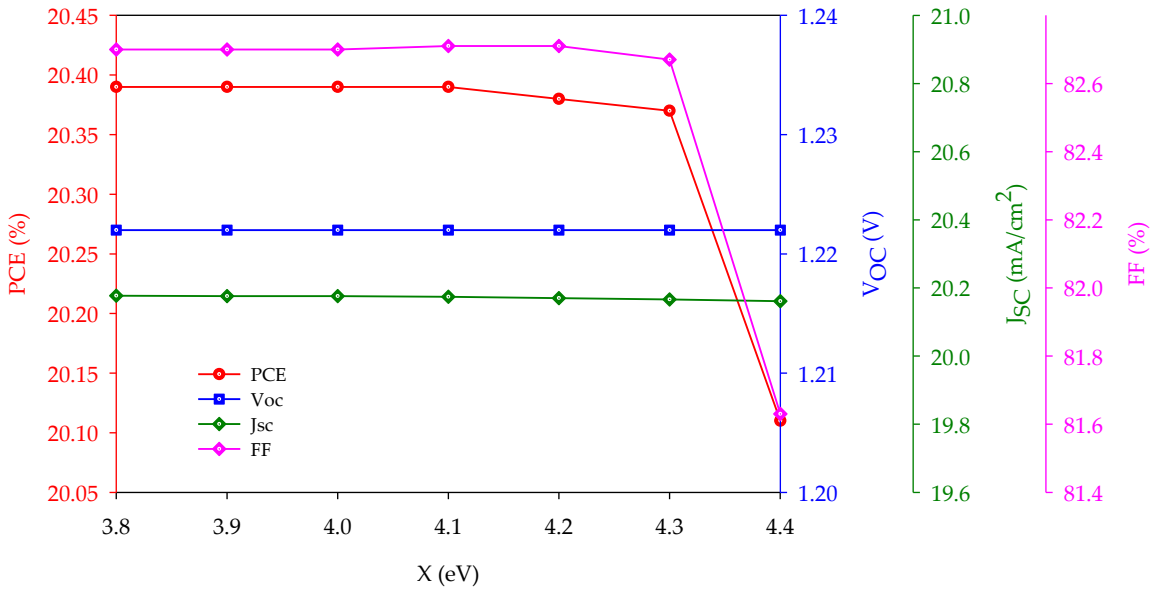

Figure 3.6. Batch simulation of flat band/PTAA/perovskite/C_{60}/PEIE/ITO/flat band varying ITO electron affinity (X) from 3.8 to 4.4 eV under AM1.5G spectrum. Data reported in figure are obtained from the SCAPS simulator.

The C_{60}/ITO interface defect is supposed to be the same of perovskite/C_{60} interface defect as they are in the same side of the cell, the *n*-side. The absorption interpolation model used for ITO is *sqrt(hv-Eg) law*.

All the material and defects parameters are reported in Tables 3.5 and 3.6.

Table 3.5. ITO SCAPS parameters.

Parameters	ITO (C_{60})
Thickness (nm)	150
Bandgap (eV)	3.50
Electron affinity (eV)	4.10
Dielectric permittivity	9.00
CB effective density of states (cm^{-3})	2.2×10^{18}
VB effective density of states (cm^{-3})	1.9×10^{19}
Thermal velocity hole and electron	1.0×10^{7}
Electron mobility (cm^2/Vs)	1.0
Hole mobility (cm^2/Vs)	1.0
Donor density N_D (cm^{-3})	1.0×10^{20}
Acceptor density N_A (cm^{-3})	0
Defect density N_t (cm^{-3})	1.0×10^{15}
References	Bendib et al. (2020), Yu et al. (2016)

Table 3.6. ITO defects SCAPS parameters.

Parameters	Bulk ITO	C_{60}/ITO interface
Defect type	Neutral	Neutral
Capture cross section (cm^2)	1.0×10^{-15}	1.0×10^{-16}
Energetic distribution	Single	Single
Reference energetic level	Above E_V	Above the highest E_V
Energy level (eV)	0.6	0.6
Defect density N_t (bulk cm^{-3}) (interface cm^{-2})	1.0×10^{15}	2.0×10^{12}
References	Bendib et al. (2020)	Assumed

3.5 PEDOT:PSS

For the ITO layer in contact with the PTAA layer it was used the same material parameters of the ITO (C_{60}) changing only N_A with N_D as ITO (PTAA) is in the *p*-side. The thickness measured from the SEM image reported by D. Kim et al. (2020) is supposed to be 5 nm. The SCAPS program is not able calculate the performance of the cell with electron affinity of ITO *X(ITO)* = 4.1 eV. The batch simulation (Fig. 3.7) shows that with electron affinity between 1.8 eV and 2.6 eV the cell has good performance, *X* in this range could be used, but there is no ITO in existence currently with such a low electron affinity.

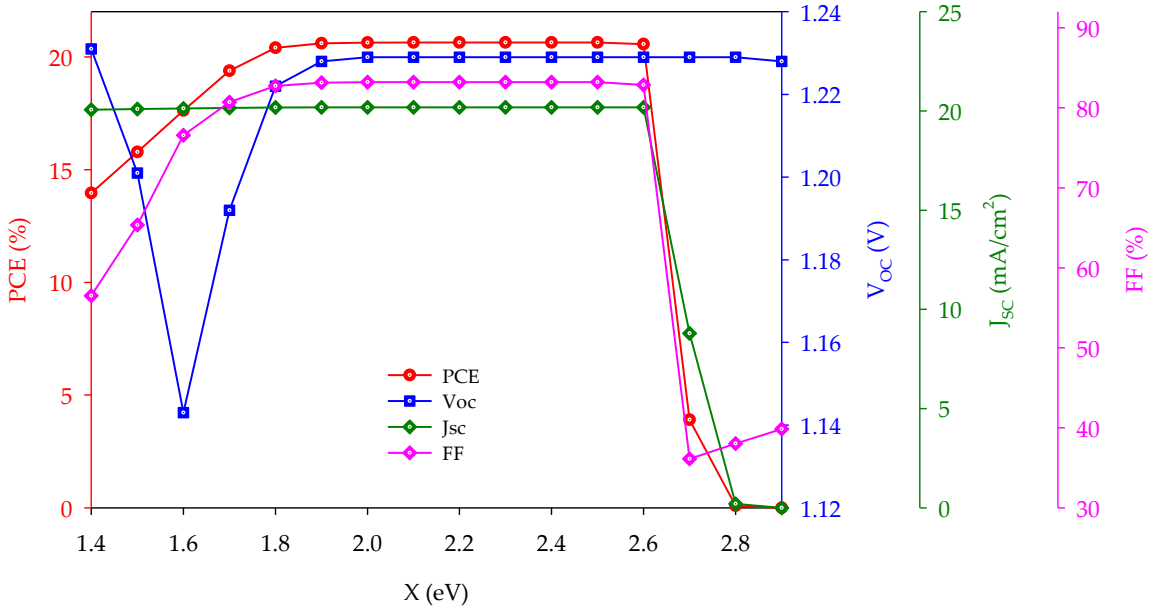

Figure 3.7. Batch simulation of flat band/ITO/PTAA/perovskite/C_{60}/PEIE/ITO/flat band varying electron affinity of ITO (PTAA) from 1.4 to 2.9 eV under AM1.5G spectrum. Data reported in figure are obtained from the SCAPS simulator.

A further analysis of the batch simulation showed that the *HOMO* level must be in the range of 5.3 – 6.1 eV. The calculation is *HOMO* = *Eg* + *X* = 3.5 eV + [1.8 – 2.6] eV = [5.3 – 6.1] eV. A transparent conducting oxide (TCO) material in this *HOMO* range is searched in literature. It was found the PEDOT:PSS material with *HOMO* = 1.8 eV + 3.4 eV = 5.2 eV that is 0.1 eV outside the range, but due to its different properties the cell works. The material parameters are taken from the study of Alipour and Ghadimi (2021). Alipour and Ghadimi (2021) also demonstrated that the PEDOT:PSS can replace ITO in tandem cells as recombination layer with a low temperature manufacturing process and low costs. Akln Kara et al. (2018) observed not only enhanced efficiency but also improved long-term

stability by a simple solution processed interfacial modification method using self-assembled monolayer (SAM). The interface PEDOT:PSS/PTAA defect is supposed to be the same of perovskite/PTAA interface defect as they are in the same side of the cell, the *p*-side. The absorption interpolation model used for PEDOT:PSS is *sqrt(hv-Eg) law*. The SCAPS simulation with flat band/PEDOT:PSS/PTAA/perovskite/C_{60}/ PEIE/ITO/flat band configuration gives PCE = 19.39%, V_{OC} = 1.1909 V, J_{SC} = 19.40 mA cm^{-2}, and FF = 80.79% under AM1.5G spectrum.

All the material and defects parameters are reported in Tables 3.7 and 3.8.

Table 3.7. PEDOT:PSS SCAPS parameters.

Parameters	PEDOT:PSS
Thickness (nm)	5
Bandgap (eV)	1.8
Electron affinity (eV)	3.4
Dielectric permittivity	18.00
CB effective density of states (cm^{-3})	2.2×10^{18}
VB effective density of states (cm^{-3})	1.8×10^{19}
Thermal velocity hole and electron	1.0×10^{7}
Electron mobility (cm^2/Vs)	4.5×10^{-2}
Hole mobility (cm^2/Vs)	4.5×10^{-2}
Donor density N_D (cm^{-3})	0
Acceptor density N_A (cm^{-3})	1.0×10^{20}
Defect density N_t (cm^{-3})	1.0×10^{15}
References	Alipour and Ghadimi (2021)

Table 2.8. PEDOT:PSS defects SCAPS parameters.

Parameters	Bulk PEDOT:PSS	PTAA/PEDOT:PSS interface
Defect type	Neutral	Neutral
Capture cross section (cm^2)	1.0×10^{-15}	1.0×10^{-16}
Energetic distribution	Single	Single
Reference energetic level	Above E_V	Above the highest E_V
Energy level (eV)	0.6	0.6
Defect density N_t (bulk cm^{-3}) (interface cm^{-2})	1.0×10^{15}	1.0×10^{11}
References	Alipour and Ghadimi (2021)	Assumed

3.6 Perovskite top cell

The top cell built is PEDOT:PSS/PTAA/perovskite/C_{60}/PEIE/ITO with perovskite *Eg* = 1.63 eV and thickness of 400 nm. This configuration with "flat band" contacts gives PCE = 19.39%, V_{OC} = 1.1909 V, J_{SC} = 19.40 mA cm^{-2}, and FF = 80.79%. Now, the perovskite *Eg* is changed in 1.68 eV and the thickness in 500 nm to be in accordance with D. Kim et al. (2020). The new configuration gives higher performance: PCE = 20.28%, V_{OC} = 1.201 V, J_{SC} = 20.258 mA cm^{-2}, and FF = 80.26%. Our configuration differs only in one layer (PEDOT:PSS) from the reference one (ITO/PTAA/perovskite/C_{60}/PEIE/ITO). It must be reminded that the reference performance is taken from the same reference paper but from the experimental results of ITO/PTAA/perovskite/C_{60}/BCP/Ag. In comparison with the experimental reference performance, the SCAPS cell is really close with little differences reported in Table 3.9. The highest difference is between the J_{SC}s. The SCAPS cell J_{SC} is 4.44% lower than the reference one.

A simplified image of the cell structure, two images of the band diagram, the J-V plot and the EQE-wavelength resulted from the SCAPS simulation, are reported in Fig. 3.8, 3.9, 3.10, 3.11 and 3.12. All the materials and defect parameters are reported in the Tables 3.10, 3.11 and 3.12.

Table 3.9 Performance comparison. Data reported are taken from D. Kim et al. (2020) and SCAPS simulator.

	PCE (%)	V_{OC} (V)	J_{SC} (mA/cm^2)	FF (%)
Reference cell: ITO/PTAA/perovskite/C_{60}/BCP/Ag	20.7	1.22	21.2	80.00
SCAPS cell: PEDOT:PSS/PTAA/perovskite/C_{60}/PEIE/ITO	20.28	1.201	20.258	80.26
SCAPS Data / Ref. Data - 1 (%)	-2.02	-1.56	-4.44	+0.33

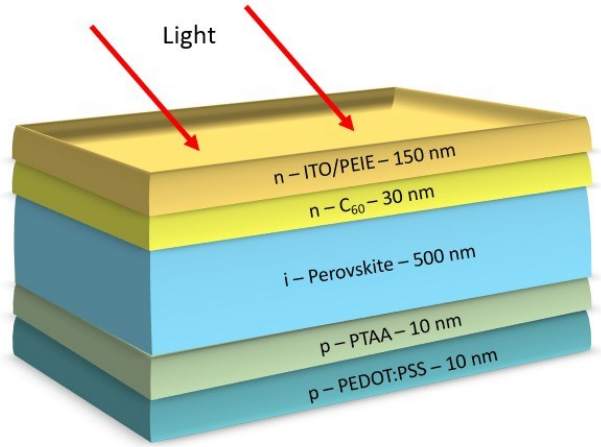

Figure 3.8 Perovskite top cell structure simplification.

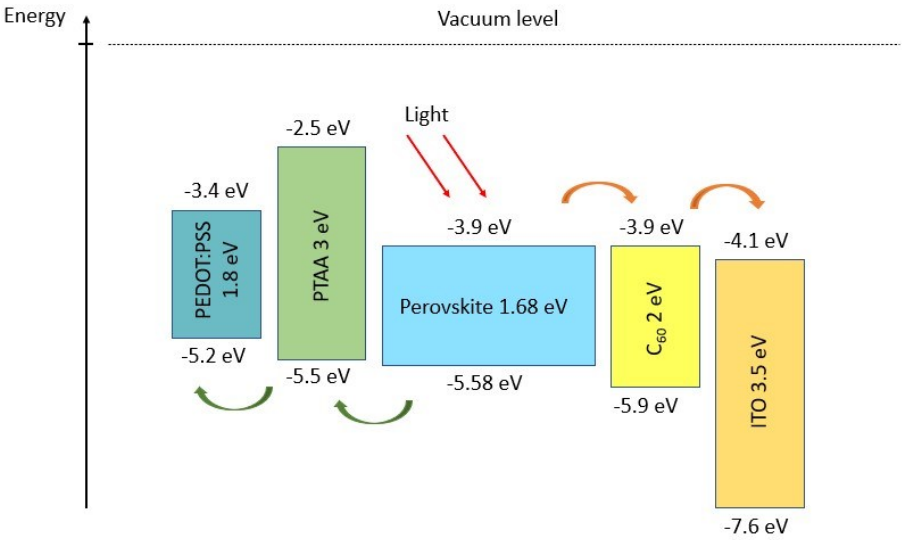

Figure 3.9 Perovskite top cell energy band diagram simplification.

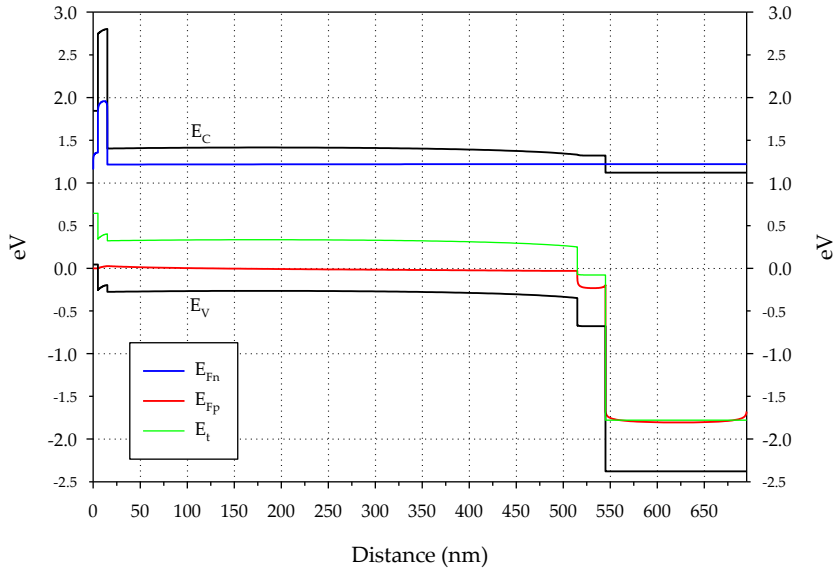

Figure 3.10 Perovskite top cell energy band diagram at 1.22 bias voltage. E_C is the conduction band, E_V is the valence band, E_{Fn} is the electron Fermi level, E_{Fp} is the hole Fermi level and E_t is the energy trap level. Data reported in figure are obtained from the SCAPS simulator.

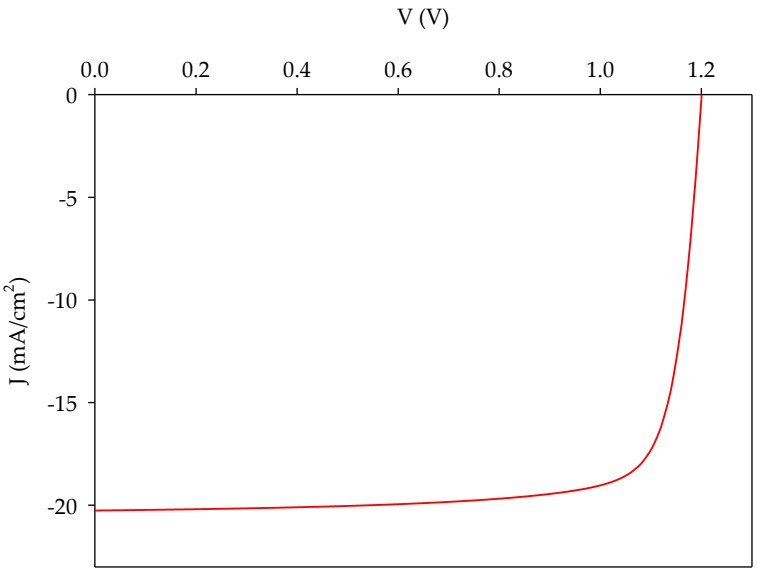

Figure 3.11. Current density J (mA/cm²) – Voltage V (V) plot of perovskite top cell. Data reported in figure are obtained from the SCAPS simulator.

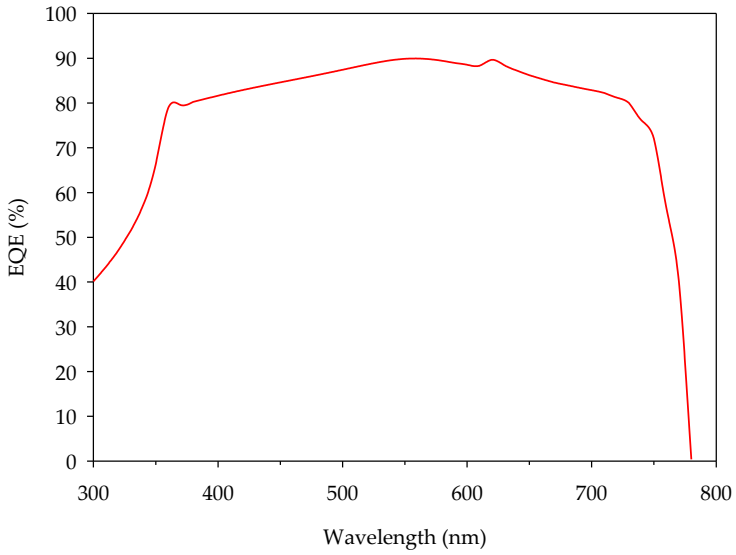

Figure 3.12. External Quantum Efficiency EQE (%) – Wavelength (nm) plot of perovskite top cell under AM1.5G spectrum. Data reported in figure are obtained from the SCAPS simulator.

Table 3.10. Perovskite top cell SCAPS parameters.

Parameters	PEDOT:PSS	PTAA	Perovskite	C_{60}	ITO
Thickness (nm)	5	10	500	30	150
Bandgap (eV)	1.8	3.00	1.68	2.00	3.50
Electron affinity (eV)	3.4	2.50	3.90	3.90	4.10
Dielectric permittivity	18.00	3.50	22.00	5.00	9.00
CB effective density of states (cm^{-3})	2.2×10^{18}	1.0×10^{20}	2.2×10^{18}	1.0×10^{20}	2.2×10^{18}
VB effective density of states (cm^{-3})	1.80×10^{19}	1.0×10^{20}	2.2×10^{18}	1.0×10^{20}	1.9×10^{19}
Thermal velocity hole and electron	1.0×10^{7}	1.0×10^{7}	1.0×10^{7}	1.0×10^{7}	1.0×10^{7}
Electron mobility (cm^2/Vs)	4.5×10^{-2}	1.5×10^{-4}	1.0	1.0×10^{-2}	1.0
Hole mobility (cm^2/Vs)	4.5×10^{-2}	1.5×10^{-4}	1.0	1.0×10^{-2}	1.0
Donor density N_D (cm^{-3})	0	0	1.0×10^{12}	2.0×10^{18}	1.0×10^{20}
Acceptor density N_A (cm^{-3})	1.0×10^{20}	2.0×10^{17}	1.0×10^{12}	0	0
Defect density N_t (cm^{-3})	1.0×10^{15}	1.0×10^{18}	2.0×10^{15}	1.0×10^{18}	1.0×10^{15}
References	Alipour and Ghadimi (2021)	Diekmann et al. (2021), Turedi et al. (2021)	D. Kim et al. (2020), Diekmann et al. (2021)	Diekmann et al. (2021), Turedi et al. (2021)	Bendib et al. (2020), Yu et al. (2016)

Table 3.11. Perovskite top cell bulk defects parameters

Parameters	Bulk PEDOT:PSS	Bulk PTAA	Bulk perovskite	Bulk C_{60}	Bulk ITO
Defect type	Neutral	Neutral	Neutral	Neutral	Neutral
Capture cross section (cm^2)	1.0×10^{-15}	1.0×10^{-16}	1.0×10^{-16}	1.0×10^{-16}	1.0×10^{-15}
Energetic distribution	Single	Single	Gaussian	Single	Single
Reference energetic level	Above E_V	Above E_V	Above E_V	Above E_V	Above E_V
Energy level (eV)	0.6	0.6	0.6	0.6	0.6
Characteristic energy (eV)	-	-	0.100	-	-
Defect density N_t (cm^{-3})	1.0×10^{15}	1.0×10^{18}	2.0×10^{15}	1.0×10^{18}	1.0×10^{15}
References	Alipour and Ghadimi (2021)	Turedi et al. (2021)	Turedi et al. (2021)	Turedi et al. (2021)	Bendib et al. (2020)

Table 3.12. Perovskite top cell interface defects parameters

Parameters	PTAA/PEDOT:PSS interface	PTAA/perovskite interface	C_{60}/perovskite interface	C_{60}/ITO interface
Defect type	Neutral	Neutral	Neutral	Neutral
Capture cross section (cm^2)	1.0×10^{-16}	1.0×10^{-16}	1.0×10^{-16}	1.0×10^{-16}
Energetic distribution	Single	Single	Single	Single
Reference energetic level	Above the highest E_V	Above the highest E_V	Above the highest E_V	Above the highest E_V
Energy level (eV)	0.6	0.6	0.6	0.6
Defect density N_t (cm^{-2})	1.0×10^{11}	1.0×10^{11}	2.0×10^{12}	2.0×10^{12}
References	Assumed	Turedi et al. (2021)	Turedi et al. (2021)	Assumed

3.7 Back contact

All the simulations were carried in "flat band" configuration for both front and rear or back contact. In this case, SCAPS calculates for every temperature the metal work function ϕ_m in such a way that flat-band conditions prevail (Burgelman M., Nollet, and Degrave 2000). A batch simulation of back contact/PEDOT:PSS/PTAA/perovskite/C_{60}/ PEIE/ITO/flat band demonstrates which back contacts are the best. The metal work function ϕ_m was varied from 4.6 eV to 5.1 eV to coincide with the energy band edges of the cell to allow charge carrier extraction. The surface recombination velocity for both electrons and holes was approximated as 1 x 10^7 cm/s. The good results, showed in Figure 3.13, prove that all the contacts with metal work function from 4.8 eV to 5.1 eV can be used, but the best are Au or Se contact with 5.1 eV and Be, Co or Ni with 5.0 eV (Nave 2017). The performance with ϕ_m = 5.0 or 5.1 eV are the same with PCE = 20.28%, V_{OC} = 1.006 V, J_{SC} = 20.257 mA cm^{-2}, and FF = 80.26% under AM1.5G spectrum. The cell without back contact has performance PCE = 20.28%, V_{OC} = 1.2006 V, J_{SC} = 20.258 mA cm^{-2}, and FF = 80.26%, so the performance remains unchanged. Using a 5.1 eV contact ensure to have a near ohmic behaviour that is preferable for the solar cells.

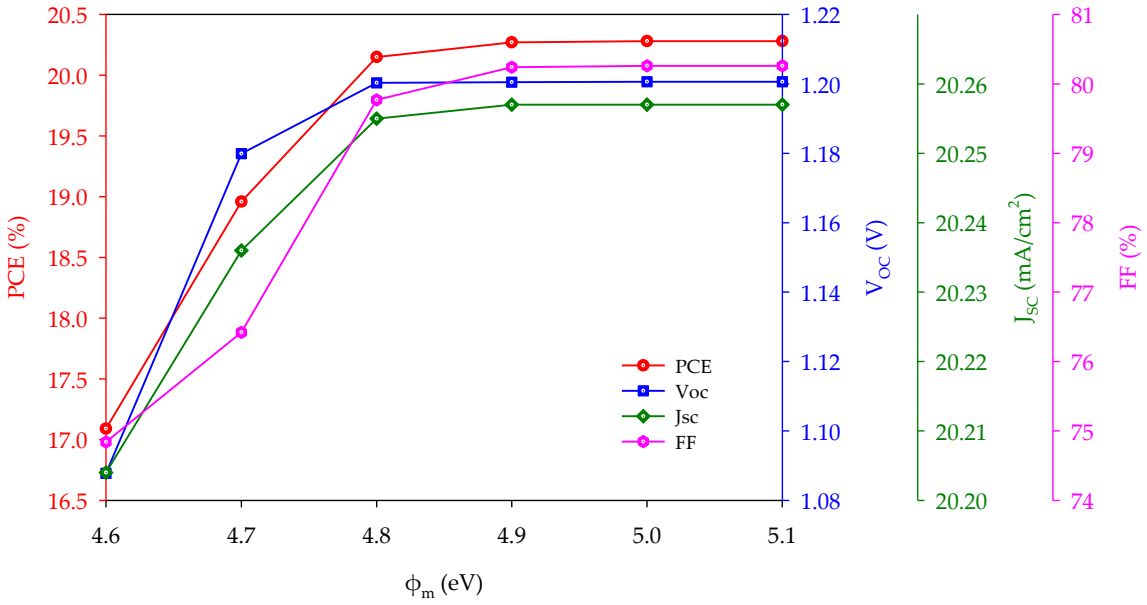

Figure 3.13. Batch simulation of back contact/PEDOT:PSS/PTAA/perovskite/C_{60}/PEIE/ITO/flat band under AM1.5G spectrum. Back contact ϕ_m varied from 4.6 to 5.1 eV. Data reported in figure are obtained from the SCAPS simulator.

3.8 Front contact

The front contact is studied in order to complete the cell. A batch simulation of Au/PEDOT:PSS/PTAA/perovskite/C_{60}/ PEIE/ITO/front contact demonstrates which front contacts are the best. The metal work function ϕ_m was varied from 4.0 eV to 4.7 eV to coincide with the energy band edges of the cell to allow carrier extraction. The surface recombination velocity for both electrons and holes was approximated as 1 x 10^7 cm/s. SCAPS is not able to simulate the cell with front contact ϕ_m = 4.7 eV. The good results, showed in Figure 3.14, prove that all the contacts with metal work function from 4.5 eV to 4.0 eV can be used and all of them give the same performance apart of 4.5 eV contact that gives slightly lower performance. Therefore, a large variety of contacts can be used: Cd (4.07 eV), Al (4.08 eV), Pb (4.14 eV), Ag (4.26 – 4.73 eV), Nb (4.3 eV), Zn (4.3 eV), Fe (4.5 eV), Hg (4.5 eV) (Nave 2017). Also adding the front contact the performance remains unchanged as before with only back contact or without contacts: PCE = 20.28%, V_{OC} = 1.2006 V, J_{SC} = 20.258 mA cm^{-2}, and FF = 80.26%.

The final configuration of the top cell could be Au/PEDOT:PSS/PTAA/perovskite/C_{60}/ PEIE/ITO/Ag with performance in line with the reference one, i.e., PCE = 20.7%, V_{OC} = 1.22 V, J_{SC} = 21.2 mA cm^{-2}, and FF = 80% of ITO/PTAA/perovskite/C_{60}/BCP/Ag under AM1.5G spectrum.

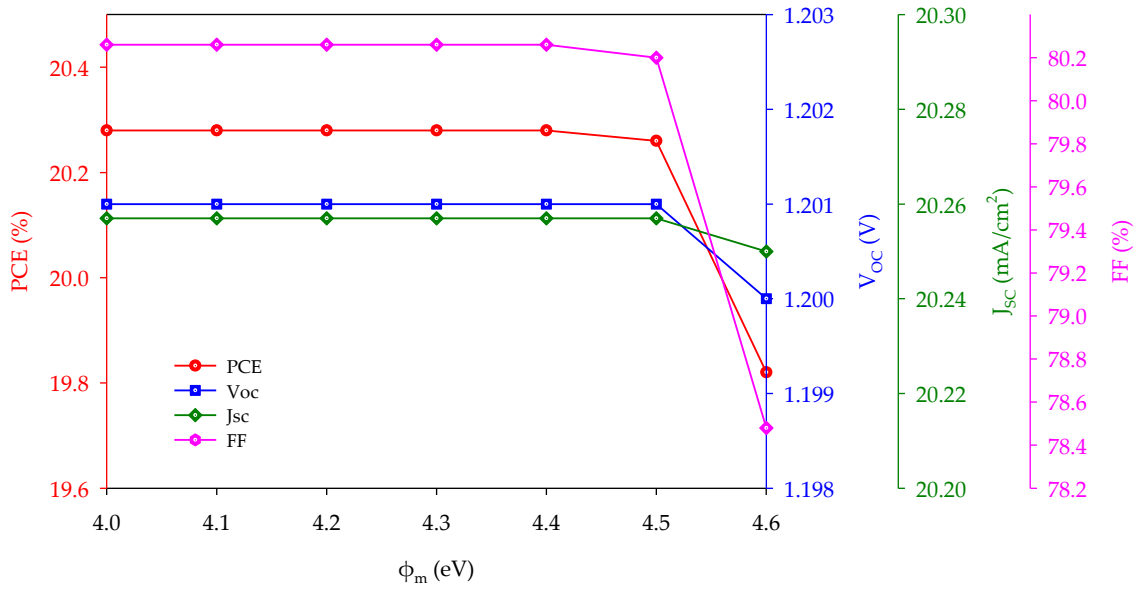

Figure 3.14. Batch simulation of Au/PEDOT:PSS/PTAA/perovskite/C_{60}/ PEIE/ITO/front contact under AM1.5G spectrum. Front contact ϕ_m varied from 4.0 to 4.7 eV. Data reported in figure are obtained from the SCAPS simulator.

3.9 Further studies

Further studies are conducted to visualize the most influential parameters that can increase and affect the performance. The cell studied is flat band/PEDOT:PSS/PTAA/ perovskite/C_{60}/PEIE/ITO/ flat band under AM1.5G (962.58 W m^{-2}) and AM1.5 1 sun (1000 W/m^2) spectra. It is chosen to use "flat band" contacts in order to have lesser noise factors because the contacts are the cell element that give more problems and performance reduction in SCAPS simulations.

In the first analysis the perovskite thickness is varied from 50 nm to 1000 nm under AM1.5 1 sun spectrum with perovskite energy gap fixed at 1.68 eV as the final SCAPS model was build. The PCE increases with the increasing thickness until reaches the maximum of 20.91% at 800 nm and then starts to decrease slowly (Fig. 3.15). The plot indicates saturation at around 650 nm. The PCE improvement with the thickness increase was expected as the light absorbed is proportional to $1 - e^{-\alpha x}$ where α is the absorption coefficient and x is the thickness, but when the thickness is too high the recombination become higher and contrast the absorption so a slightly decrease is displayed. The EQE-wavelength plot confirms the supposition about the absorption behaviour (Fig. 3.16). The V_{OC} increases as the thickness increases reaching the maximum of 1.209 V for high thickness of 1000 nm. The V_{OC} plot (Fig. 3.15) indicates saturation at 450 nm. The J_{SC} increases as the thickness increases reaching the maximum of 22.542 mA cm^{-2} for 1000 nm thickness (Fig. 3.15). The J_{SC} compared to the PCE and V_{OC} displayed less marked saturation. The FF increase until 200 nm with the maximum value of 82.30% and then decreases linearly because internal heat dissipation and resistance increase (Fig. 3.15).

The same analysis under AM1.5G spectrum shows very similar results (Fig. 3.17). If we take a look to the spectral irradiance-wavelength graph (Fig. 3.18) we can see that from the perovskite $Eg \approx 1.7$ eV ($\approx$ 730 nm) to higher energy, i.e., shorter wavelength, the sun irradiance is reduced by the effect of the atmosphere, so it was expected similar results. The J_{SC} decreases as the light has lower power density and is the most affected parameter by the changing the spectrum. The difference between the J_{SC} under different spectrum goes from 0.309 to 0.843 mA cm^{-2}. The FF remains the same and the V_{OC} decreases only by 0.001 V. The resulted PCE has a little decrease lower than 0.05%

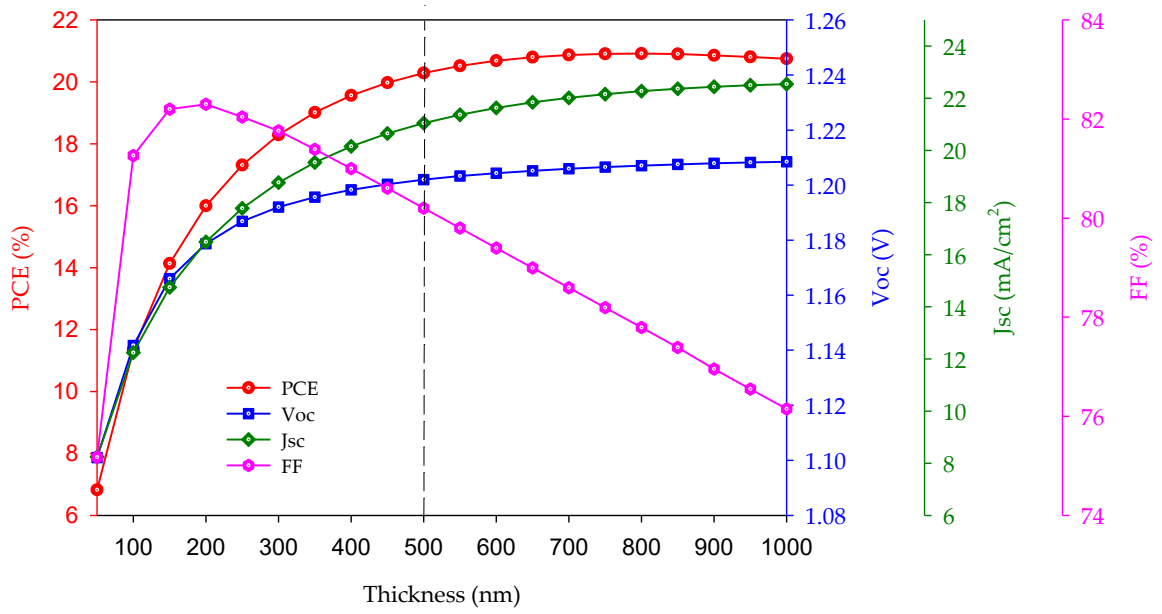

Figure 3.15. Batch simulation of flat band/PEDOT:PSS/PTAA/perovskite/C_{60}/PEIE/ITO/flat band varying perovskite thickness from 50 to 1000 nm under AM1.5G 1 sun. The dashed line is the reference perovskite thickness 500 nm. Data reported in figure are obtained from the SCAPS simulator.

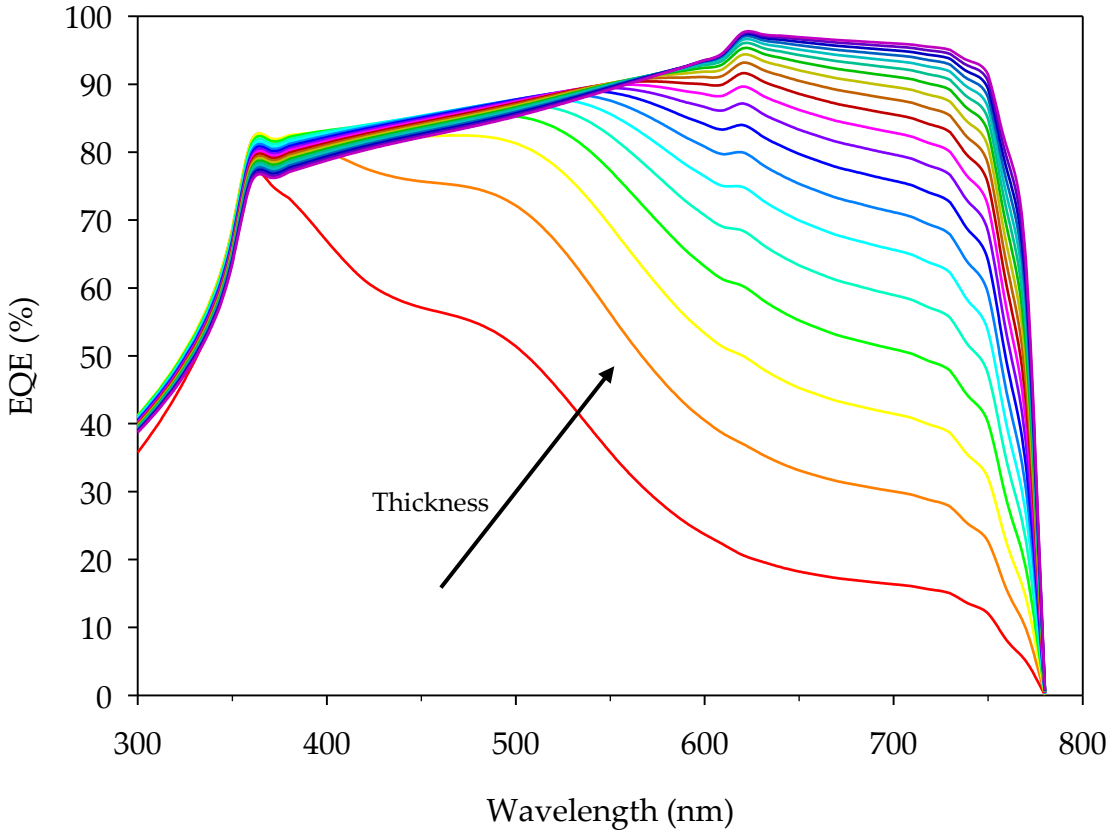

Figure 3.16. External Quantum Efficiency EQE (%) - wavelength (nm) plot varying the perovskite thickness from 50 to 1000 nm under AM1.5G 1 sun. Data reported in figure are obtained from the SCAPS simulator.

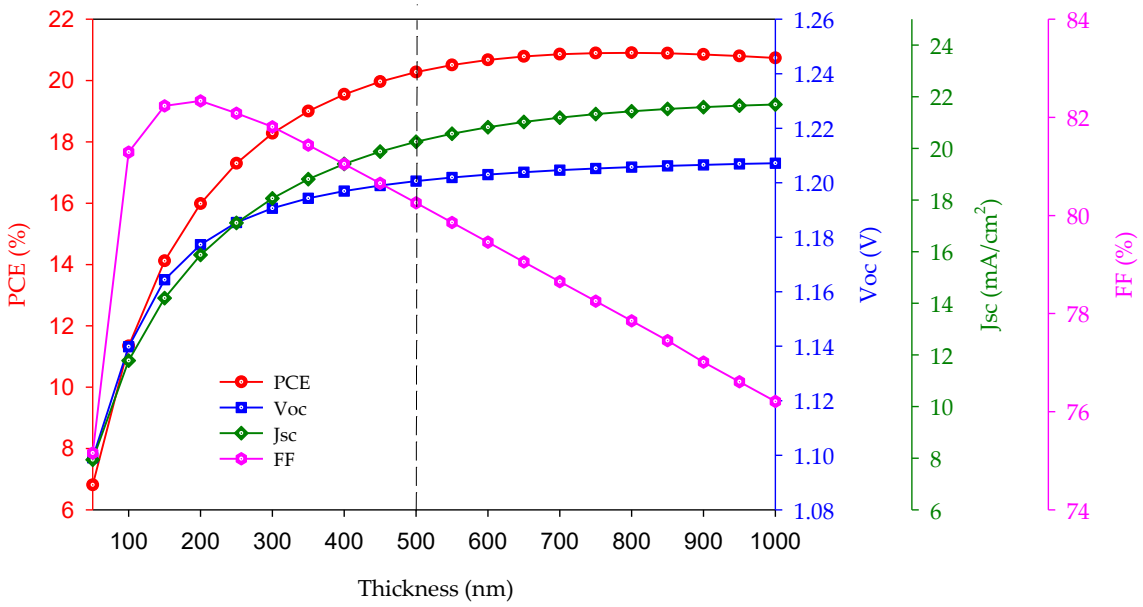

Figure 3.17. Batch simulation of flat band/PEDOT:PSS/PTAA/perovskite/C_{60}/PEIE/ITO/flat band varying perovskite thickness from 50 to 1000 nm under AM1.5G. The dashed line is the reference perovskite thickness 500 nm. Data reported in figure are obtained from the SCAPS simulator.

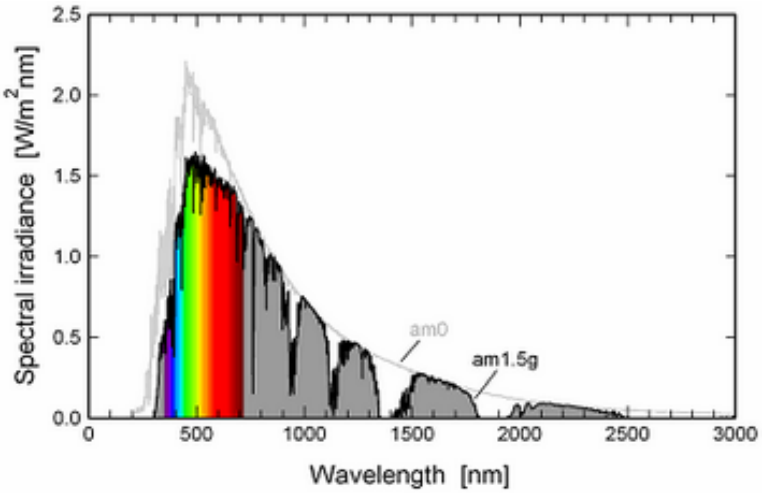

Figure 3.18. Spectral irradiance (W/m²nm) - Wavelength (nm) plot of AM1.5G and AM1.5 1 sun (or AM0). (Altermatt n.d.)

In the second analysis the perovskite *Eg* is varied from 1.6 eV to 1.8 eV to visualize other top cell options. The perovskite thickness is fixed at 500 nm as the final SCAPS model was build. The simulations under AM1.5 1 sun and AM1.5G (Fig. 3.19 and 3.20) demonstrate that if the light intensity decreases from decreases about 0.8 mA cm^{-2} and the FF increases about 0.05%, but in general the behaviour of the parameters remains the same under different spectrums. The PCE and 1000 W m^{-2} to 962.58 W m^{-2} the J_{SC} and V_{OC} are almost the same under different spectrum. The PCE increases with the *Eg*, it reaches the maximum of 20.34% (under AM1.5 1 sun) or 20.33% (under AM1.5G) in the 1.73 – 1.78 eV *Eg* range, at 1.79 eV starts to decrease, however the saturation behaviour appears at 1.7 eV. The PCE minimum is 19.89% (under AM1.5 1 sun) or 19.88% (under AM1.5G). These results mean that the *Eg* is not an affecting parameter for the performance. The V_{OC} increases slightly with the *Eg* and indicates saturation at around 1.67 eV. The V_{OC} maximum is about 1.20 V. The J_{SC} has almost a constant behaviour unless looking to the J_{SC}-*Eg* plots it could appear differently, but it decrease only from 21.044 mA cm^{-2} to 21.040 mA cm^{-2}. The FF is contstantly around 80% and has his maximum around 1.75 eV. The EQE does not change with the *Eg* (Fig. 3.21), this means that the carriers collection depends on the other layers of the cell and not only from the *Eg* of the absorber layer. If the EQE does not change in 775 – 690 nm wavelength range (1.6 – 1.8 eV energy gap range) the other layers recombine the carriers generated. The carriers recombine moving from the absorption layer to the contacts. Decreasing *Eg* the EQE should be wider.

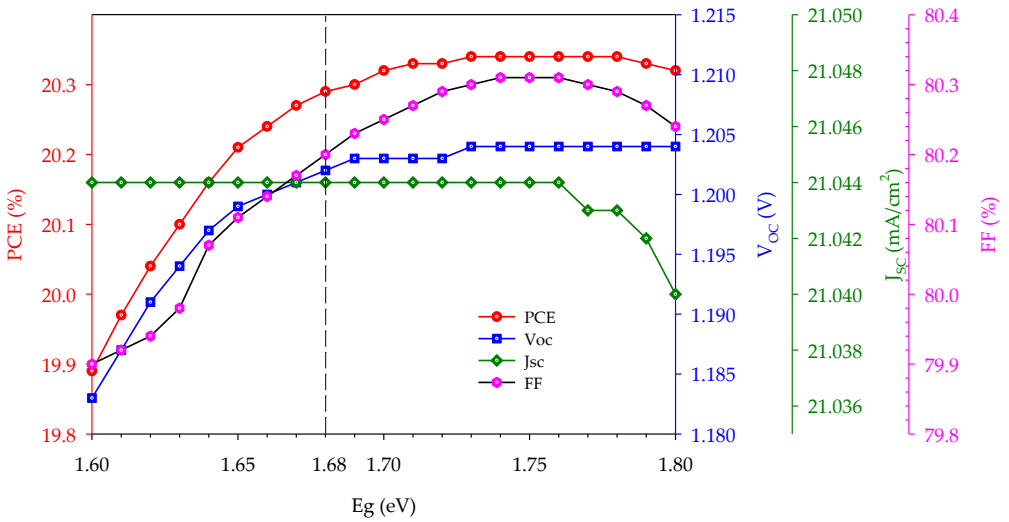

Figure 3.19. Batch simulation of flat band/PEDOT:PSS/PTAA/perovskite/C_{60}/PEIE/ITO/flat band varying perovskite energy gap Eg from 1.60 to 1.80 eV under AM1.5G 1 sun. The dashed line is the reference perovskite Eg = 1.68 eV Data reported in figure are obtained from the SCAPS simulator.

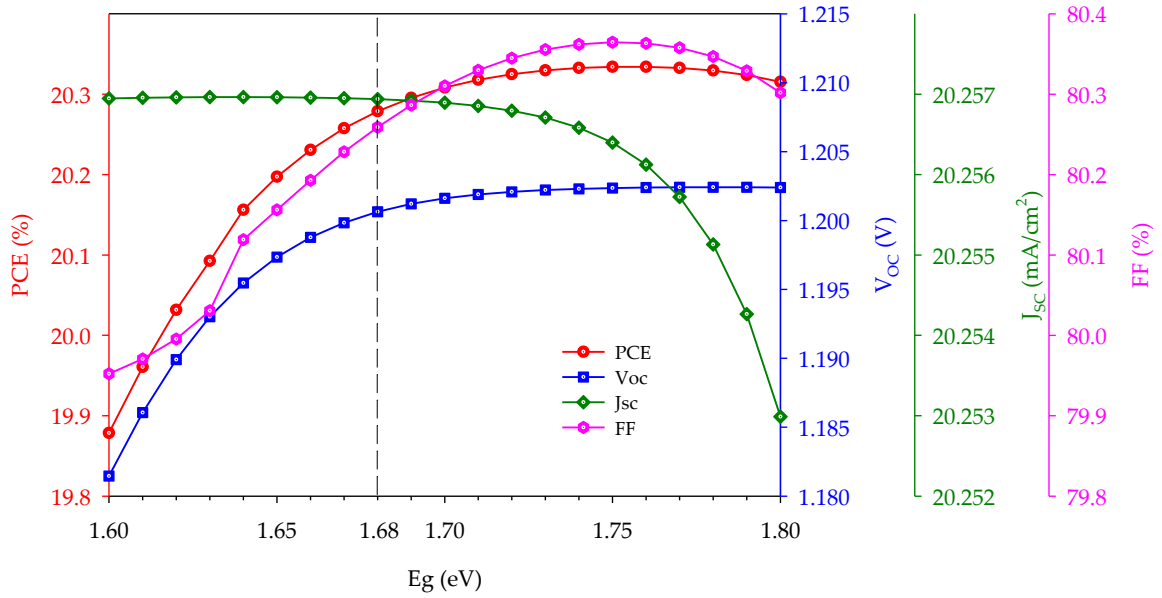

Figure 3.20. Batch simulation of flat band/PEDOT:PSS/PTAA/perovskite/C_{60}/PEIE/ITO/flat band varying perovskite energy gap Eg from 1.60 to 1.80 eV under AM1.5G. The dashed line is the reference perovskite Eg = 1.68 eV. Data reported in figure are obtained from the SCAPS simulator.

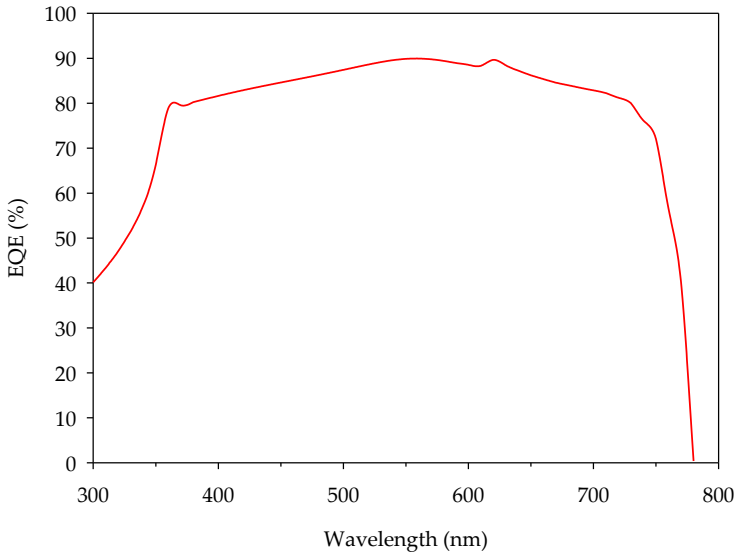

Figure 3.21. External Quantum Efficiency EQE (%) - Wavelength (nm) plot varying perovskite energy gap Eg. Data reported in figure are obtained from the SCAPS simulator.

In conclusion the SCAPS model with perovskite thickness of 500 nm and energy band gap of 1.68 eV is a valid model with good performance that can be done small improvements. The PCE can be increased by 3% and the J_{SC} by 7% increasing the perovskite thickness. The FF can be increased by 3% decreasing the perovskite thickness. The effect of varying perovskite *Eg* is slight and not relevant. The ETL and HTL must be developed for efficient collection of the charge carriers that is being generated in the device.

CHAPTER 4 - Si BOTTOM CELL

4.1 Reference Si Bottom cell

The materials used for the layers are reported by D. Kim et al. (2020b). The cell is a thick crystalline Si (c-Si) layer between two thin deposited layer of hydrogen-terminated amorphous Si (a-Si:H). The c-Si is reported to be *n*-type with a thickness of 300 μm and resistivity of 3.0 Ω cm, i.e., 1.5 x 10^{15} cm^{-3} donor concentration. The a-Si:H films are doped with hydrogen-diluted PH_3 and B_2H_6 gases giving the *n*- and *p*-type configurations respectively. The cell configuration is ITO/*n*-a-Si:H/*n*-c-Si/*p*-a-Si:H/ITO/Ag with performance: PCE = 17.28%, V_{OC} = 0.644 V, J_{SC} = 35.11 mA cm^{-2}, and FF = 76% under AM1.5G 1 sun spectrum (1000 W m^{-2}) and PCE = 9.39%, V_{OC} = 0.624 V, J_{SC} = 19.32 mA cm^{-2}, and FF 78% under filtered light of a structure that consist in glass/PTAA/perovskite/C_{60}/PEIE/ ITO.

4.2 Initial study

The light in the bottom Si cell first must pass through the *n*-layers and then to the *p*-layers as in the top cell because the cells must be connected in series to build a tandem cell. The cell is studied and modelled first under AM1.5G 1 sun spectrum and then under the filtered spectrum which is the sun spectrum after passing through the perovskite top cell.

The material parameters of the a-Si:H are taken from Schropp and Zeman (1998). The thickness of 10 nm for both *n*- and *p*-a-Si:H is taken arbitrarily for a first attempt and then studied further. The absorption file used for both the amorphous Si layer is taken from Adachi (1999) and Archer and Hill (2001). The parameters of c-Si are chosen arbitrarily. The thickness and the doping concentration are taken as reported by D. Kim et al. (2020b). The electron affinity for the crystalline Si is well known to be 4.05 eV (Hussain et al. 2019). The absorption file used for the absorber layer *n*-c-Si is taken from Green (1995). The interface defects are supposed to be neutral with capture cross sections of 1 x 10^{-18} cm^2 and total density of 1 x 10^{12} cm^{-2}. The parameters used are reported in Tables 4.1, 4.2 and 4.3. The cell flat band/*n*-a-Si:H/*n*-c-Si/*p*-a-Si:H/flat band is simulated under AM1.5G 1 sun. The performance is: PCE = 2.70%, V_{OC} = 0.542 V, J_{SC} = 6.280 mA cm^{-2}, and FF = 79.45%, it is very far from the reference one (Table 4.4). Improvements must be done.

Table 4.1. Si bottom cell SCAPS parameters for the Initial study.

Parameters	*n*-a-Si:H	*n*-c-Si	*p*-a-Si:H
Thickness (μm)	0.01	300	0.01
Bandgap (eV)	1.80	1.12	1.80
Electron affinity (eV)	3.90	4.05	3.90
Dielectric permittivity	11.90	11.90	11.90
CB effective density of states (cm^{-3})	1.0 x 10^{20}	2.8 x 10^{19}	1.0 x 10^{20}
VB effective density of states (cm^{-3})	1.0 x 10^{20}	1.4 x 10^{19}	1.0 x 10^{20}
Thermal velocity hole and electron	1.0 x 10^{7}	1.0 x 10^{7}	1.0 x 10^{7}
Electron mobility (cm^2/Vs)	2.0 x 10^{1}	1.4 x 10^{3}	2.0 x 10^{1}
Hole mobility (cm^2/Vs)	5.0	4.5 x 10^{2}	5.0

Parameters	*n*-a-Si:H	*n*-c-Si	*p*-a-Si:H
Donor density N_D (cm^{-3})	1.0×10^{17}	1.5×10^{15}	1.0×10^{7}
Acceptor density N_A (cm^{-3})	1.0×10^{7}	0	1.0×10^{17}
Defect density N_t (cm^{-3})	-	1.0×10^{12}	-
References	Schropp and Zeman (1998)	D. Kim et al. (2020b), Hussain et al. (2019), Arbitrarily chosen	Schropp and Zeman (1998)

Table 4.2. Si bottom cell bulk defects SCAPS parameters for the Initial study.

Parameters	Bulk *n*-a-Si:H (1)	Bulk *n*-a-Si:H (2)	Bulk *n*-a-Si:H (3)	Bulk *n*-c-Si	Bulk *p*-a-Si:H (1)	Bulk *p*-a-Si:H (2)	Bulk *p*-a-Si:H (3)
Defect type	Amphoteric	Donor	Acceptor	Neutral	Amphote-ric	Donor	Acceptor
Capture cross section (cm^2)	-	1.0×10^{-16}	1.0×10^{-16}	1.0×10^{-14}	-	1.0×10^{-16}	1.0×10^{-16}
Energetic distribution	Gaussian	Single	Single	Single	Gaussian	Single	Single
Reference energetic level	Below E_C	Above E_V	Above E_V	Above E_V	Below E_C	Above E_V	Above E_V
Energy level (eV)	0.7/0.5	0.6	0.6	0.6	0.7/0.5	0.6	0.6
Characteristic energy (eV)	0.288	-	-	-	0.288	-	-
Defect density N_t (cm^{-3})	8.0×10^{16}	1.0×10^{16}	1.0×10^{16}	1.0×10^{12}	8.0×10^{14}	1.0×10^{16}	1.0×10^{16}
References	Schropp and Zeman (1998)	Schropp and Zeman (1998)	Schropp and Zeman (1998)	Arbitra-rily chosen	Schropp and Zeman (1998)	Schropp and Zeman (1998)	Schropp and Zeman (1998)

Table 4.3. Si bottom cell interface defects SCAPS parameters for the Initial study.

Parameters	*n*-a-Si:H/*n*-c-Si interface	*n*-c-Si/*p*-a-Si:H interface
Defect type	Neutral	Neutral
Capture cross section (cm^2)	1.0×10^{-18}	1.0×10^{-18}
Energetic distribution	Single	Single
Reference energetic level	Above the highest E_V	Above the highest E_V
Energy level (eV)	0.6	0.6
Defect density N_t (cm^{-2})	1.0×10^{12}	1.0×10^{12}
References	Assumed	Assumed

Table 4.4. Performance comparison. Data reported are taken from D. Kim et al. (2020b) and SCAPS simulator.

	PCE (%)	V_{OC} (V)	J_{SC} (mA/cm^2)	FF (%)
Reference cell: ITO/*n*-a-Si:H/*n*-c-Si/*p*-a-Si:H/ITO/Ag	17.28	0.644	35.110	76.00
Initial study: flat band/*n*-a-Si:H/*n*-c-Si/*p*-a-Si:H/flat band	2.70	0.542	6.280	79.45
Initial study Data / Ref. Data - 1 (%)	-84.38	-15.84	-82.11	+4.54

4.3 Device optimization

4.3.1 Improvement by reducing c-Si bulk defect density

The first improvement was done by studying the bulk defect of the c-Si absorber layer. The bulk defect is neutral with capture cross section of holes and electrons of 10^{-14} cm^2; the energy distribution is single and the energy is 0.6 eV above the valence band. A batch simulation varying the defect density N_t from 1 x 10^{10} to 1 x 10^{16} cm^{-3} (Fig. 4.1) demonstrates the heavy effect that the bulk defect density has in the cell performance. Decreasing the defect density, the PCE, J_{SC} and V_{OC} increase considerably closer to the reference performance. The defect density of 1 x 10^{11} cm^{-3} was selected and the related performance is: PCE = 13.66%, V_{OC} = 0.644 V, J_{SC} = 30.611 mA cm^{-2}, and FF = 69.26% (Table 4.5). The V_{OC} of the reference paper and the SCAPS model are the same, i.e., 0.644 V. The J_{SC} and FF must be subjected to further improvements.

It was chosen to decrease the defect density but decreasing the capture cross sections gives the same result as they are related by $\tau_n = \frac{1}{\sigma_n N_t v_{thn}}$ where τ_n is the electron lifetime, σ_n is the electron capture cross section, N_t is the defect density, and v_{thn} is the electron thermal velocity (Burgelman M., Nollet, and Degrave 2000). For the holes lifetime τ_p is the same formula with respective σ_p and v_{thp} values.

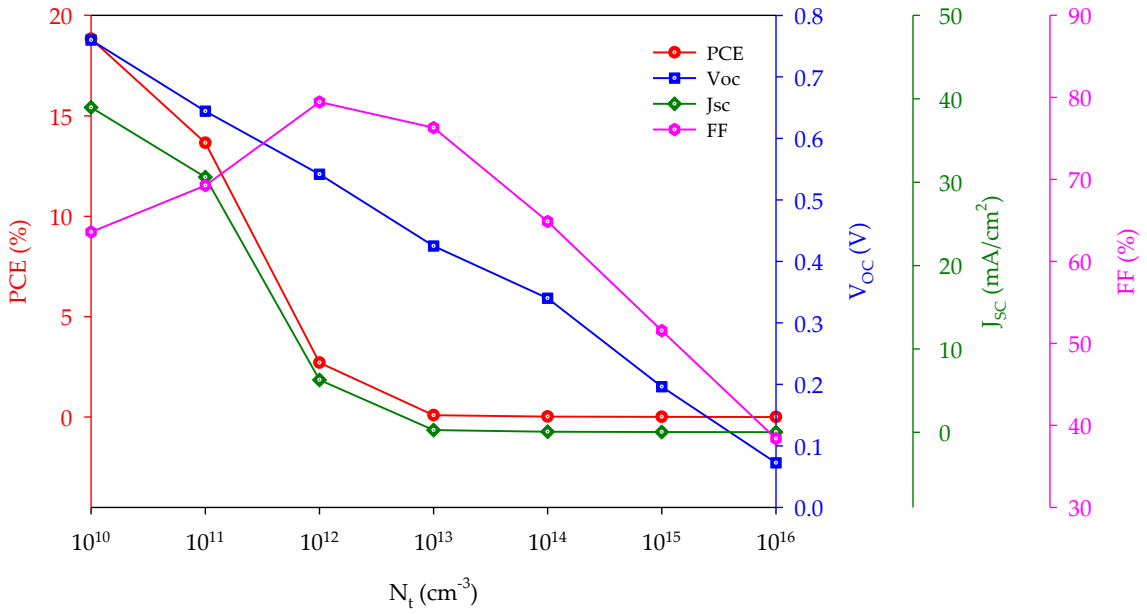

Figure 4.1. Batch simulation of flat band/a-Si:H/c-Si/a-Si:H/flat band varying the bulk defect density N_t of c-Si from 1 x 10^{10} to 1 x 10^{16} cm^{-3} under AM1.5G 1 sun spectrum. Data reported in figure are obtained from the SCAPS simulator.

Table 4.5. Performance comparison. Data reported are taken from D. Kim et al. (2020b) and SCAPS simulator.

	PCE (%)	V_{OC} (V)	J_{SC} (mA/cm²)	FF (%)
Reference cell: ITO/*n*-a-Si:H/*n*-c-Si/*p*-a-Si:H/ITO/Ag	17.28	0.644	35.110	76.00
(1) Initial study: flat band/*n*-a-Si:H/*n*-c-Si/*p*-a-Si:H/flat band	2.70	0.542	6.280	79.45
(2) Reduced c-Si bulk defect density	13.66	0.644	30.611	69.26
Second study Data (2) / Ref. Data - 1 (%)	-20.95	0	-12.81	-8.87

4.3.2 Improvement by reducing c-Si thickness

As the J_{SC} is related with the intensity of the light and its absorption by the cell, the thickness of the absorber c-Si layer is studied. A batch simulation varying the thickness from 200 to 400 µm was run (Fig. 4.2). Decreasing the thickness, the PCE and J_{SC} increase, the FF decreases, and the V_{OC} has a slight increment. The performance increases as the thickness is reduced because the recombination is lowered as the carriers have to move for smaller distance to arrive to their respective transport layer. Two thicknesses can be selected for a further study: 250 µm and 200 µm. The performance with c-Si thickness of

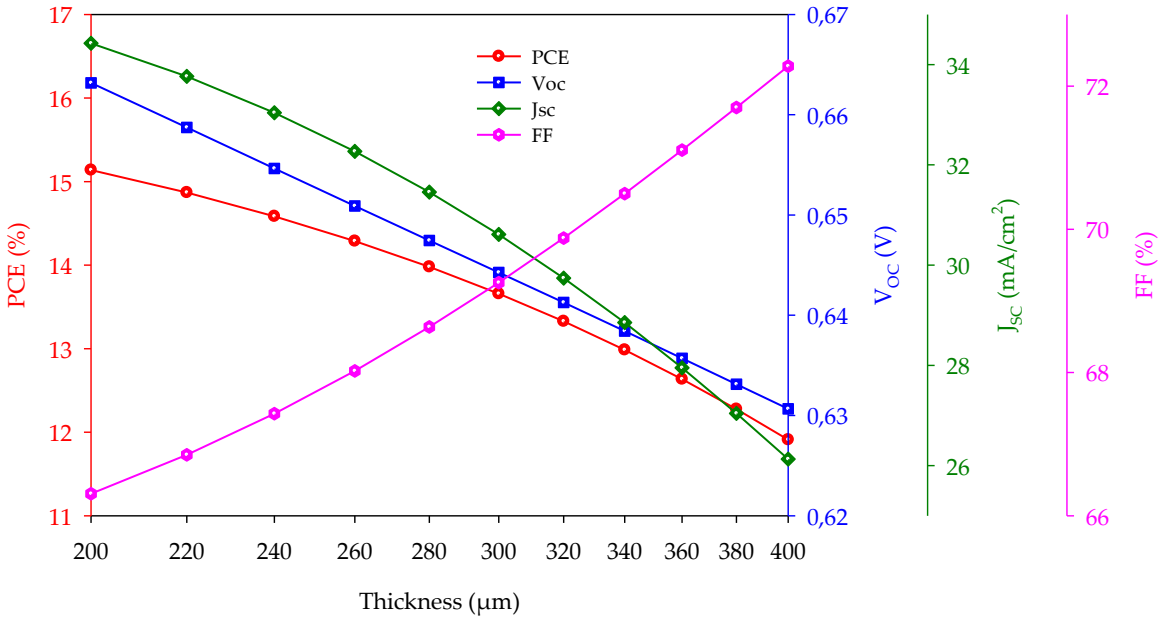

Figure 4.2. Batch simulation of flat band/a-Si:H/c-Si/a-Si:H/flat band varying the c-Si thickness from 200 to 400 µm under AM1.5G 1 sun spectrum. Data reported in figure are obtained from the SCAPS simulator.

250 μm is: PCE = 14.44%, V_{OC} = 0.653 V, J_{SC} = 32.660 mA cm^{-2}, and FF = 67.72%. The performance with c-Si thickness of 200 μm is: PCE = 15.14%, V_{OC} = 0.663 V, J_{SC} = 34.427 mA cm^{-2}, and FF = 66.31% (Table 4.6). Both models are approaching the reference J_{SC} of 35.11 mA cm^{-2} increasing also the PCE, the V_{OC} has a slight increment but is still close to the reference one, the FF still must be improved.

Table 4.6. Performance comparison. Data reported from D. Kim et al. (2020b) and SCAPS simulator.

	PCE (%)	V_{OC} (V)	J_{SC} (mA/cm²)	FF (%)
Reference cell: ITO/*n*-a-Si:H/*n*-c-Si/*p*-a-Si:H/ITO/Ag	17.28	0.644	35.110	76.00
(1) Initial study: flat band/*n*-a-Si:H/*n*-c-Si/*p*-a-Si:H/flat band	2.70	0.542	6.280	79.45
(2) Reduced c-Si bulk defect density	13.66	0.644	30.611	69.26
(3.1) Reduced c-Si thickness to 250 μm	14.44	0.653	32.660	67.72
Third study Data (3.1) / Ref. Data - 1 (%)	-16.43	+1.40	-6.98	-10.89
(3.2) Reduced c-Si thickness to 200 μm	15.14	0.663	34.427	66.31
Third study Data (3.2) / Ref. Data - 1 (%)	-12.38	+2.95	-1.95	-12.75

4.3.3 Improvement by reducing *n*-a-Si:H thickness

As D. Kim et al. (2020) did not specify the thickness of the a-Si:H layers, they can be studied and the most appropriate thickness that fits with the reference performance can be used. A batch simulation was run with the c-Si thickness of 300 μm to see the behaviour of the cell performance. The thickness of *n*-a-Si:H was varied from 15 nm to 5 nm. The results show the small effect of the *n*-a-Si:H thickness on the performance (Fig. 4.3). The PCE and J_{SC} have a slight increment decreasing the thickness. The V_{OC} and FF are not affected. However, as the J_{SC} increases and consequently the PCE increases, it was decided to use a thickness of 5 nm.

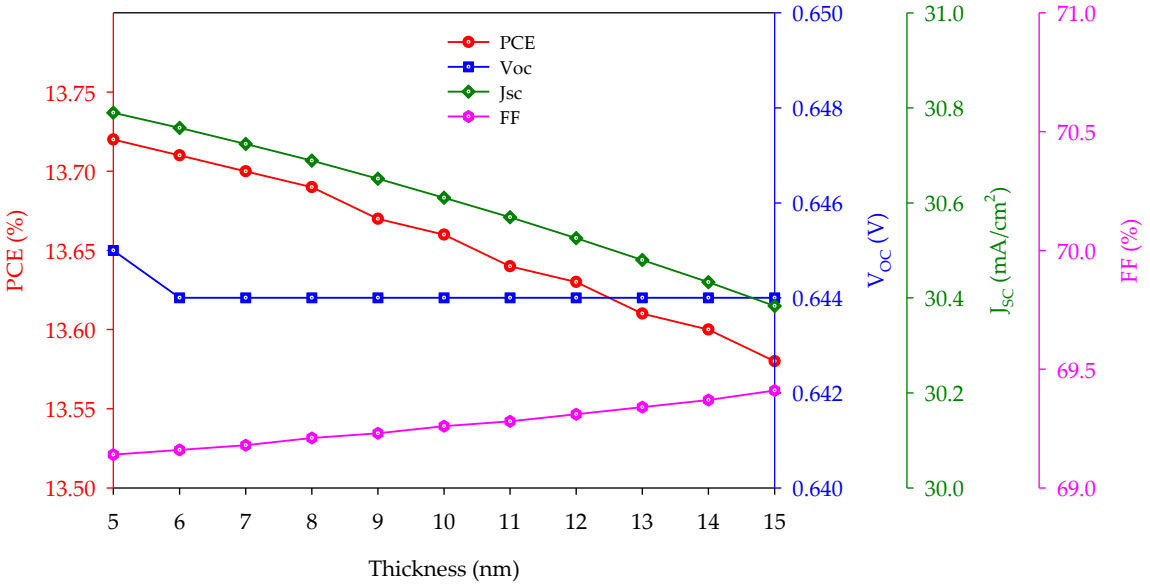

Figure 4.3. Batch simulation of flat band/n-a-Si:H/n-c-Si/p-a-Si:H/flat band varying the n-a-Si:H thickness from 5 to 15 nm under filtered spectrum with c-Si thickness of 300 µm. Data reported in figure are obtained from the SCAPS simulator.

4.3.4 Improvement by reducing *p*-a-Si:H thickness

Two batch simulations were run, one with the c-Si thickness of 200 µm and the other with the c-Si thickness of 250 µm. The thickness is varied from 15 nm to 5 nm (Fig. 4.4 and 4.5). Both the simulations show that the J_{SC} and V_{OC} are not affected but the FF has a considerable increment decreasing the thickness, resulting in PCE improvement as well. For the c-Si thickness of 250 µm a *p*-a-Si:H thickness of 5 nm is selected giving performance PCE = 16.92%, V_{OC} = 0.653 V, J_{SC} = 32.855 mA cm^{-2}, and FF = 78.85%. The performance difference from the reference one accounts mostly for the J_{SC} difference that is 2.225 mA cm^{-2} lower. The FF is 3.75% higher (Table 4.7). For the c-Si thickness of 200 µm a *p*-a-Si:H thickness of 7 nm is selected giving performance PCE = 17.45%, V_{OC} = 0.663 V, J_{SC} = 34.630 mA cm^{-2}, and FF = 75.94%. The performance is almost the same of the reference one with only a slight difference in V_{OC} and J_{SC} (Table 4.7).

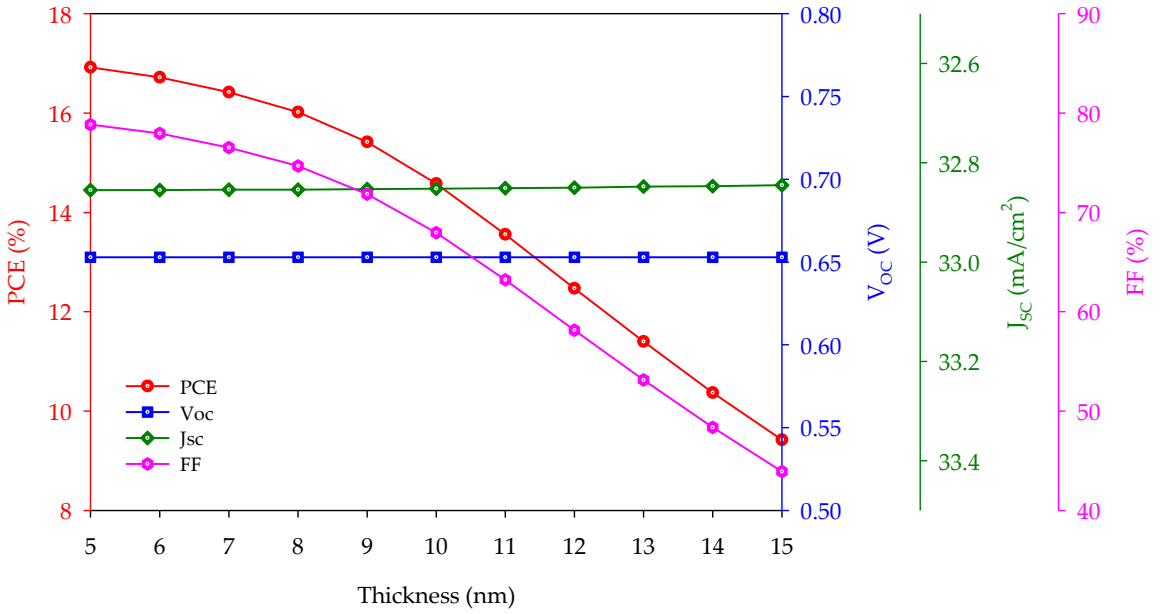

Figure 4.4. Batch simulation of flat band/n-a-Si:H/n-c-Si/p-a-Si:H/flat band varying the p-a-Si:H thickness from 5 to 15 nm under AM1.5G 1 sun spectrum with c-Si thickness of 250 µm. Data reported in figure are obtained from the SCAPS simulator.

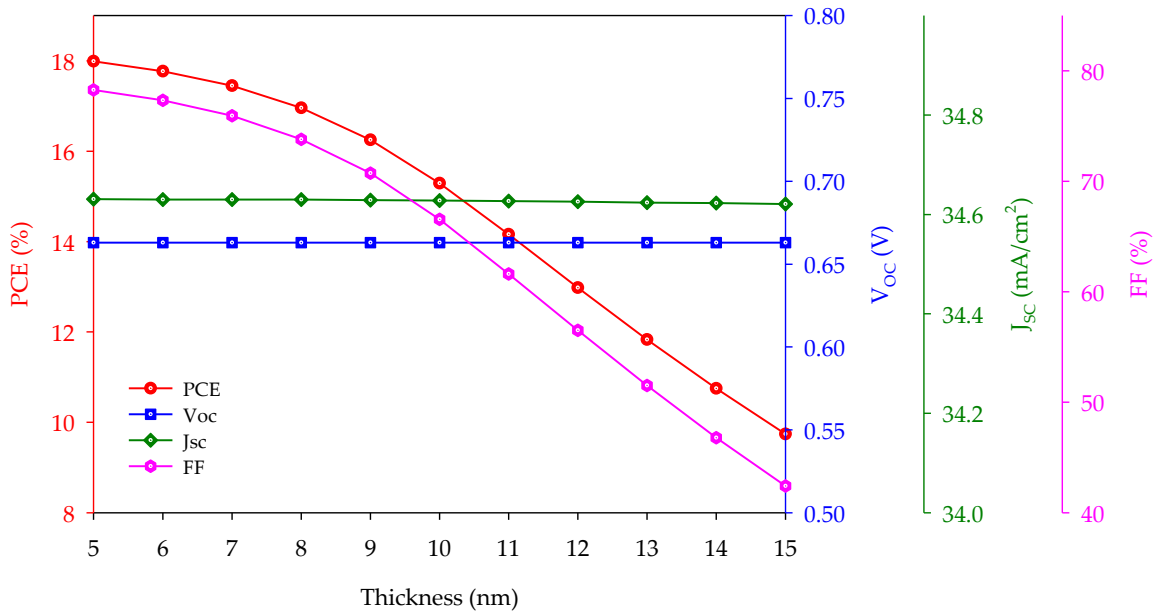

Figure 4.5. Batch simulation of flat band/n-a-Si:H/n-c-Si/p-a-Si:H/flat band varying the p-a-Si:H thickness from 5 to 15 nm under AM1.5G 1 sun with c-Si thickness of 200 µm. Data reported in figure are obtained from the SCAPS simulator.

Table 4.7. Performance comparison. Data reported are taken from D. Kim et al. (2020b) and SCAPS simulator.

	PCE (%)	V_{OC} (V)	J_{SC} (mA/cm²)	FF (%)
Reference cell: ITO/*n*-a-Si:H/*n*-c-Si/*p*-a-Si:H/ITO/Ag	17.28	0.644	35.110	76.00
(1) Initial study: flat band/*n*-a-Si:H/*n*-c-Si/*p*-a-Si:H/flat band	2.70	0.542	6.280	79.45
(2) Reduced c-Si bulk defect density	13.66	0.644	30.611	69.26
(3.1) Reduced c-Si thickness to 250 μm	14.44	0.653	32.660	67.72
(3.2) Reduced c-Si thickness to 200 μm	15.14	0.663	34.427	66.31
(4.1) Reduced *p*-a-Si:H thickness (250 μm c-Si thickness)	16.92	0.653	32.885	78.85
Fourth study Data (4.1) / Ref. Data - 1 (%)	-2.08	+1.40	-6.34	+3.75
(4.2) Reduced *p*-a-Si:H thickness (200 μm c-Si thickness)	17.45	0.663	34.630	75.94
Fourth study Data (4.2) / Ref. Data - 1 (%)	+0.98	+2.95	-1.37	-0.08

4.4 Si bottom cells

Two bottom Si cell valid models were built with different c-Si absorbance layer thickness. The information gave by Kim et al. about the c-Si thickness was neglected to get closer to the reference performance. The configuration is *n*-a-Si:H/*n*-c-Si/*p*-a-Si:H and the band diagram of the cells are shown in Figure 4.6, 4.7 and 4.8. The model with 200 μm of c-Si thickness has performance closer to the reference one than the model with 250 μm thickness. The performances are reported in Table 4.7 in Section 4.3.4. The J-V and EQE plot resulted from the SCAPS simulations under AM1.5G 1 sun spectrum are reported in Figures 4.9 and 4.10. From this study, it can be concluded that for a Si cell with *n*/*n*/*p* configuration, decreasing the thickness and the bulk defect density of the absorber layer, the J_{SC} increases (Fig. 4.11), decreasing the thickness of the *p*-layer the FF increases (Fig. 4.12), and varying the *n*-layer thickness has not a big impact on the performance at all. The SCAPS parameters are reported in the Tables 4.8, 4.9 and 4.10. The models are not subjected to further improvements and modification as it is not the main goal of the work. The cells should be completed adding the transparent conductive oxide (TCO) and the contacts. These models are a guideline to create a tandem cell.

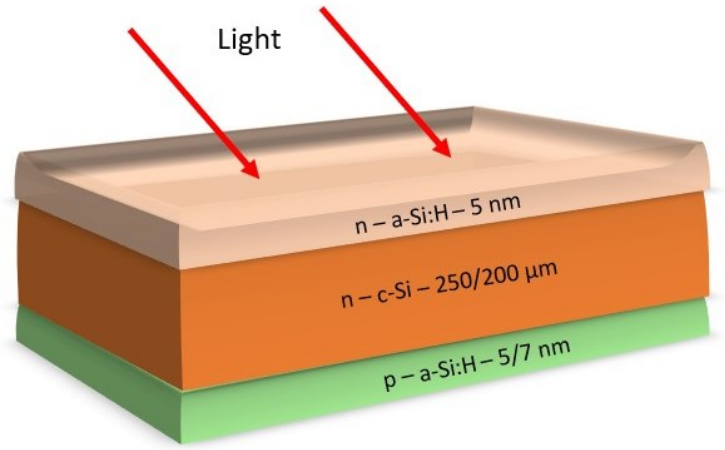

Figure 4.6. Si bottom cell structure simplification.

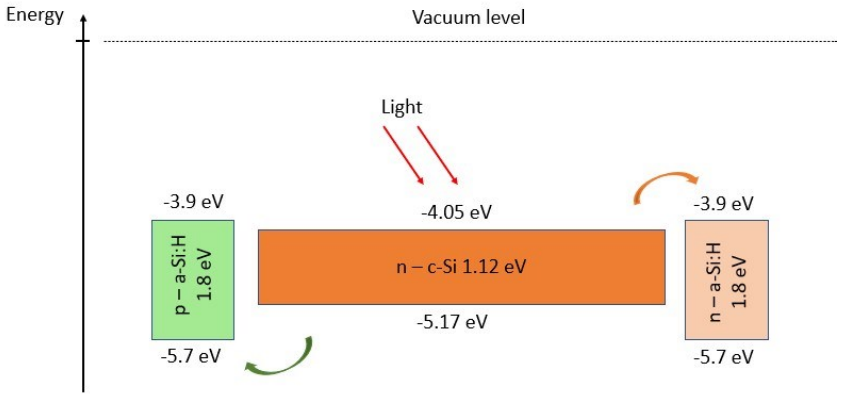

Figure 4.7. Si bottom cell energy band diagram simplification.

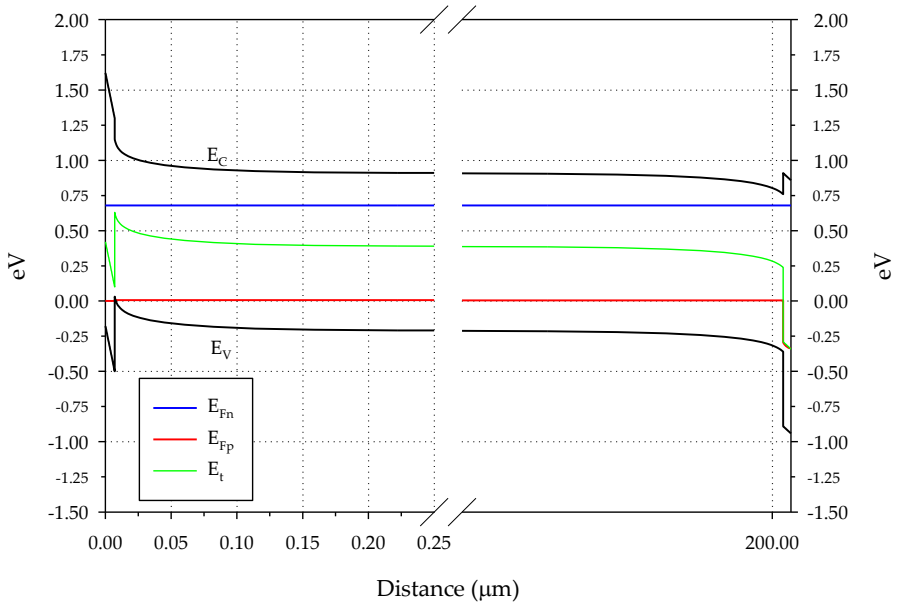

Figure 4.8 Si bottom cell energy band diagram at 0.68 bias voltage. E_C is the conduction band, E_V is the valence band, E_{Fn} is the electron Fermi level, E_{Fp} is the hole Fermi level and E_t is the energy trap level. Data reported in figure are obtained from the SCAPS simulator.

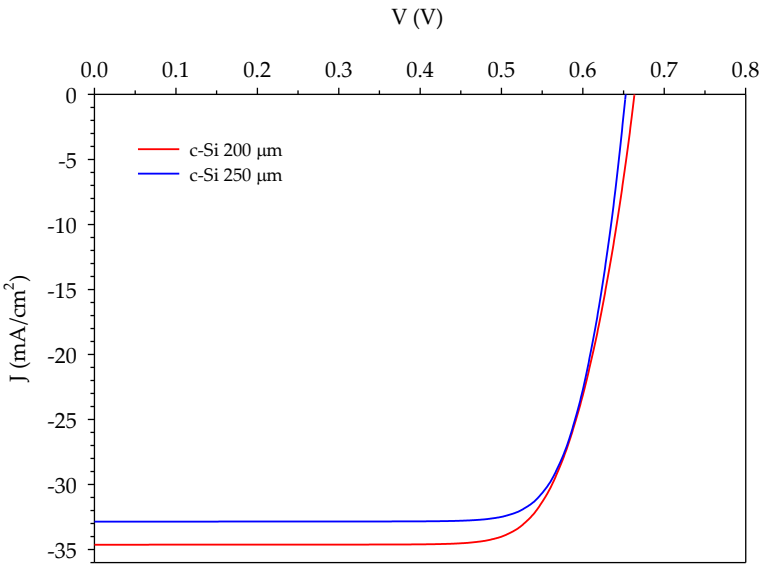

Figure 4.9. Current density J (mA/cm²) – Voltage V (V) plot of Si bottom cells under AM1.5G 1 sun spectrum. Data reported in figure are obtained from the SCAPS simulator.

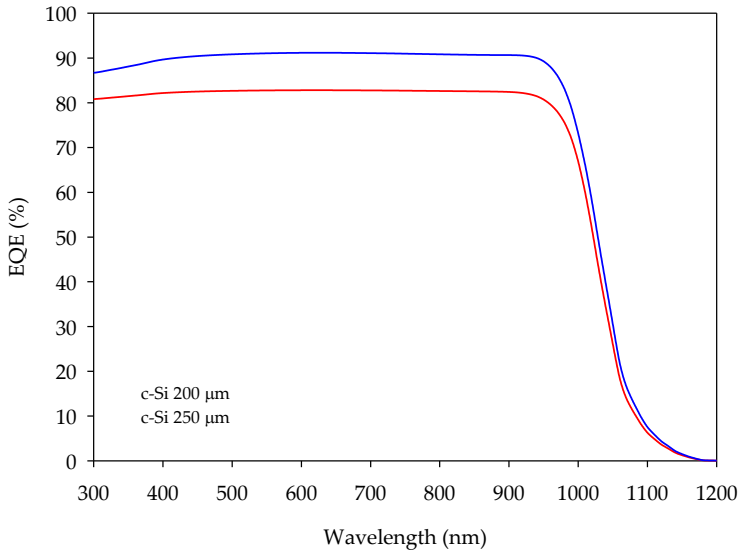

Figure 4.10. External Quantum Efficiency EQE (%) – Wavelength (nm) plot of Si bottom cells under AM1.5G 1 sun spectrum. Data reported in figure are obtained from the SCAPS simulator.

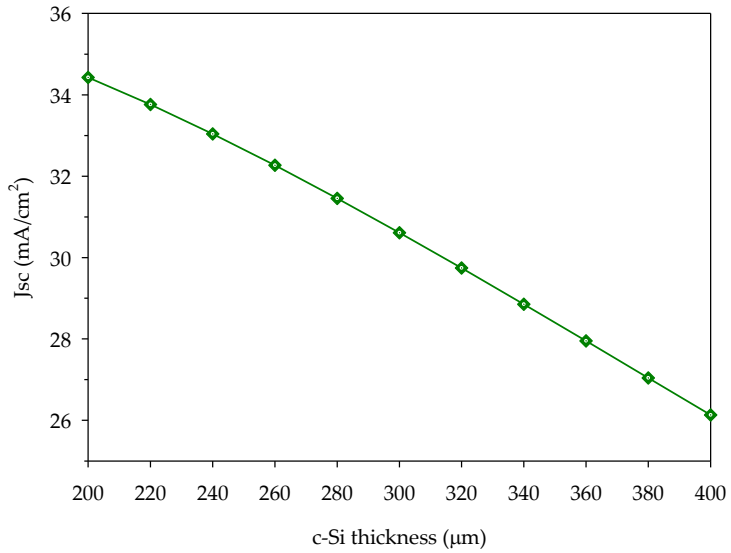

Figure 4.11. J_{SC} dependence from the absorber c-Si thickness. Data reported in figure are obtained from the SCAPS simulator.

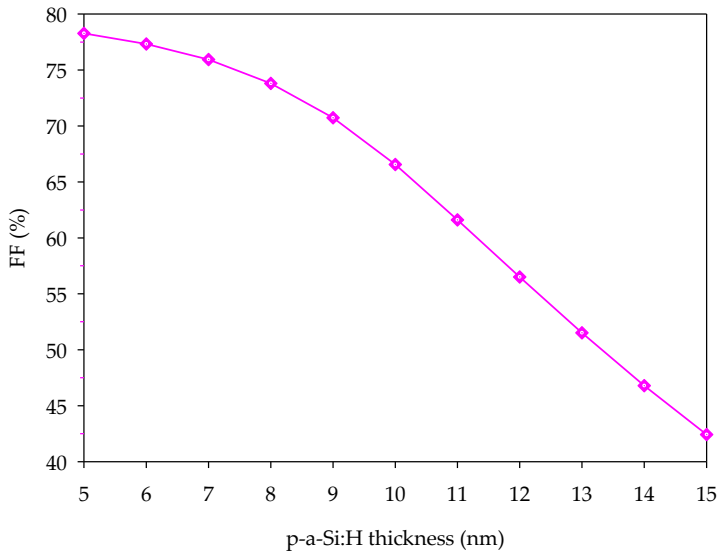

Figure 4.12. FF dependence from the p-a-Si thickness. Data reported in figure are obtained from the SCAPS simulator.

Table 4.8. Si bottom cells SCAPS parameters

Parameters	*n*-a-Si:H	*n*-c-Si	*p*-a-Si:H
Thickness (μm)	0.005	250 / 200	0.005 / 0.007
Bandgap (eV)	1.80	1.12	1.80
Electron affinity (eV)	3.90	4.05	3.90
Dielectric permittivity	11.90	11.90	11.90
CB effective density of states (cm^{-3})	1.0×10^{20}	2.8×10^{19}	1.0×10^{20}
VB effective density of states (cm^{-3})	1.0×10^{20}	1.0×10^{19}	1.0×10^{20}
Thermal velocity hole and electron	1.0×10^{7}	1.0×10^{7}	1.0×10^{7}
Electron mobility (cm^2/Vs)	2.0×10^{1}	1.4×10^{3}	2.0×10^{1}
Hole mobility (cm^2/Vs)	5.0	4.5×10^{2}	5.0
Donor density N_D (cm^{-3})	1.0×10^{17}	$1.5\ 10^{15}$	2.0×10^{18}
Acceptor density N_A (cm^{-3})	1.0×10^{7}	0	0
Defect density N_t (cm^{-3})	-	1.0×10^{11}	-
References	Schropp and Zeman (1998)	D. Kim et al. (2020b), Hussain et al. (2019), Arbitrarily chosen	Schropp and Zeman (1998)

Table 4.9. Si bottom cells bulk defects SCAPS parameters

Parameters	Bulk *n*-a-Si:H (1)	Bulk *n*-a-Si:H (2)	Bulk *n*-a-Si:H (3)	Bulk *n*-c-Si	Bulk *p*-a-Si:H (1)	Bulk *p*-a-Si:H (2)	Bulk *p*-a-Si:H (3)
Defect type	Amphoteric	Donor	Acceptor	Neutral	Amphoteric	Donor	Acceptor
Capture cross section (cm^2)	-	1.0×10^{-16}	1.0×10^{-16}	1.0×10^{-14}	-	1.0×10^{-16}	1.0×10^{-16}
Energetic distribution	Gaussian	Single	Single	Single	Gaussian	Single	Single
Reference energetic level	Below E_C	Above E_V	Above E_V	Above E_V	Below E_C	Above E_V	Above E_V
Energy level (eV)	0.7/0.5	0.6	0.6	0.6	0.7/0.5	0.6	0.6
Characteristic energy (eV)	0.288	-	-	-	0.288	-	-
Defect density N_t (cm^{-3})	8.0×10^{16}	1.0×10^{16}	1.0×10^{16}	1.0×10^{11}	8.0×10^{14}	1.0×10^{16}	1.0×10^{16}
References	Schropp and Zeman (1998)	Schropp and Zeman (1998)	Schropp and Zeman (1998)	Arbitrarily chosen	Schropp and Zeman (1998)	Schropp and Zeman (1998)	Schropp and Zeman (1998)

Table 4.10 Si bottom cells interface defects SCAPS parameters

Parameters	*n*-a-Si:H/*n*-c-Si interface	*n*-c-Si/*p*-a-Si:H interface
Defect type	Neutral	Neutral
Capture cross section (cm^2)	1.0×10^{-18}	1.0×10^{-18}
Energetic distribution	Single	Single
Reference energetic level	Above the highest E_V	Above the highest E_V
Energy level (eV)	0.6	0.6
Defect density N_t (cm^{-2})	1.0×10^{12}	1.0×10^{12}
References	Assumed	Assumed

4.5 Si bottom cells under filtered spectrum

The bottom Si cells were verified under AM1.5G 1 sun spectrum, now they must be simulated under the filtered spectrum generated by the perovskite top cell.

The filtered spectrum of PEDOT:PSS/PTAA/perovskite/C_{60}/PEIE/ITO is calculated starting from the AM1.5G spectrum (Hulstrom, Bird, and Riordan 1985) using the Eq. (2.1) in Section 2.2.3. The light spectrum passes through the top cell so is modified. The filtered spectrum is modified because the photons are mainly absorbed by the perovskite which is the absorber layer, so it is the mainly responsible of spectrum modification. Therefore, to simplify the calculation only the perovskite layer is considered. The effect of the other layers can be neglected. The perovskite absorption coefficient used is taken from Löper et al. (2015). The values of the absorption coefficient are interpolated to have the values at the same wavelength of the AM1.5G spectrum. The thickness *d* is 500 nm. The resulted filtered spectrum has 466.87 W m^{-2} of power density that can be used by the Si bottom cell, so the 51.5% of the light of the AM1.5G spectrum (962.58 W m^{-2}) is filtered by the perovskite top cell.

The SCAPS simulation under the filtered spectrum of 250 µm c-Si cell gives the following performance PCE = 13.99%, V_{OC} = 0.614 V, J_{SC} = 13.172 mA cm^{-2}, and FF = 80.69%; and for 200 µm c-Si cell the performance is PCE = 14.62%, V_{OC} = 0.623 V, J_{SC} = 13.757 mA cm^{-2}, and FF = 79.68%. The Figure 4.13 and 4.14 show the resulted J-V plot and the EQE-

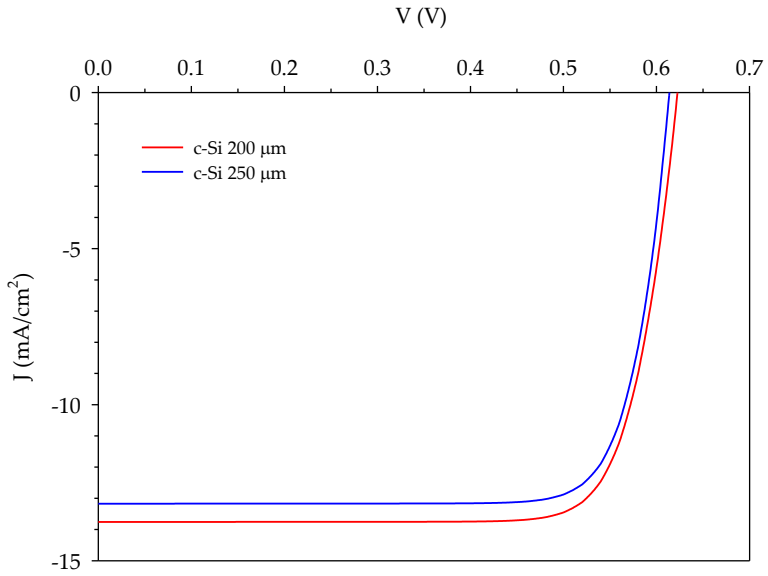

Figure 4.13. Current density J (mA/cm²) - Voltage V (V) plot of Si bottom cells under filtered spectrum. Data reported in figure are obtained from the SCAPS simulator.

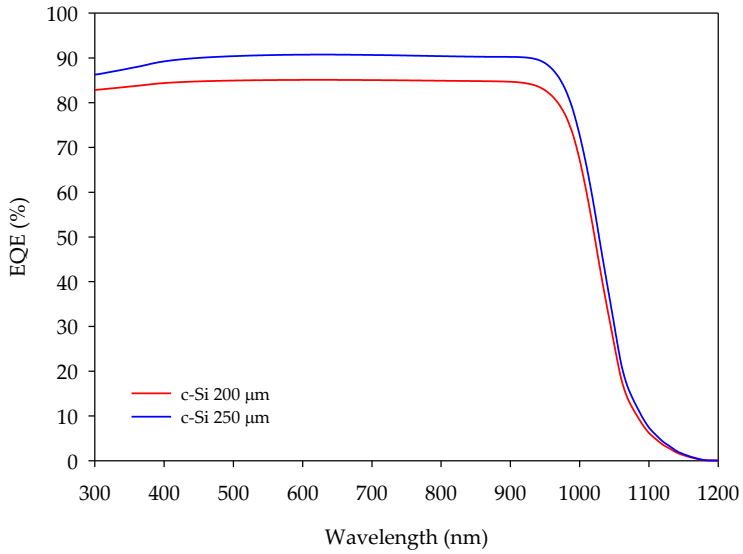

Figure 4.14. External Quantum Efficiency EQE (%) – Wavelength (nm) plot of Si bottom cells under filtered spectrum. Data reported in figure are obtained from the SCAPS simulator.

wavelength plot. The reference performance by D. Kim et al. (2020b) is PCE = 9.39%, V_{OC} = 0.624 V, J_{SC} = 19.32 mA cm^{-2}, and FF = 78%, but the PCE is referred to the AM1.5G 1 sun spectrum. As D. Kim et al. (2020) do not report the power density of the filtered spectrum, the PCE referred to the filtered spectrum cannot be calculated. The PCE of our SCAPS model referred to the AM1.5G spectrum with power density of 96.3 mW cm^{-2} is calculated considering that the PCE the cell is given by $\frac{V_{OC} \cdot J_{SC} \cdot FF}{P}$ where P is the power density equal to 96.3 mW cm^{-2}. For the 250 µm c-Si cell the PCE is 6.78% and for the 200 µm c-Si cell the PCE is 7.09%. For both cells the PCE is around 25% lower than the reference one and the J_{SC} is around 30% lower than the reference one (Table 4.11). The difference in PCE is mainly because of the J_{SC} difference that is around 6 mA cm^{-2}. The J_{SC} is influenced by the intensity of the solar spectrum, so it can be supposed that the filtered spectrum calculated and the one used by Kim et al. are different. The V_{OC} shows a little decrease with respect to the cells illuminated under AM1.5G and the FF a little increase.

Instead of the AM1.5G 1 sun as the reference paper, our filtered spectrum is calculated starting from AM1.5G spectrum to be more realistic with the application. Moreover, it is demonstrated in Section 3.9 that the PCE of the perovskite top cell under AM1.5G spectrum is lowered by 0.05% than the cell under AM1.5G 1 sun spectrum. Anyway, a further sensitive study to see the parameters that increase the J_{SC} is done.

Table 4.11. Performance comparison of Si bottom cells under filtered spectrum illumination. Data reported are taken from D. Kim et al. (2020b) and SCAPS simulator.

	PCE (%)	V_{OC} (V)	J_{SC} (mA/cm^2)	FF (%)
Reference cell: ITO/*n*-a-Si:H/*n*-c-Si/*p*-a-Si:H/ITO/Ag	9.39	0.624	19.32	78.00
(1) 250 μm c-Si cell	6.78	0.614	13.172	80.69
250 μm c-Si cell Data (1) / Ref. Data - 1 (%)	-27.56	-1.60	-31.82	+3.45
(2) 200 μm c-Si cell	7.09	0.623	13.757	79.68
200 μm c-Si cell Data (2) / Ref. Data - 1 (%)	-24.25	-0.16	-28.79	+2.15

4.6 Sensitive analysis for J_{SC}

Only the 200 μm Si cell thickness is studied as it is the cell with highest performance. Looking to the energy band diagram (Fig. 4.7 in Section 4.4) we can think about reducing the electron affinity or the *Eg* of the *p*-layer and increasing the electron affinity of the *n*-layer to have a better collection of carriers due to a favourable band alignment. First the electron affinity *X* of *p*-layer is reduced from 3.9 eV to 3.5 eV. Second the *Eg* of *p*-a-Si:H can be tuned from 1.6 to 1.8 eV as it is reported by (Kabir et al. 2012), so the *Eg* of the amorphous *p*-layer is reduced from 1.8 eV to 1.6 eV. The Figure 4.15 and 4.16 show the results and indicate a little increment of the PCE thanks to the FF improvement. These two parameters *X* and *Eg* are not useful for our purpose of increasing the J_{SC}. Increasing the *X* of the *n*-layer the performance decreases, a result not expected as the electron transfer from the absorber layer to the ETL should be facilitate by the band bending (Fig. 4.17).

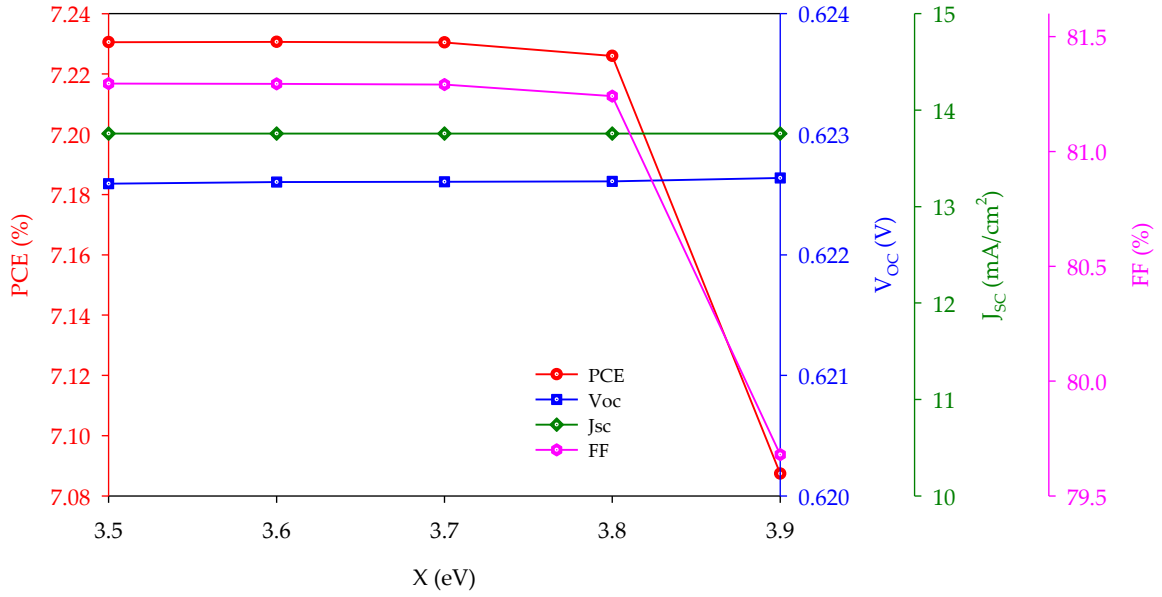

Figure 4.15. Batch simulation of 200 μm Si cell varying the electron affinity X of the p-layer from 3.5 to 3.9 eV. Data reported in figure are obtained from the SCAPS simulator.

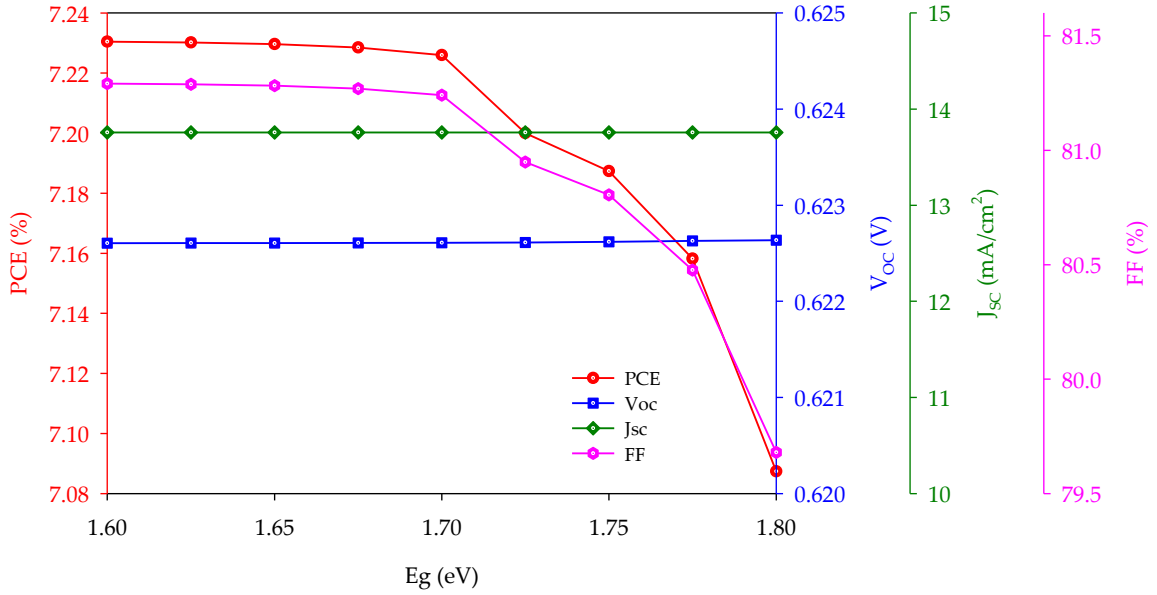

Figure 4.16. Batch simulation of 200 µm Si cell varying the energy gap Eg of the p-layer from 1.6 to 1.8 eV. Data reported in figure are obtained from the SCAPS simulator.

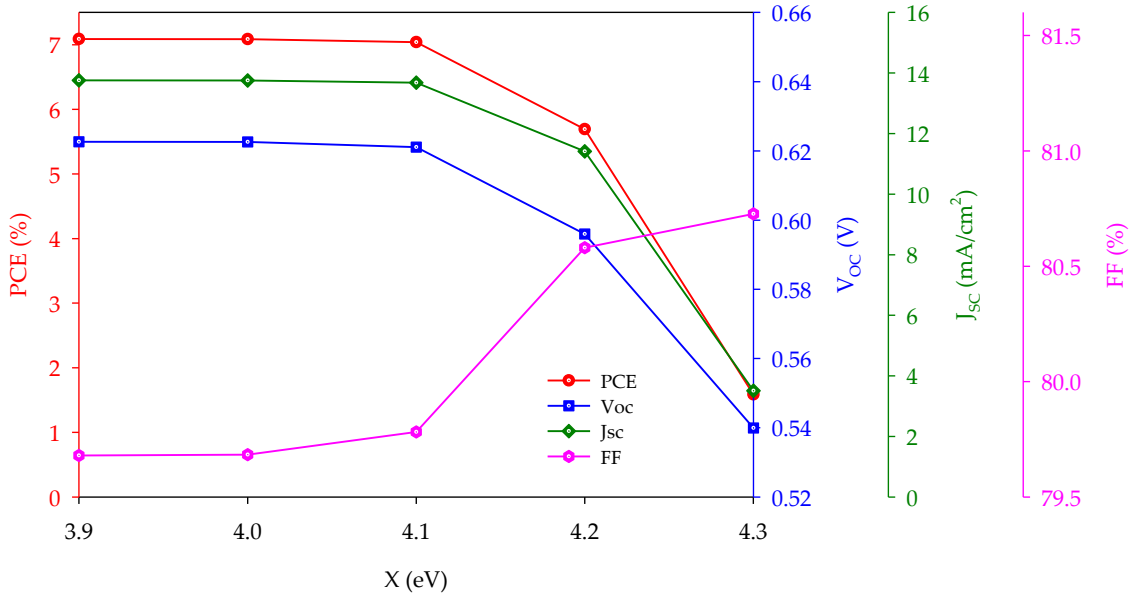

Figure 4.17. Batch simulation of 200 µm Si cell varying the electron affinity X of the n-layer from 3.9 to 4.1 eV. Data reported in figure are obtained from the SCAPS simulator.

As it was seen in Section 4.3.1 that the bulk defect density of c-Si has a big impact it is done a simulation. Reducing the bulk defect density N_t of *n*-c-Si bulk from 1 x 10^{-11} cm^{-3} to 1 x 10^{-10} cm^{-3} the PCE and the J_{SC} increase (Fig. 4.18). In particular for N_t = 1 x 10^{-10} cm^{-3} the performance is PCE = 9.06%, V_{OC} = 0.733 V, J_{SC} = 15.564 mA cm^{-2}, and FF = 76.41%. The J_{SC} increases by 13% about 2 mA cm^{-2} passing from 13.757 to 15.564 mA cm^{-2}. The V_{OC} increases by 17.17%, instead the FF decreases by 4.1%. The PCE increases by 27.79%

reaching a value only 3.51% lower than the reference one. However, the J_{SC} is still about 4 mA cm^{-2} far from the reference J_{SC} value of 19.32 mA cm^{-2} (Table 4.12).

This chapter proves what it was said before, i.e., the mainly reason for the J_{SC} difference is the light intensity.

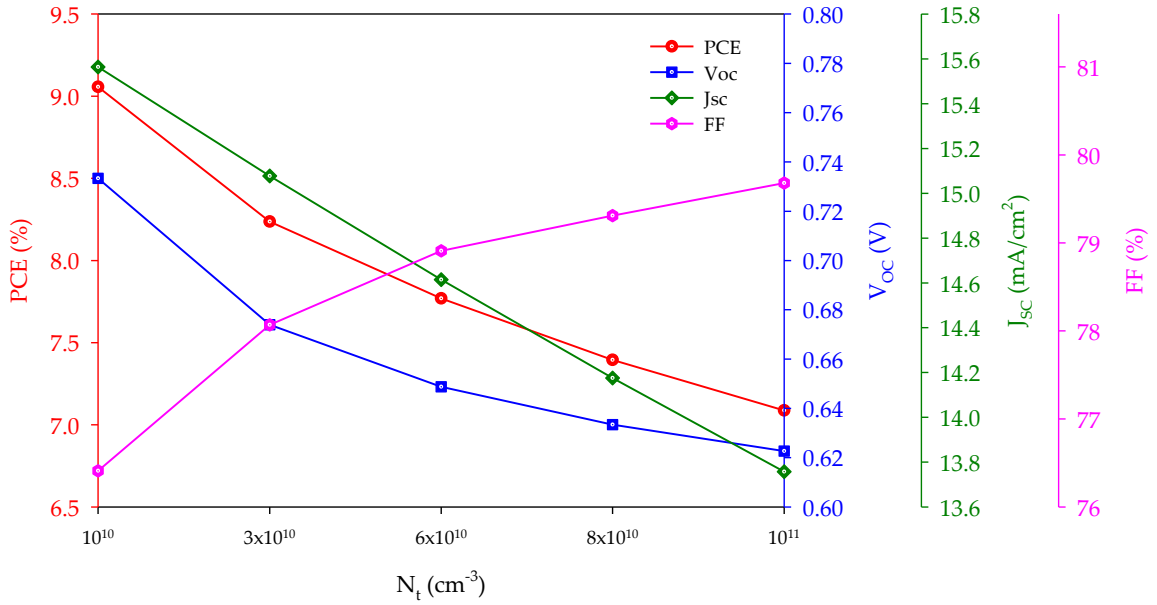

Figure 4.18. Batch simulation of 200 µm Si cell varying the bulk defect density N_t of the absorber layer n-c-Si from 1 x 10^{10} to 1 x 10^{11} cm^{-3}. Data reported in figure are obtained from the SCAPS simulator.

Table 4.12. Performance comparison. Data reported are taken from D. Kim et al. (2020b) and SCAPS simulator.

	PCE (%)	V_{OC} (V)	J_{SC} (mA/cm^2)	FF (%)
Reference Si cell:	9.39	0.624	19.32	78.00
200 µm c-Si cell	7.09	0.623	13.757	79.68
200 µm c-Si cell improved	9.06	0.733	15.564	76.41
Si cell improved Data / Ref. Data - 1 (%)	-3.51	+17.48	-19.44	-2.04
Si cell improved Data / Si cell Data - 1 (%)	+27.79	+17.66	+13.13	-4.10

CHAPTER 5 - TANDEM CELL

The SCAPS cells modelled are virtually stacked together to create a tandem cell with better performance than the individual ones. The tandem perovskite/Si cell will have a configuration *n*-a-Si:H/*n*-c-Si/*p*-a-Si:H/PEDOT:PSS/PTAA/perovskite/C_{60}/PEIE/ITO with perovskite *Eg* = 1.68 eV and c-Si *Eg* = 1.12 eV.

5.1 Light spectra

To take a look of the effect of the absorption property of the perovskite and Si we have to analyse the light spectrum and how it changes (Fig. 5.1). The tandem cell is illuminated under AM1.5G spectrum, the perovskite top cell is the first filter, the filtered light pass through the Si bottom cell and at the end the light should be harnessed as much as possible. The filtered power density P_x (W m^{-2}) resultant from the absorption are calculated through the Eq. (2.1) in Section 2.2.3 with perovskite top cell thickness d_1 = 500

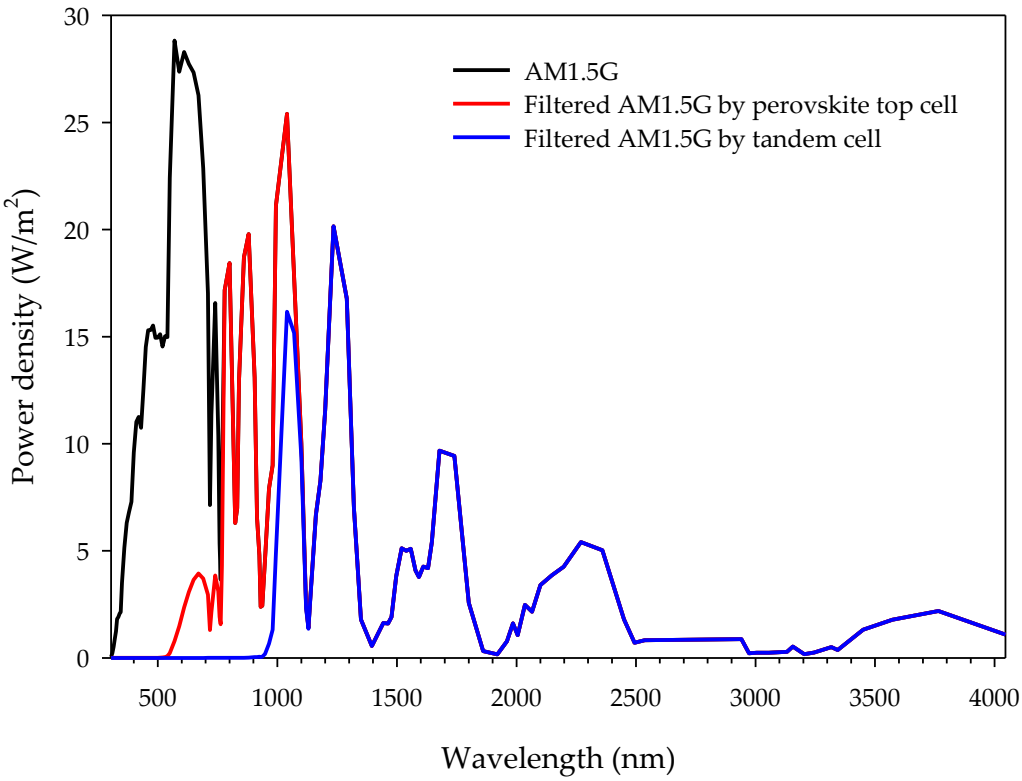

Figure 5.1. Power density P (W/m2) – Wavelength (nm) plot of AM1.5G (SCAPS file), filtered AM1.5G by the top perovskite top cell, filtered AM1.5G by the Perovskite/Si tandem cell. Spectra calculated starting from spectrum and absorption coefficients of Hulstrom, Bird, and Riordan (1985).

nm and Si bottom cell thickness d_2 = 200 μm. For both the cells the only material considered responsible of spectrum modification is the absorber material, i.e., the perovskite for the top cell and the c-Si for the bottom cell.

The AM1.5G has total power density P_0 = 962.58 W m^{-2}, the perovskite top cell uses 495.71 W m^{-2} (the 51.5% of the total AM1.5G power density) and the 48.5% (P_1 = 466.87 W m^{-2}) goes to the Si bottom cell. The power density used by the 200 μm Si bottom cell is 228.46 W m^{-2} (the 48.9% of the filtered spectrum power density P_1) and the 51.1% (P_2 = 238.41 W m^{-2}) is not used. The tandem cell uses 724.17 W m^{-2} (the 75.2% of the AM1.5G power density). The Si cell alone can harness the same percentage of light of the tandem cell, but the Si cell would have lower efficiency with lower J_{SC} and V_{OC} in comparison with the tandem cell. The Si cell as bottom cell provides an increment of 23.7% of light harnessing in comparison with the perovskite cell alone.

5.2 Virtual tandem cell

The reference performance from Kim et al. (2020) study for the tandem monolithic two terminal (2T) perovskite/Si cell is PCE = 26.7%, V_{OC} = 1.756 V, J_{SC} = 19.2 mA cm^{-2}, and FF = 79.2% with negligible hysteresis and a stabilized power output value higher than 26.5%. To verify their in-house measurement, a 2T tandem device of the same design with an active area of 1.001 cm^2 was certified with an efficiency of 26.2%. The tandem cell configuration is a perovskite top cell with a Si bottom cell Ag/ITO/*n*-a-Si:H/*n*-c-Si/*p*-a-Si:H/ITO/PTAA/perovskite/C_{60}/PEIE/ITO/Ag.

Our virtually stacked perovskite/Si tandem cell has configuration *n*-a-Si:H/*n*-c-Si/*p*-a-Si:H/PEDOT:PSS/PTAA/perovskite/C_{60}/PEIE/ITO (Fig. 5.2 and Fig. 5.3). The performance is calculated considering the tandem cell as a series-connected diodes. The reference equations used are reported in Section 2.2.4. The resulted performance is PCE = 23.24%, J_{SC} = 13.757 mA cm^{-2}, V_{OC} = 1.824 V, and FF = 92.63%. The calculations are reported in Section Appendix. In comparison with the reference performance the SCAPS tandem cell PCE is 12.96% lower, the V_{OC} is 3.87% higher, the J_{SC} is 28.34% lower (5.443 mA cm^{-2}), and the FF is 16.96% higher (Table 5.1). The biggest differences are related to the J_{SC} and the FF. We have already analysed the motivation why the J_{SC} is lower in Sections 4.8 and 4.9

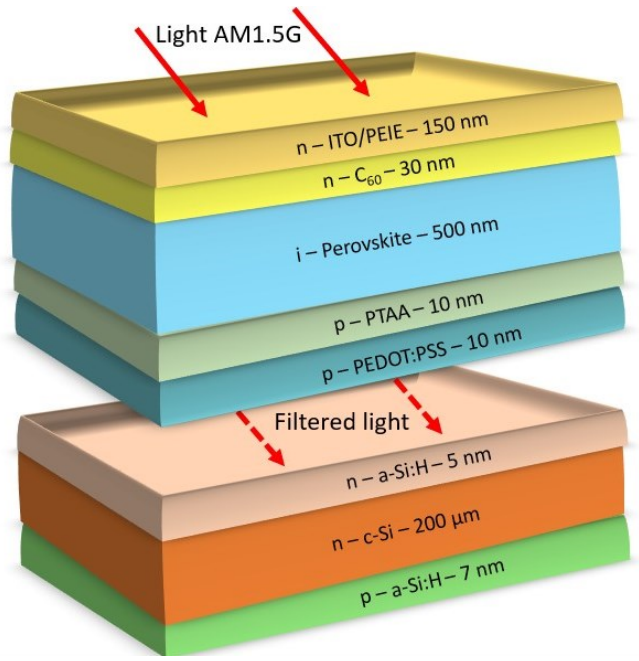

Figure 5.2. Tandem perovskite/Si cell structure simplification.

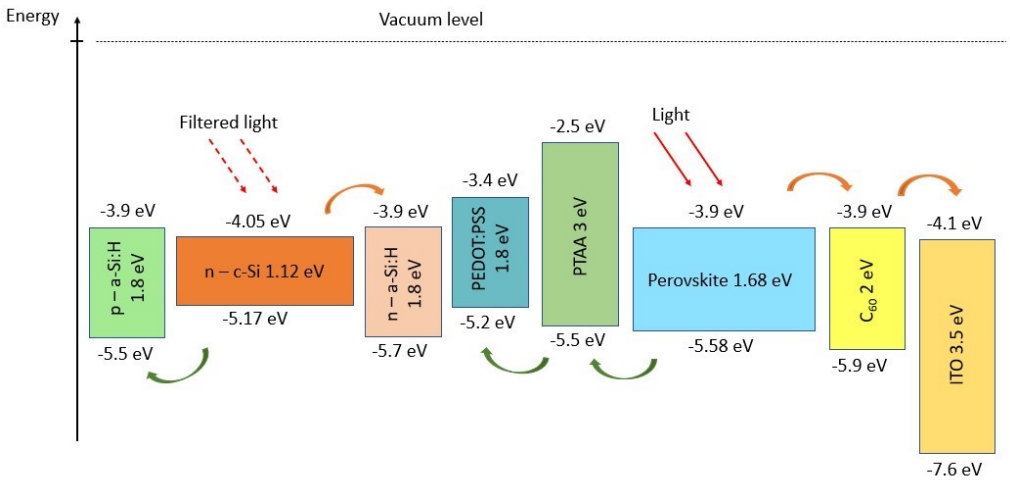

Figure 5.3. Tandem perovskite/Si cell energy band diagram simplification.

anyway to get closer to the reference PCE = 26.7% the J_{SC} should be equal to 17.578 mA cm^{-2}, an increase of 3.821 mA cm^{-2}. From our study the J_{SC} of the Si bottom cell under the filtered spectrum illumination could be increased up to 15.564 mA cm^{-2} reducing the bulk defect density N_t of the c-Si layer to 1 x 10^{10} cm^{-3} (look to Section 4.6). The resulted PCE is equal to 26.29% only 1.54% lower than the reference PCE. Our FF is 16.96% higher than the reference one so it compensates the lower J_{SC}. However, the FF could be lower if it is considered a higher value of the ideality factor n = 2, the FF becomes 87.36% and the PCE = 21.92%; in this case the PCE is 17.90% lower than the reference one.

Table 5.1. Performance comparison. Data reported are obtained from Kim et al (2020) and SCAPS simulator.

	PCE (%)	V_{OC} (V)	J_{SC} (mA/cm²)	FF (%)
Reference tandem cell: Ag/ITO/a-Si:H/c-Si/a-Si:H/ ITO/PTAA/perovskite/C_{60}/PEIE/ITO/Ag	26.7	1.756	19.2	79.2
SCAPS tandem cell: *n*-a-Si:H/*n*-c-Si/*p*-a-Si:H/ PEDOT:PSS/PTAA/perovskite/C_{60}/PEIE/ITO	23.24	1.824	13.757	92.63
SCAPS Data / Ref. Data -1 (%)	-12.96	+3.87	-28.34	+16.96
Improved J_{SC} SCAPS tandem cell	26.29	1.824	15.564	92.63
Improved J_{SC} SCAPS Data / Ref. Data - 1 (%)	-1.54	+3.87	-18.94	+16.96
Reduced FF SCAPS tandem cell	21.92	1.824	13.757	87.36
Reduced FF SCAPS Data / Ref. Data -1 (%)	-17.90	+3.87	-28.35	+10.30

The tandem cell maximum power density P_{max} = 23.24% with working points V_{mpp} = 1.715 V and J_{mpp} = 13.553 mA cm^{-2}. The calculations are reported in Section Appendix. The tandem cell J_{SC}, V_{OC}, J_{mpp} and V_{mpp} are used to approximate the J-V curve of the tandem cell (Fig. 5.4). The tandem cell EQE-Wavelength plot combination of the EQE-Wavelength plots of the perovskite top cell and 200 μm Si bottom cell is reported in Figure 5.5.

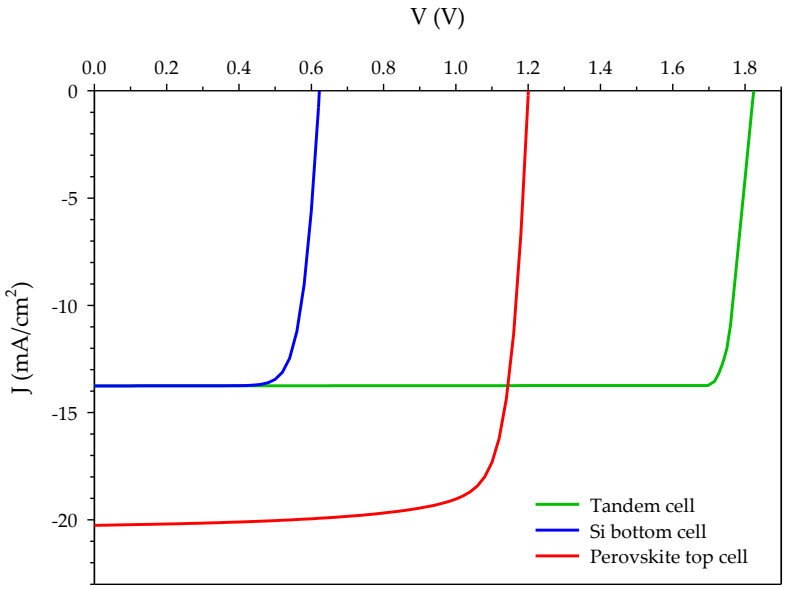

Figure 5.4. Current density J (mA/cm²) – Voltage V (V) plot of Perovskite top cell, Si bottom cell and Tandem perovskite/Si cell. Data reported are obtained from SCAPS simulator. The Tandem cell J-V plot is approximated using four points J_{SC}, V_{OC}, J_{mpp} and V_{mpp}.

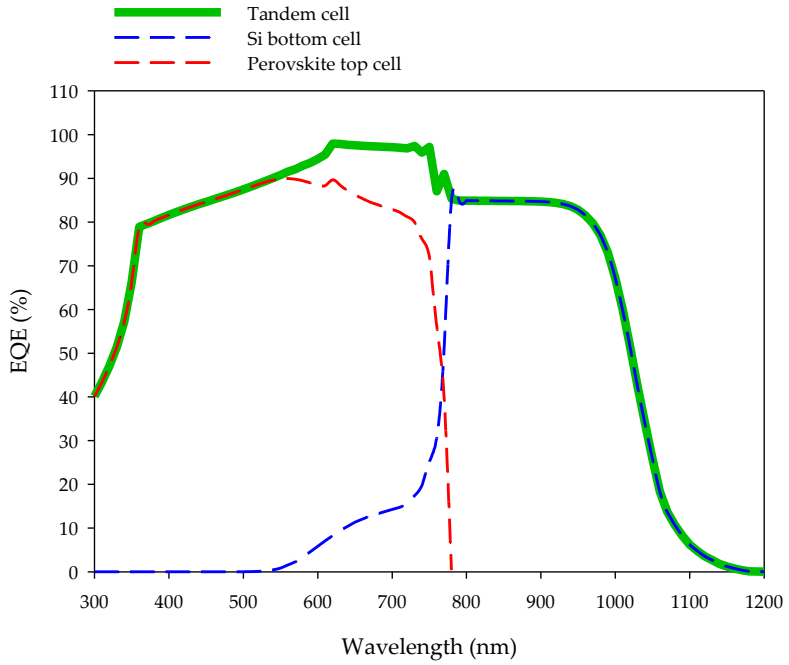

Figure 5.5. External Quantum Efficiency EQE (%) – Wavelength (nm) plot of the Perovskite top cell under AM1.5G spectrum, Si bottom cell under filtered spectrum and of the Tandem cell calculated summing the EQE of the sub-cells. The data reported are obtained from SCAPS simulator.

CHAPTER 6 - CONCLUSION

The goal was to model a wide band gap perovskite solar cell for tandem cells using the Solar Cell Capacitance Simulator (SCAPS). A perovskite top cell with Eg = 1.68 eV is designed and virtually stacked together with a Si bottom cell with Eg = 1.12 eV to create a tandem cell. Every cell is studied in standalone condition and the filtered spectrum derived from the light passing through the perovskite cell is calculated to simulate the Si cell in tandem condition. It is analyzed the spectrum utilization of the tandem cell displaying the EQE-wavelength plot and the power density-wavelength plot. The high perovskite absorption coefficient increases the performance of the standalone Si cell. The perovskite model designed is feasible, reliable and can be adapted to other Si cells.

Optimization studies are done for both cells. From the study of the PTAA, as hole transport layer HTL, it was proved that the Highest Occupied Molecular Orbital level (*HOMO*) of perovskite and PTAA must be aligned to have good performance. The PTAA used must be study furthermore as the electron affinity X selected is not realistic, therefore two other options are provided. The PEDOT:PSS as transparent conductive material (TCO) gives higher performance than the ITO and it can be used as recombination layer in a tandem cell. Some solutions for back and front contacts are given as it is proved that the performance of the perovskite cell remains unchanged. The perovskite thickness and Eg are not a very affecting parameters, so to increase the PCE, a further study about the ETL and the HTL should be carried out. The most affecting parameters for the Si cell are the bulk defect density of the absorber layer and the thickness of the HTL. The bulk defect density of the absorber layer should be reduced as possible in the manufacturing process to have higher PCE. Also, the thickness of the HTL should be reduced in the order of few nm to increase the FF.

The perovskite/Si tandem has configuration *n*-a-Si:H/*n*-c-Si/*p*-a-Si:H/PEDOT:PSS/ PTAA/perovskite/C_{60}/PEIE/ITO with *n*-c-Si thickness of 200 μm and perovskite thickness of 500 nm. The calculated performance considering the tandem cell as a series-connected diodes is PCE = 23.24%, V_{OC} = 1.824 V, J_{SC} = 13.757 mA cm^{-2}, and FF = 92.63% under AM1.5G spectrum. The low tandem J_{SC}, limited by the Si sub-cell, affects the tandem PCE, so the Si sub-cell must be optimized or substituted by another cell with a narrow energy

band gap that gives higher J_{SC}. The perovskite top cell proposed has configuration PEDOT:PSS/PTAA/perovskite/C_{60}/PEIE/ ITO and performance PCE = 20.28%, V_{OC} = 1.201 V, J_{SC} = 20.258 mA cm^{-2}, and FF = 80.26% under AM1.5G spectrum. There were proposed two Si cells, but the best one has configuration *n*-a-Si:H/*n*-c-Si/*p*-a-Si:H and performance PCE = 17.45%, V_{OC} = 0.663 V, J_{SC} = 34.630 mA cm^{-2}, and FF = 75.94% under AM1.5G spectrum; and PCE = 7.09%, V_{OC} = 0.623 V, J_{SC} = 13.757 mA cm^{-2}, and FF = 79.68% under filtered spectrum.

This study is a first step for a perovskite/Si tandem cell production starting from SCAPS simulation results. The researchers can have a clear image on the materials parameters selected and the motivation about their selection. The good final results prove that the path taken to build the cells was appropriate and the sources used are reliable. The models and the tandem cell created can be further studied and then manufactured.

APPENDIX

Equations used are reported in Section 2.2.4

$$J_{SC}\ (\text{tandem}) \approx \min\{J_{SC}(\text{top}), J_{SC}(\text{bottom})\} = \min\{20.258\ , 13.757\} = 13.757\ \text{mA cm}^{-2}$$

$$V_{OC}\ (\text{tandem}) \approx\ V_{OC}\ (\text{top})\ +\ V_{OC}\ (\text{bottom}) =\ 1.201\ +\ 0.623\ =\ 1.824\ \text{V}$$

$$FF(tandem) = \frac{v_{OC}\ (tandem)\ -\ ln(v_{OC}\ (tandem) + 0.72)}{v_{OC}\ (tandem) + 1} = \frac{70.49\ -\ ln(70.49\ +\ 0.72)}{70.49\ +\ 1}$$
$$= 0.9263 =\ 92.63\%$$

$$v_{OC}(tandem) = \frac{q}{nkT}\ V_{OC}\ (tandem) = \frac{1.9\ x\ 10^{-19}}{1\cdot\ 1.38\ x\ 10^{-23}\ \cdot\ 300}\ \cdot\ 1.824\ = 70.49\ \text{V}$$

$$PCE\ (tandem) = \frac{J_{SC}\ (tandem)\ \cdot\ V_{OC}\ (tandem)\ \cdot\ FF\ (tandem)}{P_{inc}}$$
$$= \frac{13.757\ \cdot\ 1.824\ \cdot\ 0.9263}{96.3}\ =\ 23.24\%$$

where the P_{inc} is the power density of the AM1.5G spectrum (W cm^{-2}).

The tandem cell V_{mpp} is calculated using the equation below (Green 1981) through iterations starting from $V_{mpp}\ (\text{tandem})\ =\ 0.9\cdot V_{OC}\ (\text{tandem})$

$$V_{OC}(tandem)\ =\ V_{mpp}(tandem)\ -\ \frac{nkT}{q}\ ln(\frac{q\ V_{mpp}\ (tandem)}{nkT}\ +\ 1)$$
$$V_{mpp}(tandem) =\ 0.9405\cdot V_{OC}\ (tandem) = 0.9405\cdot 1.824 = 1.715\ \text{V}$$

$$J_{mpp}(tandem) = \frac{FF(tandem)\ \cdot\ V_{OC}(tandem)\ \cdot\ J_{SC}(tandem)}{V_{mpp}\ (tandem)} = \frac{0.9263\ \cdot\ 1.824\ \cdot\ 13.757}{1.715}$$
$$= 13.553\ \text{mA cm}^{-2}$$

$$P_{max}(tandem)\ =\ J_{mpp}(tandem)\ \cdot\ V_{mpp}(tandem)\ =\ 13.553\cdot\ 1.715\ =\ 23.24\ \text{W cm}^{-2}$$

BIBLIOGRAPHY

Adachi, Sadao. 1999. "Optical Constants of Crystalline and Amorphous Semiconductors: Numerical Data and Graphical Information." *Published in 1999 in Boston Mass) by Kluwer academic*: 666–666. https://lib.ugent.be/catalog/rug01:000542750 (January 29, 2023).

Aernouts, Tom. 2020. "Expert Talk: Tandem Technology for Solar Cells: Boosting the Efficiency to Accelerate Photovoltaic Integration | EnergyVille." *EnergyVille*. https://www.energyville.be/en/press/expert-talk-tandem-technology-solar-cells-boosting-efficiency-accelerate-photovoltaic (January 28, 2023).

Akln Kara, Duygu et al. 2018. "Enhanced Device Efficiency and Long-Term Stability via Boronic Acid-Based Self-Assembled Monolayer Modification of Indium Tin Oxide in a Planar Perovskite Solar Cell." *ACS Applied Materials and Interfaces* 10(35): 30000–7.

Alipour, Hossein, and Abbas Ghadimi. 2021. "Optimization of Lead-Free Perovskite Solar Cells in Normal-Structure with WO3 and Water-Free PEDOT: PSS Composite for Hole Transport Layer by SCAPS-1D Simulation." *Optical Materials* 120.

Altermatt, Pietro P, on-line lectures, www.pvlighthouse.com.au

Anefnaf, Ikram et al. 2020. "Polyethylenimine-Ethoxylated Interfacial Layer for Efficient Electron Collection in SnO2-Based Inverted Organic Solar Cells." *Crystals* 10(9): 1–12.

Archer, Mary D, and Robert Hill. 2001. "Clean Electricity from Photovoltaics." 1. https://www.worldscientific.com/worldscibooks/10.1142/p139 (January 29, 2023).

Bendib, T. et al. 2020. "Combined Optical-Electrical Modeling of Perovskite Solar Cell with an Optimized Design." *Optical Materials* 109.

Bremner, Levy and Honsberg. 2008. "Analysis of tandem solar cell efficiencies under {AM1.5G} spectrum using a rapid flux calculation method." *Progress in Photovoltaics: Research and Applications* 16(3): 225-223

Burgelman, M., P. Nollet, and S. Degrave. 2000. "Modelling Polycrystalline Semiconductor Solar Cells." *Thin Solid Films* 361–362: 527–32.

Cai, Molang et al. 2017. "Cost-Performance Analysis of Perovskite Solar Modules." *Advanced Science* 4(1).

Chauhan, Shivani, and Rachna Singh. 2021. "A Review on Perovskite/Silicon Tandem Solar Cells." www.preprints.org.

Caprioglio, Pietro et al. 2020. “On the Origin of the Ideality Factor in Perovskite Solar Cells.” *Advanced Energy Materials* 10(27)

Davis, Melissa, and Zhibin Yu. 2020. “A Review of Flexible Halide Perovskite Solar Cells towards Scalable Manufacturing and Environmental Sustainability.” *Journal of Semiconductors* 41(4).

Diekmann, Jonas et al. 2021. *Pathways towards 30% Efficient Single-Junction Perovskite Solar Cells and the Role of Mobile Ions*.

EPFL 2022. “New world records: perovskite-on-silicon-tandem solar cells”, https://actu.epfl.ch/news/new-world-records-perovskite-on-silicon-tandem-sol/ (January 29,2023)

Föll H. 2019. “2.2.4 Simple Junctions and Devices”, https://www.tf.uni-kiel.de/matwis/amat/semi_en/kap_2/backbone/r2_2_4.html (January 5, 2023)

Fu, Xuemei et al. 2018. “Flexible Solar Cells Based on Carbon Nanomaterials.” *Carbon* 139: 1063–73.

Green, Martin A. 1981. “Solar Cell Fill Factors: General Graph and Empirical Expressions.” *Solid-State Electronics* 24(8): 788–89.

Green, Martin A. 1995. “Silicon Solar Cells : Advanced Principles and Practice.” *Published in 1995 in Sydney by University of New South Wales Centre for photovoltaic devices and systems*: 333–36. https://lib.ugent.be/catalog/rug01:000833709 (January 29, 2023).

Green, Martin A. 2022. “Solar Cell Efficiency Tables (Version 60).” *Progress in Photovoltaics: Research and Applications* 30(7): 687–701.

Green, Martin A., Anita Ho-Baillie, and Henry J. Snaith. 2014. “The Emergence of Perovskite Solar Cells.” *Nature Photonics* 8(7): 506–14.

Honsberg, C.B. and Bowden S. G. “Photovoltaics Education Website,” www.pveducation.org, 2019.

Hulstrom, R., R. Bird, and C. Riordan. 1985. “Spectral Solar Irradiance Data Sets for Selected Terrestrial Conditions.” *Solar Cells* 15(4): 365–91.

Hussain, Babar et al. 2019. “Electron Affinity and Bandgap Optimization of Zinc Oxide for Improved Performance of Zno/Si Heterojunction Solar Cell Using PC1D Simulations.” *Electronics (Switzerland)* 8(2).

IEA,2022, Solar PV, IEA, Paris https://www.iea.org/reports/solar-pv, License: CC BY 4.0

Ilic, Ognjen. 2020. “Nanophotonic Materials for Space Applications.” In *MRS Bulletin*, Cambridge University Press, 769–78.

IST 2022. “Solar research institute uses SALD technology for perovskite solar cells.” https://www.ist-surfacetechnology.com/news/solar-research-institute-uses-sald-technology-for-perovskite-solar-cells-3201414.html (December 15, 2022)

Jarwal, Deepak Kumar et al. 2020. “Fabrication and TCAD Simulation of TiO2 Nanorods Electron Transport Layer Based Perovskite Solar Cells.” *Superlattices and Microstructures* 140.

Kabir, Mohammed Ikbal et al. 2012. “Amorphous Silicon Single-Junction Thin-Film Solar Cell Exceeding 10 % Efficiency by Design Optimization.” *International Journal of Photoenergy* 2012.

Kanda, Hiroyuki et al. 2018. “Facile Fabrication Method of Small-Sized Crystal Silicon Solar Cells for Ubiquitous Applications and Tandem Device with Perovskite Solar Cells.” *Materials Today Energy* 7: 190–98.

Khelifi, Samira. 2009. “Characterization and Modelling with Scaps of the Performance of Solar Cells.”

Kim, Daehan et al. 2020a. “Efficient, Stable Silicon Tandem Cells Enabled by Anion-Engineered Wide-Bandgap Perovskites.” *Science* 368(6487): 155–60.

Kim, Daehan et al. 2020b. “Efficient, Stable Silicon Tandem Cells Enabled by Anion-Engineered Wide-Bandgap Perovskites.” *Science* 368(6487): 155–60.

Kim, Sangmo, Van Quy Hoang, and Chung Wung Bark. 2021. “Silicon-Based Technologies for Flexible Photovoltaic (Pv) Devices: From Basic Mechanism to Manufacturing Technologies.” *Nanomaterials* 11(11).

Klein, Andreas et al. 2010. “Transparent Conducting Oxides for Photovoltaics: Manipulation of Fermi Level,Work Function and Energy Band Alignment.” *Materials* 3(11): 4892–4914.

Lamanna, Enrico et al. 2020. “Mechanically Stacked, Two-Terminal Graphene-Based Perovskite/Silicon Tandem Solar Cell with Efficiency over 26%.” *Joule* 4(4): 865–81.

Li, Ling, Gregor Meller, and Hans Kosina. 2007. “Analytical Conductivity Model for Doped Organic Semiconductors.” *Journal of Applied Physics* 101(3).

Li, Ping et al. 2014. “High-Efficiency Inverted Polymer Solar Cells Controlled by the Thickness of Polyethylenimine Ethoxylated (PEIE) Interfacial Layers.” *Physical Chemistry Chemical Physics* 16(43): 23792–99.

Li, Xuejing et al. 2019. “Roles of Polyethylenimine Ethoxylated in Efficiently Tuning the Thermoelectric Performance of Poly(3,4-Ethylenedioxythiophene)-Rich Nanocrystal Films.” *ACS Applied Materials and Interfaces* 11(8): 8138–47.

Li, Zhen et al. 2018. “Scalable Fabrication of Perovskite Solar Cells.” *Nature Reviews Materials* 3.

Llanos, M., R. Yekani, G. P. Demopoulos, and N. Basu. 2020. "Alternatives Assessment of Perovskite Solar Cell Materials and Their Methods of Fabrication." *Renewable and Sustainable Energy Reviews* 133.

Löper, Philipp et al. 2015. "Complex Refractive Index Spectra of CH3NH3PbI3 Perovskite Thin Films Determined by Spectroscopic Ellipsometry and Spectrophotometry." *Journal of Physical Chemistry Letters* 6(1): 66–71. https://pubs.acs.org/doi/abs/10.1021/jz502471h (January 28, 2023).

Luque, A. (Antonio), and Steven. Hegedus. 2011. *Handbook of Photovoltaic Science and Engineering*. Wiley.

MacKay, David JC. 2009. *Sustainable Energy-without the Hot Air*. www.withouthotair.com.

Madan, Jaya, Karanveer Singh, and Rahul Pandey. 2021. "Comprehensive Device Simulation of 23.36% Efficient Two-Terminal Perovskite-PbS CQD Tandem Solar Cell for Low-Cost Applications." *Scientific Reports* 11(1).

Mandadapu, Usha, and B J Babu. 2017. Article in International Journal of Renewable Energy Research *Design and Simulation of High Efficiency Tin Halide Perovskite Solar Cell Spacecraft Solar Arrays View Project Deposition and Characterization of Graded Cu(In1-XGax)Se2 Thin Films by Spray Pyrolysis View Project*. https://www.researchgate.net/publication/322887172.

Mariotti, Silvia et al. 2022. "Monolithic Perovskite/Silicon Tandem Solar Cells Fabricated Using Industrial p-Type Polycrystalline Silicon on Oxide/Passivated Emitter and Rear Cell Silicon Bottom Cell Technology." *Solar RRL* 6(4).

Nave C. 2017. "Work Functions for Photoelectric Effect." http://hyperphysics.phy-astr.gsu.edu/hbase/Tables/photoelec.html (January 20, 2023)

Neder, Verena, Stefan W. Tabernig, and Albert Polman. 2022. "Detailed-Balance Efficiency Limits of Two-Terminal Perovskite/Silicon Tandem Solar Cells with Planar and Lambertian Spectral Splitters." *Journal of Photonics for Energy* 12(01).

NREL. Best Research-Cell Efficiencies. https://www.nrel.gov/pv/cell-efficiency.html (December 16, 2022).

Nuclear Power, 2019. "Conduction and Valence Band in Semiconductors", https://www.nuclear-power.com/nuclear-engineering/radiation-detection/semiconductor-detectors/what-are-semiconductors-properties-of-semiconductors/conduction-and-valence-band-in-semiconductors/ (January 5, 2023)

Paetzold 2022, KIT. "Taskforce Perovskite Photovoltaics", https://www.lti.kit.edu/english/9042.php (January 10, 2023)

Qcells 2022. “European pilot line for innovative photovoltaic technology based on tandem solar cells.” https://www.q-cells.eu/about-q-cells/press-releases/20221123.html (December 15, 2022)

Ravishankar, Sandheep, Zhifa Liu, Uwe Rau, and Thomas Kirchartz. 2022. *Electronic Supplementary Information Multilayer Capacitances: How Selective Contacts Affect Capacitance Measurements of Perovskite Solar Cells*. www.fluxim.com.

Saleh, M, and Le Vide. 1981. 24 2. I. Ishiwara and S. Furukawa. Trans. Instit. Electron. Com-mm. Engrs. Jap ?*?3), and Exact Calculations In*.

Schropp, Ruud E.I., and Miro Zeman. 1998. *Amorphous and Microcrystalline Silicon Solar Cells : Modeling, Materials, and Device Technology*. ed. Kluwer Academic. Boston.

Schwenn, P. E., P. L. Burn, and B. J. Powell. 2011. “Calculation of Solid State Molecular Ionisation Energies and Electron Affinities for Organic Semiconductors.” *Organic Electronics* 12(2): 394–403.

Shockley, Williams. 1950. *Electrons and Holes in Semiconductors with Applications to Transistor Electronics* . New York: Van Nostrand.

Shur, Michael. 2005. “The Electrical Engineering.” In , 153–62.

Sun, Haitao et al. 2016. “Ionization Energies, Electron Affinities, and Polarization Energies of Organic Molecular Crystals: Quantitative Estimations from a Polarizable Continuum Model (PCM)-Tuned Range-Separated Density Functional Approach.” *Journal of Chemical Theory and Computation* 12(6): 2906–16.

Tao, Yuguo. 2016. “Screen-Printed Front Junction N-Type Silicon Solar Cells.” In *Printed Electronics - Current Trends and Applications*, InTech.

Turedi, Bekir et al. 2021. “Perovskite Single-Crystal Solar Cells: Going Forward.” *ACS Energy Letters* 6(2): 631–42.

Wali, Qamar et al. 2018. “Tandem Perovskite Solar Cells.” *Renewable and Sustainable Energy Reviews* 84: 89–110.

Wang, Rui et al. 2019. “A Review of Perovskites Solar Cell Stability.” *Advanced Functional Materials* 29(47).

Wenk, Hans-Rudolf, and A. G. (Andreĭ Glebovich) Bulakh. 2004. *Minerals : Their Constitution and Origin*. Cambridge University Press.

Wojciechowski, Forgács, and Rivera. 2019.” Industrial Opportunities and Challenges for Perovskite Photovoltaic Technology.” *Solar RRL* 3(9)

Würfel, Peter, and Uli Würfel. 2016. *Physics of Solar Cells*.

Yu, Ze et al. 2016. “Indium Tin Oxide as a Semiconductor Material in Efficient P-Type Dye-Sensitized Solar Cells.” *NPG Asia Materials* 8(9): e305.

Zekry, Abdelhalim, Imene Yahyaoui, and Fernando Tadeo. 2019. “Generic Analytical Models for Organic and Perovskite Solar Cells.” In *2019 10th International Renewable Energy Congress, IREC 2019*, Institute of Electrical and Electronics Engineers Inc.